UNIVERSITÀ
DEGLI STUDI
FIRENZE

Scuola di
Scienze Matematiche
Fisiche e Naturali

Corso di Laurea in
Scienze Fisiche e
Astrofisiche

Produzione e Osservazione di Gas Quantistici Degeneri di Atomi Fermionici di ^{6}Li

Production and Observation of Degenerate Quantum Gases of ^{6}Li Fermionic Atoms

Relatore
Dr. Giacomo Roati

Correlatore
Dr.ssa Chiara Fort

Candidato
Klejdja Xhani

Anno Accademico 2013/2014

Contents

To my love Alessio and my family

Dedikuar Alessios dhe familjes time

Introduction

Ultracold atoms are emerged as ideal quantum simulators of many-body physics, becoming model systems where to test quantum Hamiltonians, thanks to the unprecedented possibility of controlling most of the experimental parameters [1] [2]. This feature distinguishes atomic gases from ordinary materials in which the inevitable presence of disorder, interactions and of large number of particles greatly complicates the comparison between microscopic theories and experiments. In ultracold atom experiments it is possible to tailor arbitrary potentials by laser light which mimic the structure of crystals but without the presence of impurity and imperfections. In addition, an extraordinary property of ultracold atoms is the possibility to tune the interaction between atoms by Feshbach resonance [3] [4] which allows to experimentally produce and to study both strongly and weakly correlated gases [5] [6].

One of the latest most exciting results was the observation of superfluidity in fermionic systems. Superfluidity is one of the most spectacular phenomena in nature, intimately connected to superconductivity, being a superfluid essentially a superconductor carrying zero charge. With ultracold atomic fermions, it is nowadays possible to study the physics of the so-called BEC-BCS crossover [7] [8], thanks to the tunability of the interparticle interactions given by Feshbach resonances.

In particular, the transition between a Bose-Einstein condensate (BEC) of molecules and a superfluid composed of Cooper-like pairs of fermions is observed. At the resonance, the size of the pairs becomes much smaller than the one of conventional Cooper pairs, but similar to the ones composing high-T_c superconductor, showing the strong link among these two systems. The quest to develop new and efficient experimental schemes to produce large and highly degenerate fermionic samples is therefore still a crucial challenge.

My thesis fits exactly this context. In fact during my work I have participated to the realization of a new and efficient experimental scheme to produce large degenerate and eventually superfluid gases of fermionic ^{6}Li atoms. Furthermore, I have also designed and then implemented a simple and versatile

optical scheme to image the fermionic atoms (paired or unpaired) across all the interaction regimes offered by the magnetic Feshbach resonance.
In detail, my work was focused in three main topics:

- First implementation and characterization on fermionic ^{6}Li of a Sub-Doppler cooling scheme based on blue-detuned gray molasses. This novel cooling scheme permits to achieve phase space density more than one order of magnitude larger than the one achieved with standard cooling scheme. I have also demonstrated its efficiency even in the high intensity optical dipole trap (peak-intensity of the order of few MW/cm^2)

- Production and characterization of ^{6}Li quantum gases trapped in two different spin states. In particular, I have explored the peculiar regimes offered by the tuning of the interactions via Feshbach resonance. In the repulsive side, I have observed the onset of Bose-Einstein condensates of molecules composed by lithium atoms, while at the center of the resonance (the BEC-BCS crossover), I have studied the presence of a condensate of fermionic pair. In the weakly interacting regime, I have been able to produce ultra-degenerate Fermi gases.

- Design and then implementation of a new optical scheme to image the lithium quantum gases in all the different interaction regimes, which depend on the value of the scattering length between fermions. i.e. on the magnetic field. Both the low and high field imaging is now available in the laboratory in a much more versatile fashion. I have in particular set up an offset-lock loop at 1 GHz able to lock two different laser sources with high stability and tunability. Furthermore, I have built up an home-made laser tapered amplifier to produce the requested laser power to be sent to the atomic sample.

This thesis is divided in four chapters:

1. In chapter one, I describe the properties of ideal and interacting Fermi gases, giving a short theoritical description of their interaction and of the Feshbach resonance. Then I illustrate the special case of the fermionic ^{6}Li, showing in some details the cooling techniques used to produce quantum degenerate Fermi gases.

2. In chapter two, I describe in details our experimental apparatus devoted to the production of lithium quantum gases.

3. In chapter three, I give the main theoretical aspects of the blue-detuned gray molasses. Then, I show the main experimental results characterizing the gray molasses cooling scheme, showing how they are in good agreement with the theoretical expectation. I also show that this new sub-Doppler cooling scheme works efficiently even in the presence of the high intensity dipole trap. At the end of this chapter, I describe the efficient production of molecular BEC and of weakly and strongly degenerate Fermi gases.

4. In chapter four, I describe the optical scheme that I have designed and implemented to produce imaging light resonant with an atomic transition at low and high magnetic field. The imaging light is amplified using a home-made tapered amplifier whose construction, working principle and characterization are shown. The phase-lock loop technique and its experimental realization are described too.

Chapter 1

Ultracold quantum gases

In this chapter, I will introduce the concept of quantum degenerate regime, showing how the density distribution of an ideal trapped Bose and Fermi gas changes passing from the classical to the quantum regime [1], [2]. Then I will consider the case of interacting particles giving a short theoretical description of the two-body scattering problem [1], [2], [3]. In fact, a very interesting property of the ultracold atomic gases is the possibility of tuning their interaction thanks to magnetic Feshbach resonance [4]. This allows to study different and intriguing physical regimes, as we will see in the following of this thesis. At the end of this chapter I will illustrate the special case of the fermionic ^6Li which is implemented in our experiment.

1.1 Quantum degenerate regime

Any particle in nature has an associated de-Broglie wavelength given by $\lambda_{dB} = h/p$, where h is Planck's constant and p is the particle momentum. Within a gas at temperature T, the particles have an average kinetic energy of

$$\frac{p^2}{2m} = \frac{\hbar^2 k^2}{2m} \approx k_B T \tag{1.1}$$

and hence an average momentum $p = \hbar k \approx \sqrt{2mk_BT}$, where m is the mass of the particle, k_B the Boltzman constant and k the wave-vector. Knowing that $k = 2\pi/\lambda_{dB}$ and by substituting it in equation 1.1 I find that the de-Broglie length depends on temperature as $\lambda_{dB} = \sqrt{\frac{2\pi\hbar^2}{mk_BT}}$. At high temperature λ_{dB} assumes values which are small compared with the interparticle separation given by $n^{-1/3}$, where n is the particle density. This means that the particles are well-localized (pointlike) and they can be considered as distinguishable

ones (classical regime). By keeping the density fixed and decreasing the temperature, the spatial wave-functions of individual particles start to overlap as λ_{dB} becomes larger. Consequently, the particles can not be considered anymore as distinguishable ones and they enter in the quantum degenerate regime $\lambda_{dB} \approx n^{-1/3}$.
In the quantum degenerate regime, the probability density, defined as the modulus square of the many-body system wave function $|\Psi|^2$, must be invariant under the exchange of two particles "described" by the coordinates x_i

$$|\Psi(x_1, ..., x_i, ..., x_j ... x_N)|^2 = |\Psi(x_1, ..., x_j, ..., x_i ... x_N)|^2 \tag{1.2}$$

This condition is fulfilled if the many-body wave-function is anti-symmetric or symmetric under the exchange of two particles

$$\begin{cases} \Psi(x_1, ..., x_i, ..., x_j, ..., x_N) = -\Psi(x_1, ..., x_j, ..., x_i, ..., x_N) & \text{Antisymmetric} \\ \Psi(x_1, ..., x_i, ..., x_j, ..., x_N) = \Psi(x_1, ..., x_j, ..., x_i, ..., x_N) & \text{Symmetric} \end{cases} \tag{1.3}$$

In the first case Ψ describes an ensemble of fermions, that have a half-integer spin in units of the reduced Planck's constant; in the second one instead it describes an ensemble of bosons, which have an integer spin in the same units. The anti-symmetry condition for the fermions many-body wave-function, implies that two identical fermions can not occupy the same quantum state because this would lead to $\Psi = 0$. This represent the Pauli exclusion principle. For bosons instead the symmetry condition for Ψ implies that there is not constraint on the number of particles occupying the same quantum state. The distinction between these two different classes is valid not only for elementary particles but also for composite ones, with the sum of spins of their costituents defining the quantum nature (bosons or fermions) of these particles. For instance, a ^{6}Li atom is composed by an odd number of fermions (3 neutrons, 3 protons and 3 electrons) and it is therefore a fermion. A ^{7}Li atom in turn, having 4 neutrons, 3 protons and 3 electrons, is a boson.

1.2 Ideal Bose and Fermi gases in a harmonic trap

In our case and in many other experiments that deal with quantum degenerate gases, the gases are confined in potentials which can be approximated as harmonic ones near their minimum:

$$V(x, y, z) = \frac{1}{2} m(\omega_x{}^2 x^2 + \omega_y{}^2 y^2 + \omega_z{}^2 z^2) \tag{1.4}$$

where ω_i for $i = x, y, z$ are the trapping frequencies in each direction. I consider here the particular case of an ensemble of particles which do not interact (ideal) with each-other. When the thermal energy $1/\beta = k_B T$ is much larger than the harmonic level spacing $\hbar\omega_{x,y,z}$ (Thomas-Fermi approximation) [1],[2] the occupation probability of a phase-space cell $\{\vec{r}, \vec{p}\}$ is given by

$$f(\vec{r}, \vec{p}) = \frac{1}{e^{(\frac{\vec{p}^2}{2m} + V(\vec{r}) - \mu)/k_B T} \pm 1} \tag{1.5}$$

where $\vec{r}$ is the particle position (with coordinates x, y, z), μ is the chemical potential and $V(\vec{r})$ is the external potential which in our case is the harmonic one. The upper sign is for fermions and it is known as Fermi-Dirac distribution, while the lower one is for bosons and it is known as Bose-Einstein distribution. By integrating $f(\vec{r}, \vec{p})$ in momentum space, one found the density distribution

$$n_{th}(\vec{r}) = \frac{1}{(2\pi\hbar)^3} \int d\vec{p} f(\vec{r}, \vec{p}) = \mp \frac{1}{\lambda_{dB}^3} \mathrm{Li}_{3/2}(\mp e^{\beta(\mu - V(\vec{r}))}) \tag{1.6}$$

where $\mathrm{Li}_{3/2}(\mathrm{z})$ is the Polylogarithmic function of order $3/2$, that in general is defined as:

$$\mathrm{Li}_\nu(z) = \frac{1}{\Gamma(\nu)} \int \frac{t^{\nu-1}}{\frac{1}{z} e^t - 1} dt = \sum_{k=1}^{\infty} \frac{z^k}{k^\nu} \tag{1.7}$$

where $\Gamma(\nu)$ is the gamma function of order ν.

In the classical limit (high temperature), the density distribution calculated by equation 1.6 is a Gaussian one known as the Maxwell-Boltzmann distribution:

$$n_{cl} = \frac{N}{\pi^{3/2} \sigma_x \sigma_y \sigma_z} e^{-\sum_i \frac{x_i^2}{\sigma_{x_i}^2}} \qquad \text{where} \qquad \sigma_{x_i}^2 = \frac{2 k_B T}{m \omega_{x_i}^2} \tag{1.8}$$

In the quantum degenerate regime, achieved at $T \approx T_{deg} = \frac{h^2}{2 m k_B} n^{2/3}$ being of the order of μK in typical quantum degenerate gases experiment where $n \approx 10^{13} cm^{-3}$, the density distribution for bosons and fermions have different profiles. A Bose gas undergoes a first-order [9] phase transition to a Bose-Einstein condensation (BEC) which consists in a macroscopic population of the system ground state and in a saturated excited state population at a certain value. Therefore the BEC is described by a many-body wavefunction whose modulus square give the condensed (ground state) part density [2][5] [6] [7] that in the case of the harmonic potential is:

$$n_c(\vec{r}) = \frac{N_0}{\pi^{3/2} d_x d_y d_z} e^{-\sum_i \frac{x_i^2}{d_{x_i}^2}} \tag{1.9}$$

where $d_{x_i} = \sqrt{\hbar/m\omega_{x_i}}$ is the harmonic oscillator length and N_0 is the ground state population. In the harmonic trap, the critical temperature at which the phase transition occurs is:

$$T_{BEC} = \simeq 0.94 \frac{\hbar\bar{\omega}}{k_B} N^{1/3} \tag{1.10}$$

where $\bar{\omega} = (\omega_x \omega_y \omega_z)^{1/3}$ is the geometric mean of the trapping frequencies. For temperature below T_{BEC}, the condensate fraction in the case of the harmonic trap is given by:

$$\frac{N_0}{N} = 1 - \left(\frac{T}{T_c}\right)^3 \tag{1.11}$$

Fermions instead "repel" each other and each quantum state is occupied by at maximum one particle (Pauli exclusion principle). At zero temperature, each of the states with energy less than the Fermi energy E_F is occupied but no phase transition occurs. In this limit the Fermi-Dirac distribution becomes

$$f(\vec{r},\vec{p}) = \frac{1}{e^{(\frac{\vec{p}^2}{2m} + V(\vec{r}) - \mu)/k_B T} + 1} \xrightarrow{T \to 0} \begin{cases} 1 & \frac{\vec{p}^2}{2m} + V(\vec{r}) \leq \mu \\ 0 & \frac{\vec{p}^2}{2m} + V(\vec{r}) > \mu \end{cases} \tag{1.12}$$

where the chemical potential coincides with the Fermi energy at zero temperature. After substituting in equation 1.6, one finds that the density profile changes smoothly from its Gaussian shape at high temperature to its zero temperature profile that, for our case of harmonic trap, is given by:

$$n_F(\vec{r}) = \frac{8}{\pi^2} \frac{N}{R_{F_x} R_{F_y} R_{F_z}} \left[max\left(1 - \sum_i \frac{x_i^2}{R_{F_i}^2}, 0\right)\right]^{3/2} \tag{1.13}$$

with $R_{F_{x,y,z}} = \sqrt{\frac{2E_F}{m\omega_{x,y,z}^2}}$ the Fermi radii. This density profile is flat top with respect to the Gaussian one because the occupation of the excited states saturates at unity. From the total fermion number $N = \int n_F(\vec{r}) d\vec{r}$, the Fermi energy value is found to be:

$$E_F = (6N)^{1/3} \hbar\bar{\omega} \tag{1.14}$$

1.3 Interaction in ultracold atoms

In the field of quantum degenerate (ultracold) atoms, interactions play an important role not only in preparing quantum degenerate ensembles but also

in the physics phenomena that are studied. At degenerate regime temperature, the system stable phase is the solid one, but supposing that the range of the interaction potential R_0 is much smaller than the interparticle distance (diluteness condition) the system phase becomes the gaseous one. For instance, in the case of ^{6}Li, the interparticle distance $n^{-1/3} \sim 5000 - 10000a_0$, where a_0 is the Bohr radius, is in fact much larger than the range of interaction potential (supposed the van der Waals potential [2]) $R_0 \sim 50a_0$. In such ultradilute and ultracold ensembles, the two-body interactions dominate and the collision process can be described in terms of a single quantity: the scattering length. I consider two spinless atoms or two atoms in the same spin state with mass m_1, m_2 interacting through the two-body interaction potential $\mathrm{V}(\vec{R_1} - \vec{R_2})$. In the two-particle center of mass, this problem is reduced in studying the motion of a "fictitious" particle of mass $\mu = \frac{m_1 m_2}{m_1+m_2}$ in the interaction potential $V(\vec{R})$, where $\vec{R} = \vec{R_1} - \vec{R_2}$ is the relative position vector. The wave function of the "fictitious" particle $\psi_{\vec{k}}(\vec{R})$ corresponding to eigenvalue E satisfies the Schrödinger equation

$$-\frac{\hbar^2}{2\mu}\nabla^2\psi_{\vec{k}}(\vec{R}) + V(\vec{R})\psi_{\vec{k}}(\vec{R}) = E\psi_{\vec{k}}(\vec{R}) \tag{1.15}$$

Considering a short-range R_0 potential, i.e. that goes to zero when $R > R_0$, one finds that asymptotically ($R >> R_0$), the wave-function is given by the sum of the incoming wave plane, with wave vector $\vec{k_i}$ and propagation direction $\hat{k_i} = \vec{k_i}/k_i$, and the outgoing scattered spherical wave-function, with wave vector $\vec{k_f} = k\vec{n}$ and propagation direction $\vec{n} = \vec{R}/R$

$$\psi_{\vec{k}}(R) \propto e^{i\vec{k}_i\cdot\vec{R}} + f(k, \hat{k_i}, \vec{n})\frac{e^{ikR}}{R} \tag{1.16}$$

where $f(k, \hat{k_i}, \vec{n})$ is the scattering amplitude in the direction defined by $\vec{n}$ and its general expression is

$$f(k, \hat{k}_i, \vec{n}) = -\frac{\mu}{2\pi\hbar^2}\int d^3\vec{r}' e^{-i\vec{k}_f\cdot\vec{r}'}V(\vec{r}')\psi_{\vec{k}}(\vec{r}') \tag{1.17}$$

For a spherically symmetric potential ($V(\vec{R}) = V(R)$), considered hereafter, the scattering amplitude depends only on k and the angle θ between the incident and scattered wave vector. In the case of distinguishable particles, one can find that the differential and total cross section are given by

$$\frac{d\sigma}{d\Omega} = |f(\theta, k)|^2 \qquad \text{and} \qquad \sigma(k) = \int |f(\theta, k)|^2 d\Omega \tag{1.18}$$

where $0 < \theta < \pi$.

Including quantum statistics

For indistinguishable particles in the same spin state, the two posssible scattering processes shown in figure 1.1, corresponding to the scattering amplitude $f(\theta, k)$ and $f(\pi - \theta, k)$, are indistinguishable due to the overlap between the two-atoms wave function in the collision region. Consequently, the

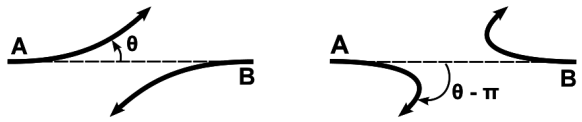

Figure 1.1: Two possible scattering process for two identical particles

asymptotic scattering wave-function must be symmetrized or anti-symmetrized with respect to the two-particle coordinates exchange for bosons or fermions respectively becoming

$$\psi_{\vec{k}}(R) \propto \frac{1}{\sqrt{2}}(e^{i\vec{k}\cdot\vec{R}} \pm e^{i\vec{k}\cdot\vec{R}}) + \frac{1}{\sqrt{2}}(f(\theta, k) \pm f(\pi - \theta, k))\frac{e^{ikR}}{R} \tag{1.19}$$

with the plus sign for bosons and the minus one for fermions. Thus the differential cross section is given now by

$$\frac{d\sigma}{d\Omega} = |f(\theta, k) \pm f(\pi - \theta, k)|^2 \tag{1.20}$$

with $0 < \theta < \pi/2$.

Partial wave expansion and low energy limit

As the scattering potential is considered spherically symmetric, the system own to a cylindrical symmetry which permits to expand the wave-function as

$$\psi_{\vec{k}}(\vec{R}) = \sum\nolimits_l \frac{u_{k,l}(R)}{R} P_l(\cos\theta) \tag{1.21}$$

where l is the angular momentum, $u_{k,l}$ is the radial wave-function depending only on R, and $P_l(\cos\theta)$ is the Legendre polynom depending only on θ. By substituting this partial wave expansion into equation 1.15, one obtains that for each of the angular momentum values the radial wavefunction satisfies

$$\left[-\frac{\hbar^2}{2\mu}\frac{d^2}{dR^2} - \frac{\hbar^2 k^2}{2\mu} + V_{eff}(R)\right] u_{k,l}(R) = 0 \tag{1.22}$$

where $V_{eff}(R) = \frac{\hbar^2 l(l+1)}{2\mu R^2} + V(R)$ is the "effective" potential with the second term interpreted as the centrifugal potential. The expression of the total cross-section can now be found in terms of l

$$\sigma(k) = \sum_{l=0}^{\infty} \sigma_l(k) \qquad \text{with} \qquad \sigma_l(k) = \frac{4\pi}{k^2}(2l+1)\sin^2\delta_l(k) \quad (1.23)$$

which contains only even(odd) values of l for bosons(fermions) with δ_l being the phase shift acquired during the scattering process by the incoming plane wave and it depends on energy, therefore on k. In our case of fermionic lithium, the p-wave scattering is present for temperature larger than $T_p = 6$ mK, which is much larger than the window for quantum degeneracy [2]. Therefore a second species or second hyperfine state is needed for thermalization and evaporative cooling. In the general case of ultracold atoms, to which corresponds low momenta $k << 1/R_0$, the scattering process can occur for $l = 0$ (s-wave) as for any $l \neq 0$ the centrifugal barrier heigth is larger than their energy E. The s-wave scattering amplitude is independent on θ and is given by

$$f_{k,l=0} = \frac{1}{k} e^{i\delta_0} \sin\delta_0 \quad (1.24)$$

where δ_0 is the phase shift acquired by $l = 0$ partial waves in terms of which one defines the s-wave scattering length as

$$a = -\lim_{k\to 0} \frac{\tan\delta_0}{k} \qquad \text{or equivalently} \qquad \delta_0(k) \xrightarrow{k\to 0} -ka \quad (1.25)$$

The s-wave scattering total cross section for fermions, bosons and distinguishable particles is now expressed as

$$\sigma = \begin{cases} \frac{4\pi a^2}{1+k^2a^2} & \text{for distinguishable particle} \\ \frac{8\pi a^2}{1+k^2a^2} & \text{for identical bosons} \\ 0 & \text{for identical fermions} \end{cases} \quad (1.26)$$

In the limit $ka << 1$, the total cross-section becomes energy independent (independent on k) and depends only on a; it is equal to $4\pi a^2$ and $8\pi a^2$ for distinguishable and identical bosons respectively. In the limit $ka >> 1$, called the unitarity limit, $\sigma = 4\pi/k^2$ for distinguishable particle and a factor of 2 larger for the bosons.

1.4 Tuning interaction: Feshbach resonance

An extraordinary property of ultracold atomic gases is the possibility to tune their interaction, i.e. the scattering length, by just varying an external

magnetic field, thanks to the Feshbach resonance they present. Consequently one can study different physical regimes; BEC and BCS superfluidity (see section "BEC-limit" and "BCS-limit"). But the most unique feature is the possibility to study the crossover between these two regimes that otherwise in condensed matter physics is not possible. The physical interpretation of this resonance and the different physics regimes main features are given in the following section, where the atoms internal states are taken into account to describe the resonance scattering.

1.4.1 Basic theory concepts

Each atom is characterized by its total angular momentum $\vec{F}$ which is the vectorial sum of the electron total angular momentum $\vec{J}$ with the nuclear one $\vec{I}$. At low uniform external magnetic field B, the total angular momentum quantum number F and its projection m_F along the B-axis are good quantum numbers. Therefore, the initial collision channel, called also the "open channel", is defined by specifing the quantum numbers $\{F_1, m_{F_1}; F_2, m_{F_2}; l = 0\}$ of both atoms (1 and 2). There are also other collision channels which are characterized by different quantum numbers. The interaction potential contains the van der Waals term, which describes the interaction between the electric dipole-dipole of atoms, and another one describing the interaction between the atoms magnetic moment [2], which depends on the relative $\vec{F_i}$ (with $i = 1, 2$) orientations. The last term gives rise to the coupling between different channels, but we consider here only the coupling between the open and a closed channel (two-channel model) as shown in figure 1.2.

A channel is called closed when its dissociation threshold energy is above E, so that the two colliding atoms can not belong to the continuum of this channel. We suppose also that the closed channel support a bound state whose energy E_{res} is not too much different from E. The two possible channels shown in figure 1.2 correspond to different total F configurations ($\vec{F} = \vec{F_1} + \vec{F_2}$) and also to different magnetic moments. This means that by sweeping a static magnetic field the open and closed channel potential move with respect to each other varying so the energy difference

$$E_{res} - E = \Delta\mu(B - B_0) \tag{1.27}$$

where $\Delta\mu$ is the difference between the open and close channel magnetic moments (see figure 1.2). When the energy of the closed channel bound state is resonant with the energy of the colliding particles ($E_{res} - E = 0$), the scattering length goes to infinity. This is called the Feshbach resonance and from equation 1.27 it happens at the magnetic field value B_0. Actually, there

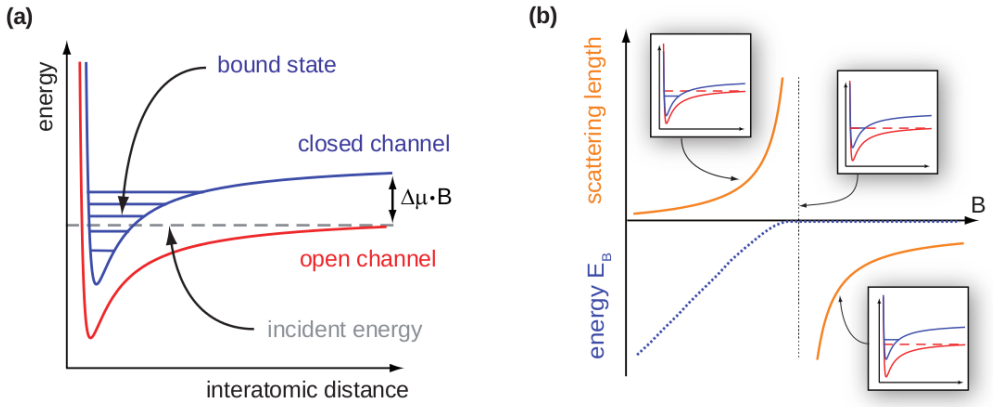

Figure 1.2: Left figure: The open (red) and closed (blue) channel potential corresponding to different $\vec{F}_i$ orientation, where it is indicated the bound state of the closed channel and the free atoms energy too [2]. Right figure: The energy of the dimer state (blue profile) and the s-wave scattering length (orange profile) as a function of the magnetic field values [19]. In the inset is shown the relative position between the open and closed channel to which corresponds different values of the scattering length.

is an anti-crossing between the closed bound state and the continuum states energy due to the strong coupling between the two channels. In fact, the resonance position is shifted at a different magnetic field value B_c. Hereafter, we take the continuum state energy as zero, which is a good approximation for the case that we are considering of ultracold atoms. The expression of the scattering length [4] around the Feshbach resonance (fig. 1.2) is given by:

$$a(B) = a_{BG}(1 - \frac{\Delta}{B - B_c}) \tag{1.28}$$

where the width of the resonance Δ is such that at $B = B_c + \Delta$, the zero crossing of the scattering length ($a = 0$) is achieved, while a_{BG} is the scattering length corresponding to the situation where the atoms enter and exit in the "open" channel (no resonance scattering). Near the Feshbach resonance, dimer states are formed having a binding energy

$$E_b = -\frac{\hbar^2}{2\mu a^2} \tag{1.29}$$

which, from equation 1.28, depends quadratically on the detuning $B - B_c$ (fig. 1.2). The properties of these Feshbach molecules ("dimer states") are considered in details in the section "BEC-BCS crossover."

1.4.2 Weakly bound dimers stability

The expression given before for the dimer states binding energy $E_b = -\frac{\hbar^2}{2\mu a^2}$ is valid in the case of a dimer size a greater than the potential range, which is true for $a \to \infty$ (as it happens at the Feshbach resonance). In the case of lower positive scattering length, it satisfies a similar expression but a mean scattering length ($\overline{a}$) is subtracted from a

$$E_b = -\frac{\hbar^2}{2\mu(a-\overline{a})^2} \tag{1.30}$$

For instance, in the case of ^{6}Li $\overline{a} \simeq 30a_0$. The stability of this gas composed of dimers depends on the frequency at which atom-dimer or dimer-dimer collisions happen, causing the decay of the dimer states into deeper states. In a two-state fermionic mixture, these three or four body collisions include at least two identical fermions. In this case of weakly bound dimers, the atoms quantum fermionic nature is considered and, from the Pauli exclusion principle, these processes are suppressed. The atom-dimer and dimer-dimer scattering length [1] is given by

$$a_{dd} = 0.6a \qquad \text{and} \qquad a_{ad} = 1.2a \tag{1.31}$$

The relaxation rate constant for the case of a weakly bound dimer state

$$\alpha_{relax} \propto \begin{cases} a^{-3.33} & \text{atom-dimer} \\ a^{-2.55} & \text{dimer-dimer} \end{cases} \tag{1.32}$$

is small (approximately zero) for large atom-atom scattering length, i.e. strong interactions, and the gas is thus more stable. Also the ratio of the relaxation to the elastic rate is an important quantity that characterizes the dimer gas stability and assumes small values (approximately 10^{-4} for ^{6}Li). This permits long-life Feshbach molecular gases.

1.4.3 Two-particle energy spectrum

In this section, I follow the simple model described in more details in [3] to find the spectrum energy of a homogeneous ultracold Fermi gas composed of $N/2$ particles having spin "up",i.e. the spin projection on the quantum axis is $m_s = +1/2$ in units of $\hbar$, and the other $N/2$ particles having spin "down" ($m_s = -1/2$). Firstly, I consider the two-body s-wave scattering between a fermion with spin "up" and its nearest fermion with spin "down" and then include the effect of the other spin "up" and "down" particle. The

interaction potential is taken to be the Fermi delta pseudo-potential having a zero range

$$V_{pseudo} = g\delta_{reg}(\vec{r}) \tag{1.33}$$

with $g = 4\pi\hbar^2 a/m$ the coupling constant choosen to give the correct scattering length and m the particle mass. This is a good approximation of the true

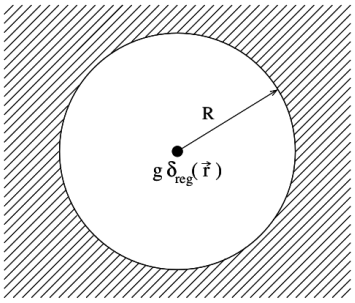

Figure 1.3: The schematic model of the interaction between the $N/2$ fermions with spin $+1/2$ with other $N/2$ fermions with spin $-1/2$ [3].

interaction potential in the regime $n{r_e}^3 << 1$ (r_e is the effective range of the true potential [10]), which is also the condition to have gaseous system. To eliminate singularities in the Schrödinger equation [1], the pseudo-potential is replaced with the contact condition

$$\lim_{r\to 0}\frac{\partial_r(r\Psi)}{r\Psi} = -\frac{1}{a} \tag{1.34}$$

where r is the distance from the origin ($r = 0$) and Ψ is the wavefunction of the "fictitious" particle having mass $\mu = m/2$ (see previous section). To take into account the interactions effect of the rest $N/2 - 1$ spin $-1/2$ particles and the Fermi statistical effect of the remaining $N/2 - 1$ spin $+1/2$ particles, the boundary conditions are choosen such that Ψ vanishes at the surface of a sphere having radius $R \propto 1/k_F$, with k_F the Fermi wave-vector (fig. 1.3). By considering the contact and boundary conditions, the Schrödinger equation is resolved for both positive and negative energy values. The results for the total energy per particle E/N of the first two lowest branches as a function of $-\frac{1}{k_F a}$, which is the ratio of the interparticle spacing to the scattering length, are shown in figure 1.4.

We can note two regimes in the ground branch:

- the first regime $k_F a \to 0^-$ (i.e. $-\frac{1}{k_F a} \to +\infty$) represents a weakly attractive Fermi gas which, at zero temperature, corresponds to the superfluid BCS phase.

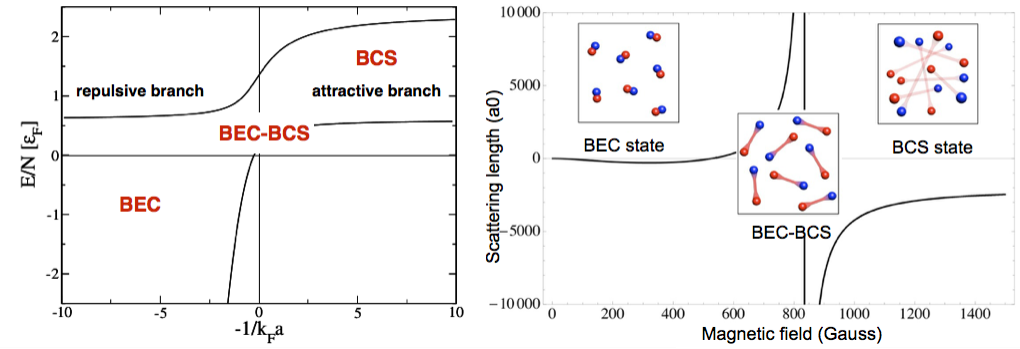

Figure 1.4: Left figure: The total energy per particle in units of the Fermi energy ϵ_F as a function of $-\frac{1}{k_F a}$ [3]. Right figure: The different physical regimes found in the ground branch are indicated at the corresponding scattering length.

- the second regime $k_F a \to 0^+$ (i.e. $-\frac{1}{k_F a} \to -\infty$) represents a dilute gas of dimers where each of them is a molecular bound state of two opposite spin fermions and have an energy $E_b = -\hbar^2/ma^2$. At zero temperature they form a Bose-Einstein condensation of weakly-interacting molecules of mass $M = 2m$.

- The cross-over between these two regimes corresponds to the Feshbach resonance, $a \to \infty$ i.e. $-1/k_F a = 0$, and it is called the unitarity regime. It can be noted that in this regime, the mean energy per particle is less than the ideal Fermi gas energy, implying that there is an effective attraction between the atoms.

For the first excited branch instead one notes that the limit $k_F a \to 0^+$ corresponds to a weakly repulsive Fermi gas as in this limit the mean energy per particle is larger than the ideal Fermi gas energy ($E = \frac{3}{5} N E_F$). It is a metastable state of the gas because, during three body collisions, if a dimer is formed, the releasing energy is carried away by the third atom, causing the state to decay from the excited to the ground branch.

1.4.4 BEC-limit $k_F a \to 0^+$

For $k_F a \to 0^+$, corresponding to positive scattering length, the interaction potential supports a bound state and the atoms in the two-spin states can form molecules. At temperature below the critical one, these molecules can condensate into a BEC. For this reason this limit is called the BEC-limit. The condensed part, i.e. the molecular BEC, is described by a many-body

wavefunction $\psi(\vec{r},t)$ that obeys the Gross-Pitaevski equation (GP) [5], [6], [7] in the limit of weakly interacting gases where $n_M a_M^3 << 1$

$$\left(-\frac{\hbar^2\nabla^2}{2M} + V_M(\vec{r}) + g|\psi(\vec{r},t)|^2\right)\psi(\vec{r},t) = i\hbar\frac{\partial\psi(\vec{r},t)}{\partial t} \tag{1.35}$$

where $V_M(\vec{r})$ is the molecular trapping potential, $g = 4\pi\hbar^2 a_M/M$ is the coupling constant for molecules and $a_M = 0.6a_{dd}$ is the scattering length between two molecules, i.e. four fermions. In equilibrum, the ground state wave-function can be written as $\psi(\vec{r},t) = e^{-i\mu_M t/\hbar}\psi(\vec{r})$ where μ_M is the the ground state energy being equal to the molecular chemical potential and twice the atomic chemical potential, while $\psi(\vec{r})$ is a solution of the stationary Gross-Pitaevski equation

$$\left(-\frac{\hbar^2\nabla^2}{2M} + V_M(\vec{r}) + g|\psi(\vec{r})|^2\right)\psi(\vec{r}) = \mu_M\psi(\vec{r}) \tag{1.36}$$

The condensed part density distribution, defined as $n_c(\vec{r}) \equiv |\psi(\vec{r})|^2$, in the Thomas-Fermi approximation which considers the kinetic term negligible compared to the interaction one ($gn_c > \hbar\omega_{x,y,z}$), is found to be

$$n_C(\vec{r}) = max\left(\frac{\mu_M - V_M(\vec{r})}{g}, 0\right) \tag{1.37}$$

where the zero value is assumed for $\mu_M < V(\vec{r})$. Typical value for gn_c away from the Feshbach resonance and $\hbar\omega$ are k_Bx$150nK$ and k_Bx$5nK$ respectively so the Thomas-Fermi approximation is valid. In our case of the harmonic trap the condensed part density is

$$n_C(\vec{r}) = \frac{15}{8\pi}\frac{N_M}{R_x R_y R_z} max\left(1 - \sum_i \frac{x_i^2}{R_i^2}, 0\right) \tag{1.38}$$

i.e. an inverted parabola with $R_i = \sqrt{\frac{2\mu}{m\omega_i^2}}$ the Thomas-Fermi radii. At the Thomas-Fermi radius the wavefunction of the BEC goes to zero and it is thus a measure of the size of the condensate. One can also determine the chemical potential from the normalization condition $N_M = N/2 = \int n_c(\vec{r})d\vec{r}$ and the result is

$$\mu_M = \frac{\hbar\bar{\omega}}{2}\left(\frac{15N_M a_M}{\bar{a}_{h.o.}}\right)^{2/5} \tag{1.39}$$

being on order of kHz, with $\bar{a}_{h.o.} = \sqrt{\hbar/m\bar{\omega}}$ being the geometric mean of the harmonic oscillator lengths.

1.4.5 BCS-limit $k_F a \to 0^-$

In the BCS-limit of weakly attractive interactions between fermions with opposite spin components, weakly bound pairs called Cooper pairs [8] are formed at the Fermi surface, which is the surface of a sphere of radius the Fermi momentum k_F in the momentum-space. Their binding energy [8] depends exponentially on the interactions and assumes small values for $k_F a \to 0^-$:

$$E_B = -\frac{8}{e^2} E_F e^{-\pi/k_F|a|} \tag{1.40}$$

If the Cooper pairs interact with the particle consituent of the Fermi sea, the Fermi sea is unstable towards pairing (Cooper instability) and a many-body description is necessary for the paired-states system. It is given by Bardeen, Copper and Schrieffer (BCS) [1] [8] theory which was developed to explain superconductivity in metals. According to this theory the Cooper pairing causes an energy gap

$$\Delta = \frac{8}{e^2} E_F e^{-\frac{\pi}{2k_F|a|}} \tag{1.41}$$

to open at the Fermi surface and the system becomes superfluid. The superfluid gap is larger than the single Cooper pair binding energy due to the other particles participating in the pairing. At finite temperature, the critical temperature for superfluidity [1] [8] is given by

$$k_B T_{BCS} = \frac{e^\gamma}{\pi} \Delta \tag{1.42}$$

where $\gamma \approx 0.58$ is Euler's constant and Δ is the zero temperature energy gap. For conventional superconductors, the critical temperature is very small $T_{BCS} \approx 10^{-4} T_F$. In the case of ultracold degenerate gases, for instance, for $|k_F a| = 0.1$ the critical temperature is $T_{BCS} \sim 10^{-7} T_F$, very much smaller than the temperature achieved experimentally.

1.4.6 BEC-BCS crossover

When crossing from BEC to BCS-limit, all quantities changes smoothly and continuosly with the interaction parameter $1/k_F a$. In particular, in this section I show how the wavefunction size and the critical temperature changes with $1/k_F a$ in the crossover region, which extends from $1/k_F a = -1$ to $1/k_F a = +1$. In the BCS-limit the pairing occurs around the Fermi surface in a narrow region of width $\delta k = \frac{\Delta}{\hbar v_F}$ where v_F is the velocity of fermions at the Fermi surface [1][2][8].Therefore, the spatial wavefunction of the Cooper pairs has a strong modulation at the inverse Fermi wave vector $(1/k_F)$ and

an extention of the inverse width of the pairing region ($\sim 1/\delta k >> 1/k_F$), so at $r \to \infty$ it is given by

$$\psi(r) \sim \sin(k_F r) e^{-\frac{r}{\pi \xi_{BCS}}} \tag{1.43}$$

where ξ_{BCS} is the Cooper pairs coherence length and $r = |\vec{r_1} - \vec{r_2}|$ is the modulus of the relative position vector. The pair size or the two-particle correlation length is in general defined as:

$$\xi_0 = \sqrt{\frac{< \psi(\vec{r})|r^2|\psi(\vec{r}) >}{< \psi(\vec{r})|\psi(\vec{r}) >}} \tag{1.44}$$

and is found to be on order of the coherence length in the BCS-limit, i.e

$$\xi_0 \approx \xi_{BCS} = \hbar v_F / \pi \Delta >> 1/k_F \tag{1.45}$$

In the BEC-limit instead the wave-function

$$\psi(r) \sim \frac{e^{-r/a}}{r} \tag{1.46}$$

is in fact the wavefunction of a molecule of size a, and the corresponding two-particle correlation length is thus a. The evolution of the pair size as a function of the interaction parameter is shown in figure 1.5. On resonance the pair size is of the order of $\xi_0 \sim 1/k_F$, about a third of the interparticle distance. Another important quantity which must change smoothly from the BEC to BCS-limit is the temperature at which a long-range order is established, i.e. a phase transition to a superfluid occurs, called the critical temperature. In our case of three dimensional potential a Bose-Einstein condensate is a superfluid. In this BEC regime and in the case of weakly interacting molecules the critical temperature can be expressed also as

$$T_{c,BEC} = 0.22 \frac{E_F}{k_B} \tag{1.47}$$

For stronger interactions, there is a small positive correction to be added to the critical temperature that becomes $\frac{T_c}{T_{c,BEC}} = 1 + 1.31 n_M^{1/3} a_M$. In the BCS-limit instead the critical temperature assume a very small value (see section "BCS-limit"). This means that at the crossover between these two regimes, the critical temperature must assume a local maxima. To determine this value one must know the central density and, in the case of the harmonic trap, we use the local density approximation which consists on assuming that the properties of a gas at $\vec{r}$ are that of a homogeneous gas having the local

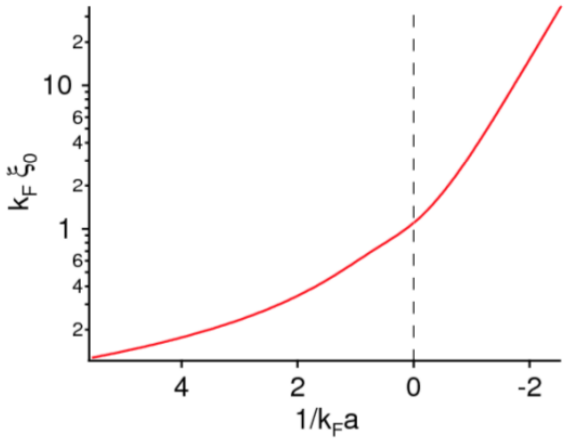

Figure 1.5: Characteristic pair size evolution from tightly bound molecules in BEC-limit ($1/k_F a > 1$) to the long-range Cooper pairs in the BCS-limit ($1/k_F a < -1$) [2]. On the resonance, the pair size is on order of the interparticle distance $\xi_0 \sim 1/k_F$.

chemical potential $\mu(\vec{r}) = \mu - V(\vec{r})$ and Fermi energy $\epsilon_F(\vec{r}) = \frac{\hbar^2 k_F^2(\vec{r})}{2m} = \frac{\hbar^2}{2m}(6\pi^2 n_\uparrow(\vec{r}))^{2/3}$ where $n_\uparrow(\vec{r})$ is the density of atoms in a spin state. At zero temperature, the density profile in the unitarity limit becomes

$$n_{\uparrow,U}(\vec{r}) = \frac{8}{\pi^2}\frac{N_\uparrow}{R_{U_x}R_{U_y}R_{U_z}}\max\left(1 - \sum_i \frac{x_i^2}{R_{U_i}^2}, 0\right)^{3/2} \tag{1.48}$$

with the radii $R_{U_{x,y,z}} = \alpha^{1/4} R_{F_{x,y,z}}$, where α is an universal constant which simply rescales the radii by a factor $\alpha^{1/4}$ and the central density by a factor $\alpha^{-3/4}$ with respect to the ideal degenerate Fermi gases. The critical temperature at unitarity [1] is:

$$T_{c,U} = 0.15 E_F/k_B \tag{1.49}$$

which is actually achieved in the ultracold Fermi gases experiments. It is interesting to note that this temperature is larger than $T_c/T_F \sim 10^{-4}$ typical of conventional superconductors and even larger than $T_c/T_F \sim 10^{-2}$ peculiar of high-T_c superconductors, thanks to the strongly interactions achieved by the Feshbach resonance. For this reason the crossover fermionic superfluid are called "high-temperature superfluid"; scaled to the density of electrons in a metal, this form of superfluid would occur at temperature above the room temperature, even above the melting one [2]. The profile of the critical T_c and pair creation $T*$ temperature as a function of $1/k_F a$ is shown in figure 1.6.

In the region between T_c and $T*$, there are bound pairs which are not yet condensed.

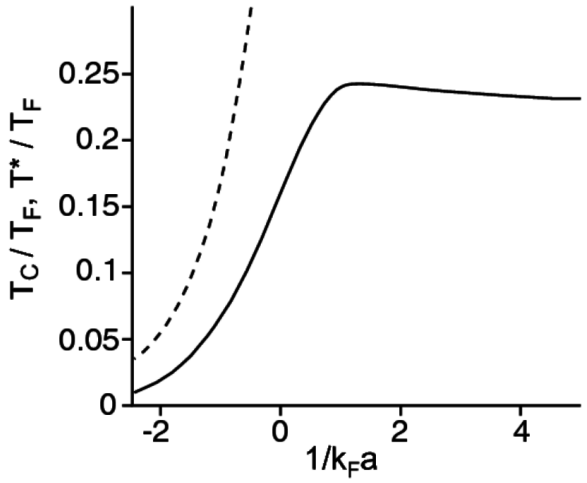

Figure 1.6: Behavior of the superfluid transition temperature (T_c) and pair creation temperature ($T*$) as a function of $1/k_F a$ in the BEC-BCS crossover regime. [2].

1.5 The special case of ^{6}Li

An extraordinary property of fermionic lithium (^{6}Li), which we use in our experiment, is the presence of broad Feshbach resonances between its internal states which permits to finely tune the interaction scattering length by just varying an external magnetic field. The enhanced scattering length at the resonance permits to efficiently evaporate (see "Evaporative cooling") the lithium gases to the quantum degenerate regime and then, by just tuning the magnetic field value, to the directly production of molecular BEC (mBEC). Therefore one can study different physical regime from quantum degenerate Fermi gases to mBEC and thus simulate different many-body phenomena of condensed matter physics. In the following, I firstly describe the level structure of ^{6}Li and then give its Feshbach resonances features.

1.5.1 Level structure

Fermionic lithium (^{6}Li) has in its ground state ($^2S_{1/2}$) a valence electron having a total angular momentum $J = 1/2$, where $\vec{J} = \vec{L} + \vec{S}$ with $\vec{L}$ the orbital angular momentum and $\vec{S}$ the electron spin equals to zero and $1/2$

respectively. At zero external magnetic field, the level energies are given by the eigenvalues of the hyperfine hamiltonian:

$$H_{hf} = a_{hf}\vec{I}\cdot\vec{J} \tag{1.50}$$

where a_{hf} is the hyperfine constant of the level and $\vec{I}$ is the nuclear spin, whose value is one for ^{6}Li. If we define the atom total angular momentum as $\vec{F} = \vec{J}+\vec{I}$, a good basis to diagonalize H_{hf} is the one of the atom momentum quantum number F and of its projection along the quantization axis m_F. As a result, we achieve that the ground state splits in two hyperfine levels $|^2S_{1/2}, F = 1/2\rangle$ and $|^2S_{1/2}, F = 3/2\rangle$ separated by 228.2 MHz. In figure 1.7 is shown not only the ground state hyperfine structure but also that of the excited states $^2P_{1/2}$ and $^2P_{3/2}$ where the hyperfine energy splitting value is indicated [12] [11]. The state $^2P_{3/2}$ hyperfine structure is unresolved as the hyperfine splitting is smaller than its natural width $\Gamma = 5.9$ MHz, while instead the $^2P_{1/2}$ hyperfine sublevels are well-resolved. When an external magnetic field (B) is applied, the hamiltonian is instead given by the sum of the hyperfine hamiltonian and the Zeeman hamiltonian which gives the interaction of the electron and nuclear spins with the magnetic field

$$H = a_{hf}\vec{I}\cdot\vec{J} + g_j\mu_B\vec{B}\cdot\vec{J} + g_i\mu_N\vec{B}\cdot\vec{I} \tag{1.51}$$

where g_j and g_i are the electron and nuclear Lande g-factor respectively, while $\mu_B \approx 1.4$ MHz/G is the Bohr magneton. At magnetic field values $B << a_{hf}/\mu_B$, which is almost 30 G for ^{6}Li, the Zeeman effect is a weak perturbation to the hyperfine structure and $|F, m_F\rangle$ continue to be a good basis. At high field values (larger than 30 G) instead, the Zeeman effect dominates and the electron and nuclear spin decouples. So, F is not anymore a good quantum number while the electronic and nuclear spin projections m_S and m_I are good ones. To find the hamiltonian eigenvalues at intermediate field too, we write it in terms of the creation and destruction operators $\vec{J}_\pm$, $\vec{I}_\pm$ as

$$H = ha_{hf}I_zJ_z + \frac{ha_{hf}}{2}(J_+I_- + J_-I_+) + \mu_B B(g_J J_z + g_I I_z) \tag{1.52}$$

where

$$J_\pm\,|J, m_J\rangle = \sqrt{(J \mp m_J)(J \pm m_J + 1)}\,|J, m_J \pm 1\rangle \tag{1.53}$$

the same is true for $I_\pm$ if we substitute $J \to I$. The hamiltonian eigeinvalues expression is called the Breit-Rabi formula. The profile of the energy of the ground state sublevels versus magnetic field, calculated via Mathematica, are shown in figure 1.8. In our experiment, we use two-state mixtures composed

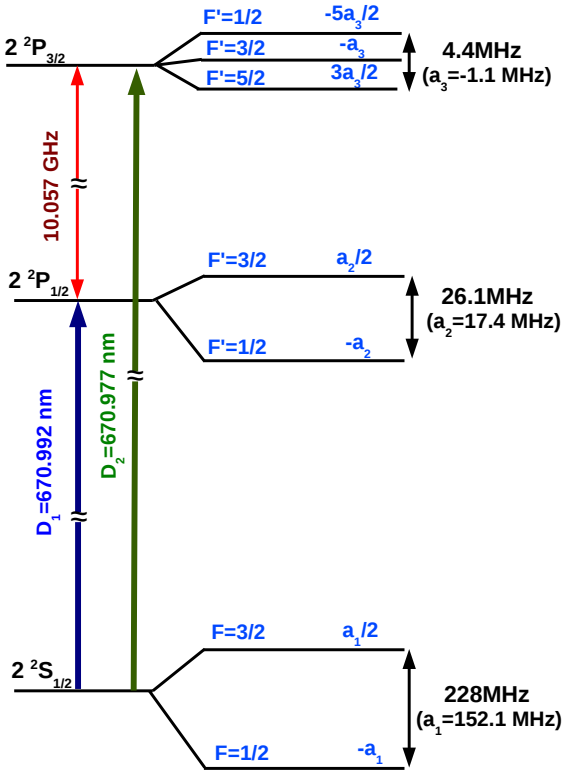

Figure 1.7: The ground ($2^2S_{1/2}$) and excited states ($2^2P_{1/2}$, $2^2P_{3/2}$) hyperfine structure of ^6Li and the corresponding hyperfine energy splitting. The transition $2^2S_{1/2} \rightarrow 2^2P_{1/2}$ (called D_1 transition) and the $2^2S_{1/2} \rightarrow 2^2P_{3/2}$ (called D_2 transition) are also indicated.

of ^{6}Li atoms being in $|1\rangle - |2\rangle$ or $|1\rangle - |3\rangle$ states. The fermionic system I considered in the previous sections was composed of fermions having spin "up" and spin "down", i.e. spin components along the quantization axis equal to $+1/2$ and $-1/2$ respectively. Hereafter, the fermionic particle I consider are the ^{6}Li atoms and the state $|1\rangle$ and $|2\rangle$ or $|3\rangle$ are the analogous of spin "up" and spin "down" states, a kind of "pseudospin" states.

1.5.2 ^{6}Li Feshbach resonances

The ^{6}Li open channel is described by the triplet potential to which corresponds an angular momentum $F = 1$, while the closed one is the singlet potential corresponding to $F = 0$ [4]. The ^{6}Li Feshbach resonances between its internal state $|1\rangle - |2\rangle$ and $|1\rangle - |3\rangle$ are shown in figure 1.9 [13] while

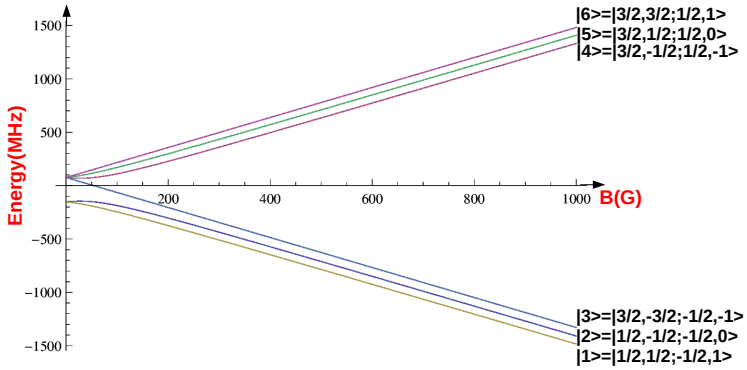

Figure 1.8: Ground state Zeeman sublevels energy as a function of the magnetic field, labeled from $|1\rangle$ to $|6\rangle$ where the quantum numbers indicating the states are $|F, m_F, m_J, m_I\rangle$.

the corresponding properties such the resonance position, width and background scattering length [14], [15] are given in the table 1.10. I note that ^{6}Li Feshbach resonances background scattering length a_{bg} assumes large values, of about $-1600a_0$, when compared to typical a_{bg} on order of hundreds of a_0 for the other alkali atoms. Thus, if the triplet potential of ^{6}Li were just about $\hbar^2/ma_{bg}^2 \simeq h \cdot 415$ kHz deeper, it would support a new bound state. Also, the Feshbach resonance width (Δ) is two or three order of magnitude larger than typical values. The strongly interaction regime $1/k_F|a| < 1$ is thus completely in the universal (unitarity) regime.

1.6 Production of quantum degenerate gases

The atomic gases are produced by heating up in an oven (see next chapter) its solid at very high temperature. So, the first step in producing the quantum degenerate gases is to reduce their velocity after leaving the oven. This is achieved by an interplay between the effect of the laser and magnetic fields on the atoms motion. In order to achieve the quantum degenerate regime, the evaporative cooling is applied, where interactions play a crucial role in the cloud thermalization. Therefore, the following section begins by describing the forces that the light exerts on the atoms, continues considering its application and in the end I explain the evaporative cooling technique.

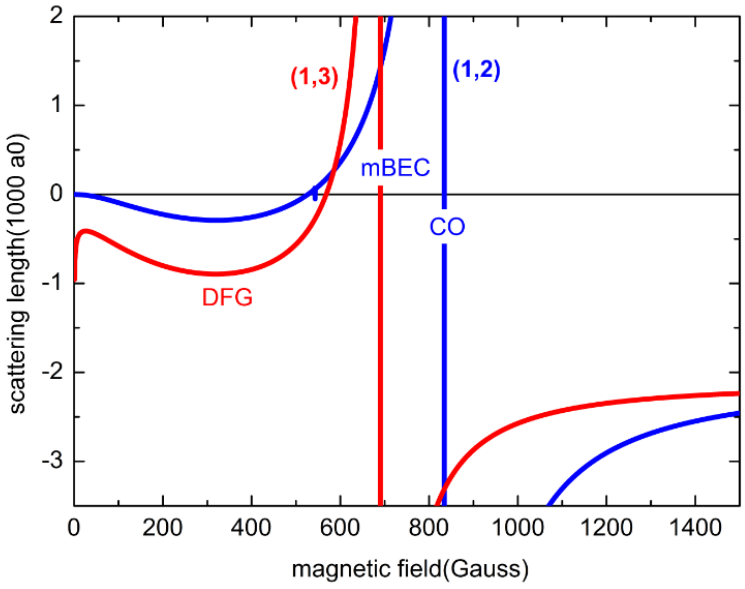

Figure 1.9: Feshbach resonances between $|1\rangle - |2\rangle$ and $|1\rangle - |3\rangle$ internal states of ^{6}Li.

Scattering channel	B_0 $[G]$	Δ $[G]$	a_{bg} $[a_0]$
$\|1\rangle$ $\|2\rangle$	832.18	-262.3	-1582
$\|1\rangle$ $\|3\rangle$	689.68	-116.6	-1770

Figure 1.10: The position, widths and background scattering lengths of the Feshbach resonances between $|1\rangle - |2\rangle$ and $|1\rangle - |3\rangle$ states of ^{6}Li.

1.6.1 The effect of light on the atoms

The force exerted on the atoms by the light field originates from the momentum exchange during the absorption/emission processes. To achieve an expression of this force, I follow the semiclassical approach which consists on calculating the mean force acting on an atom at a position x. This approach is valid only if the atomic wavepackets spatial (Δx) and momentum ($\Delta p = m\Delta v$) spread are sufficiently small but such to satisfy the Heisenberg uncertainty relation $\Delta x \Delta p \geq \hbar$. The atom is considered spatially well-localized in the laser field if $\Delta x \ll \lambda$, where λ is the laser wavelength. If the spread of the Doppler shifts $k\Delta v$ associated to a velocity spread and consequently to a momentum spread is much smaller than the natural width of an excited level Γ , i.e. $k\Delta v = k\Delta p/m \ll \Gamma$, the atom wave-packed is well-

localized even in momentum space [16] [17]. In this semiclassical approach the electric field is taken to be

$$\vec{E_L}(\vec{R},t) = \vec{e}_L \epsilon_L(\vec{R}) \cos\left[\omega t + \phi(\vec{R})\right] \tag{1.54}$$

where $\vec{e}_L$ is the polarization vector supposed independent on R, while the field amplitude $\epsilon_L(\vec{R})$ and phase $\phi(\vec{R})$ depends on R. It can be shown [16] that the average force acting on the atoms, calculated at the rest atom position supposed to be $R = 0$, is the sum of two terms; the dissipative force $\vec{F}_{diss}$ and the reactive one $\vec{F}_{react}$ expressed as

$$\vec{F}_{diss} = -\frac{\hbar\Gamma}{2}\frac{\Omega^2/2}{\delta^2+\frac{\Gamma^2}{4}+\frac{\Omega^2}{2}}\nabla\phi \qquad \text{and} \qquad \vec{F}_{react} = -\frac{\hbar\delta}{4}\frac{\nabla\vec{\Omega}^2}{\delta^2+\frac{\Gamma^2}{4}+\frac{\Omega^2}{2}} \tag{1.55}$$

where $\delta = \omega - \omega_0$ is the laser detuning from the atomic transition ω_0 and $\Omega(\vec{R})$ the Rabi frequecy defined as:

$$\hbar\Omega(\vec{R}) = -\epsilon_L(\vec{R})\vec{d}_{eg} \cdot \vec{e}_L \tag{1.56}$$

For a plane wave whose $\vec{\nabla}\phi = \vec{k}_l$, one finds that the dissipative force varies with δ as a Lorentzian absorption curve centered at $\delta = 0$, at which it assumes the maximum value $\vec{F}_{max} = \hbar\vec{k}_l\Gamma/2$, and having a width $\sqrt{\frac{\Gamma^2}{4}+\frac{\Omega^2}{2}}$ (fig. 1.11a). Defining the intensity parameter $\frac{I}{I_{sat}} = 2\frac{|\Omega|^2}{\Gamma^2}$, one finds also the

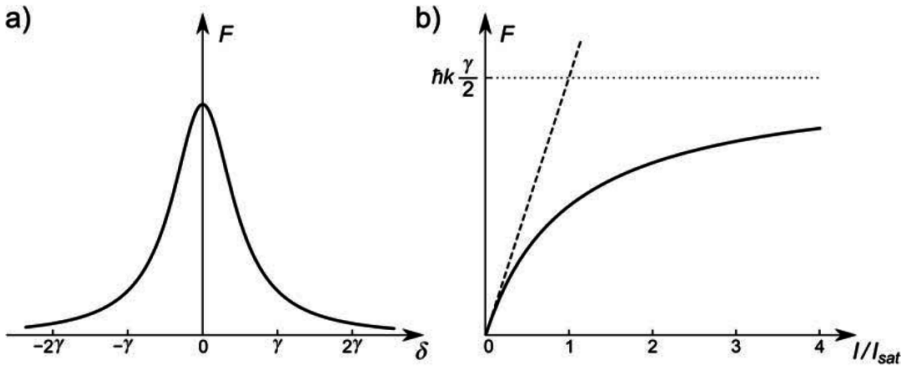

Figure 1.11: The dissipative force profile as a function of the detuning (a) and the ratio I/I_{sat} (b).

dissipative force profile versus this parameter as shown in figure 1.11b. At low laser beam intensity $I/I_{sat} << 1$ the dissipative force is proportional to Ω^2 and thus to the light intensity. At high intensity $I/I_{sat} >> 1$ instead the

dissipative force saturates at its maximum value $\vec{F_{max}}$. Also it can be interpreted as being proportional to the rate of spontaneous emission processes [16], during each of them the atom gains the momentum $\hbar\vec{k_l}$:

$$\vec{F}_{diss} = \hbar\vec{k_l} < \frac{dN_{spont}}{dt} > \tag{1.57}$$

where $< \frac{dN_{spont}}{dt} >$ is the average value of the rate of variation of the excited state population per second due to spontaneous emission process. For a plane wave, the reactive force is instead zero, but in general it varies with δ as a dispersion curve having the same width as the dissipative one. For positive detuning $\delta > 0$ (blue-detuned laser), the laser repels the atoms away from the high intensity region. For negative detuning $\delta < 0$ (red-detuned laser) the force instead attracts the atoms toward the regions of high laser intensities. In contrast to the dissipative force it increases with the laser intensity ($\Omega^2 \propto I$) without saturating. The reactive force can be expressed also as the gradient of a potential appearing so as a conservative force and it is called the "dipole" force

$$\vec{F}_{react} = -\vec{\nabla}U \qquad \text{with} \qquad U = -\frac{3\pi c^2}{2\omega_0^3}\left(\frac{\Gamma}{\omega_0-\omega} + \frac{\Gamma}{\omega_0+\omega}\right) I(\vec{r}) \tag{1.58}$$

The scattering rate of photons by the atoms is

$$\Gamma_{sc}(\vec{r}) = -\frac{3\pi c^2}{2\omega_0^3}\left(\frac{\omega}{\omega_0}\right)^3 \left[\frac{\Gamma}{\omega_0-\omega} + \frac{\Gamma}{\omega_0+\omega}\right]^2 I(\vec{r}) \tag{1.59}$$

1.6.2 Magneto-optical trap (MOT)

MOT configuration

When two counterpropagating laser light at the same frequency ω are sent to an atom whose velocity $\vec{v}$ points in the same direction, for instance, as the left laser (fig. 1.12a), the atom feel a total dissipative force given by

$$\vec{F} \simeq \hbar\vec{k}\frac{\Gamma}{2}\left[\frac{\frac{I}{I_{sat}}}{1+\frac{4(\omega-\omega_0-kv)^2}{\Gamma^2}} - \frac{\frac{I}{I_{sat}}}{1+\frac{4(\omega-\omega_0+kv)^2}{\Gamma^2}}\right] \tag{1.60}$$

which takes into account the Doppler shifts of each laser in the atom reference frame: the right laser frequency is upshifted to $\omega_R = \omega\left(1+\frac{v}{c}\right)$ and the force exerted by it is given by the second term, while the left one frequency is downshifted to $\omega_L = \omega\left(1-\frac{v}{c}\right)$ and the first term gives the force exerted by it to the atom (fig. 1.12b).

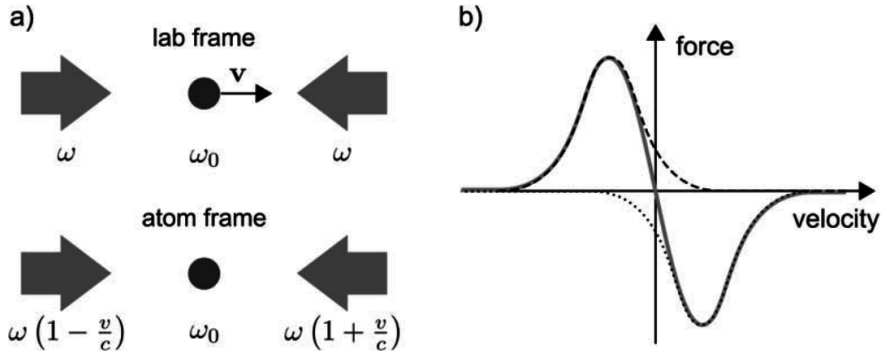

Figure 1.12: The two counterpropagating laser beams sent to a moving atom (a) and the resulting dissipative force as a function of the atom velocity (b) [17].

In the limit of small laser intensity ($I << I_{sat}$), the total dissipative force exerted by the two beams on the atom is

$$\vec{F} = -\beta\vec{v} + O(v^3) \qquad \text{with} \qquad \beta = -8\hbar k^2 \frac{I}{I_{sat}} \frac{\frac{\delta}{\Gamma}}{\left(1+\frac{4\delta^2}{\Gamma^2}\right)} \tag{1.61}$$

where β is the damping coefficient and is positive for red-detuning ($\delta < 0$) giving a dissipative force that lineary reduces the atomic velocity beeing opposite to it (fig. 1.12b), the opposite happens for blue-detuning ($\delta > 0$). We would expect these results as when $\omega < \omega_0$, ω_R is closer to resonance than ω_L so the right laser has higher probability to be absorbed by the atoms and consequently the atoms gain a momentum $\hbar\vec{k_l}$ in the opposite direction of their motion slowing down. This configuration called optical molasses, efficiently cool the atoms but does not provide any spatial confinement of them. The atoms trapping is achieved by using an inhomogeneous magnetic field and a pair (in one dimensional) of counterpropagating red-detuned laser beams polarized σ^+ and σ^-. To show the MOT principle of work, for simplicity, I consider an atom whose angular momentum number of the ground and excited state are $J = 0$ and $J = 1$ respectively (fig. 1.13). Supposing that a linear magnetic field is applied in x-direction, i.e. $\vec{B}(x) = bx\hat{x}$, we achieve a position dependent Zeeman shift of the excited hyperfine states energy

$$E_Z(x) = g_{J'}\mu_B m_{J'} bx \tag{1.62}$$

where $m_{J'} = -1, 0, 1$ are the angular momentum components defined respect to the quantization axis x, $g_{J'}$ is the Lande factor of the excited state, μ_B the Bohr magneton and b the gradient of the magnetic field. For an atom

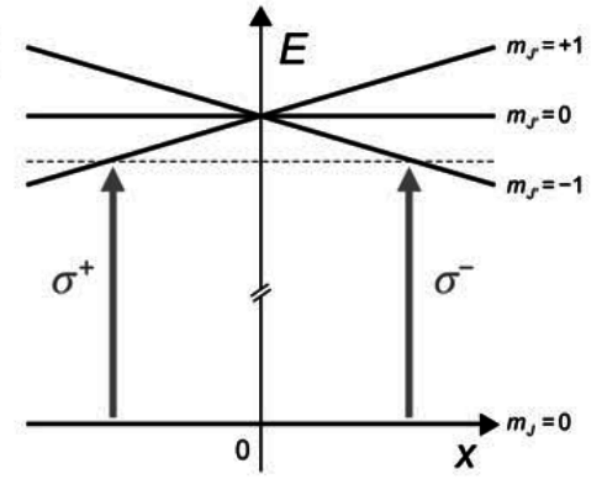

Figure 1.13: The Zeeman energy shift of the excited state $J = 1$ in the presence of magnetic field having a constant gradient and the incident σ^+, σ^- laser light [17].

located at $x > 0$, the transition $|m_J = 0\rangle \rightarrow |m_{J'} = -1\rangle$ is almost resonant with the red-detuned laser beams. As $\Delta m_J = -1$ for this transition, due to the selection rule, these atoms are resonant with the σ^- polarized laser. The atoms experience so a radiation pressure force directed towards the trap center. If instead the atom is located at $x < 0$, the situation is reversed; the transition $|m_J = 0\rangle \rightarrow |m_{J'} = +1\rangle$ is almost resonant with the laser beams but it probably absorbs the σ^+ polarized laser due to the corresponding selection rule $\Delta m_J = +1$. It results in a radiation pressure force which tends to bring the atom at the trap center, opposite to the first one. In fact, for small atom displacement (x) and velocity (v), the resulting force can be expressed as

$$F \simeq -m\omega^2 x - \beta v \tag{1.63}$$

which describes the force acting on a damped harmonic oscillator. This discussion can be generalized in three dimensions.

MOT cooling limit

During the spontaneous decay from the excited state, the atom acquires a momentum $\hbar\vec{k}$ in a random direction, for any emission process. This can be thought as a random walk in the momentum space with unit step equal to $\hbar\vec{k}$ which results in an atom heating with an average squared velocity increasing

$$< v^2 >= v_r^2 \Gamma_{\ scatt} t \tag{1.64}$$

with $v_r = \frac{\hbar k}{m}$ the recoil velocity and Γ_{scatt} the scattering rate of photons. Also the laser intensity fluctuations can contributes in heating the atoms. The equilibrum is achieved when the cooling and heating rate are equals and it happens at the Doppler temperature [16] [17]:

$$T_D = \frac{\hbar\Gamma}{4k_B} \frac{1 + \left(\frac{2\Delta}{\Gamma}\right)^2}{\frac{2|\Delta|}{\Gamma}} \tag{1.65}$$

We would expect for T_D to assume a minimum value because when the momentum of the particles becomes so low that their Doppler shift becomes smaller than the linewidth of the transition, the absorption of light from the counter- and co-propagating light beams becomes equally probable and this cooling mechanism does not work anymore. In fact, a minimum temperature is achieved for $|\Delta| = \Gamma/2$ and is:

$$T_D^{min} = \frac{\hbar\Gamma}{2k_B} \tag{1.66}$$

being equal to $T_D^{min} = 140\ \mu K$ for ^{6}Li.
Doppler temperature originates from considering a two-level atom in a standing wave, but if an atom has a Zeeman ground state structure (as alkalin atoms) and it moves in a polarization gradient light field, sub-Doppler cooling mechanism are possible having as minimum temperature limit:

$$T_r = \frac{\hbar^2 k^2}{2mk_B} \tag{1.67}$$

which corresponds to the recoil of a single photon with momentum k and in the case of ^{6} Li is about $T_r = 3\ \mu$K. However, such very small temperature for ^{6}Li is unreachable with standard sub-Doppler cooling technique due to the unresolved excited state hyperfine structure. To achieve sub-Doppler temperature, in our experiment is implemented a "blue-detuned gray molasses" scheme, which is explained in more details in the third chapter.

1.6.3 Optical dipole trap

In typical ultracold atoms experiment, in the MOT one achieves phase-space density $\rho = n\lambda_{dB}^3 \simeq 10^{-5}$ which is much smaller than the quantum degenerate value $\rho \sim 1$. For this reason the atoms are transferred into a conservative potential in order to perform a further cooling stage called evaporative cooling.

Optical dipole trap

As I explained previously, the dipole force, exerted by focused laser beam, traps the atoms if the laser light is red-detuned with respect to the atomic transition. The disadvantage of this trapping technique is that the atoms scatter the trapping light which causes heating or loss of atom from this optical dipole trap ODT. However, while the trap depth reduces lineary with the increase of the detuning of the light $U \propto I/\delta$, the scattering rate drops off quadratically while increasing the detuning $\Gamma_{sc} \propto I/\delta^2$. Thus by using very far-detuned laser beams, the scattering rate is reduced while sufficiently deep dipole traps are achieved. To efficiently load the atoms from the MOT into the ODT, are sufficient trap depth on order of $1mK$.

I consider here the case of the dipole trap created by a red-detuned Gaussian beam propagating along z-axis. Its intensity varies spatially depending both on the radial r and axial z coordinates as

$$I(r,z) = \frac{2P}{\pi w^2(z)} \exp\left(-2\frac{r^2}{w^2(z)}\right) \qquad \text{with} \quad w(z) = w_0\sqrt{1+\left(\frac{z}{z_R}\right)^2} \tag{1.68}$$

where P is the laser power and $w(z)$ is the radius at which the intensity is diminished by $1/e^2$ with respect to its maximum value. Its minimum value w_0 is called the beam waist and $z_R = \pi {w_0}^2/\lambda$ is the Rayleigh range. The beam waists and Rayleigh ranges determine the region of confinement for the atoms, i.e. the trapping volume. If the thermal energy of the sample $k_B T$ is much smaller than the trap depth U_0 the extension of the trapped cloud is smaller than the trapping volume, which is the case in our experiment. Thus we can expand the Gaussian beam intensity to the second order on r and z around its maximum value I_0, which includes all the constant

$$I(r,z) \simeq I_0\left(1 - \frac{z^2}{z_R^2} - \frac{2r^2}{w_0^2}\right) \tag{1.69}$$

Consequently the dipole potential can be expanded around its minimum value $U_0 = \frac{3\pi c^3}{2\omega_0^3}\frac{\Gamma}{|\delta|} I_0$ and we find

$$U_{dip} \simeq -U_0 + \frac{1}{2}m\omega_r^2 r^2 + \frac{1}{2}m\omega_z^2 z^2 \tag{1.70}$$

where ω_z and ω_r are the axial and radial frequency given by

$$\begin{cases} \omega_z = \sqrt{\frac{2U_0}{mz_R^2}} \\ \omega_r = \sqrt{\frac{4U_0}{mw_0^2}} \end{cases} \tag{1.71}$$

The ratio of the radial to axial frequency is called the aspect ratio $\epsilon = \omega_r/\omega_z = \sqrt{2}\pi w_0/\lambda$. In general it is more than one which means that there is stronger confinement in the radial than in the axial direction and it increases with the beam waist value. In order to strongly confine the atoms in the axial direction too, we can use crossed laser beam or magnetic trapping.

1.6.4 Evaporative cooling

Once the atoms are transfered in an optical dipole trap, we perform the evaporative cooling process in order to cool them to the degenerate regime temperature on order of hundreds of nK. In the ODT, the velocity of the atoms follow initially the Maxwell-Boltzman distribution and the temperature of the cloud is defined by the mean velocity. The idea of the evaporative cooling technique is to lower the trap depth by descreasing the laser intensity, so the atoms having energy larger than the mean, i.e. the tail of the velocity distribution, leave the trap. After the loss of these high-energy particles and if elastic collision are present, the gas is re-thermalized to a new velocity distribution to which corresponds a lower equilibrum temperature. The trap depth is lower slowly enough for the atoms to re-thermalize in order not to loose too many atoms during the evaporative process. High elastic collision rates are very important to re-thermalize the gas during the evaporative cooling. For this reason we perform evaporative cooling in two-state mixture fermions near the Feshbach resonance, where the scattering length is very large (see 'Feshbach resonance'). In principle, the evaporative cooling process can cool the sample down to zero temperature, but the fraction of escaping particles is found to be

$$\frac{N_{free}}{N_{trapped}} \propto e^{-U/k_B T} \tag{1.72}$$

where the ratio $\eta = U/k_B T$ between trap depth and temperature of the gas is called the truncation parameter and is almost $\eta \sim 10$ in our experiment.

Chapter 2

Experimental apparatus and results

In this chapter I will describe the experimental apparatus we use to produce quantum degenerate gases of ^6Li atoms. I will illustrate the optical schemes to produce a Magneto-Optical Trap of ^6Li and to investigate its properties, such as number of atoms and temperature. I will show in detail the set-up to create a pure optical potential where the degenerate regime is achieved for our fermionic gases.

2.1 Laser system

To cool and trap the atoms we use laser beams at 670.977nm, resonant with the $|^2S_{1/2}, F = 3/2\rangle \rightarrow |^2P_{3/2}, F' = 5/2\rangle$ transition. These cooling lights can transfer with a finite probability the atoms in $F = 1/2$ hyperfine state and thus removing them from the cooling cycle. For this reason we use also a repumping beam which repump the atoms from $F = 1/2$ to the cooling transition (fig. 2.1). As the hyperfine splitting in the ground state manyfold is just 228 MHz, the cooling and repumper light are obtained from a single frequency laser source by just appropriately shifting its frequency with acousto-optical -modulators (AOMs). The master laser we use is a Tapered Amplifier High Power Diode Laser (TA-Pro) produced by TOPTICA that gives a maximum power of 400 mW. Using polarization maintaining fibers the light is brought from this table (TA-Pro's table) to the one where all the necessary lights (MOT, Zeeman slower and imaging beam) are generated, called hereafter "the MOT table".

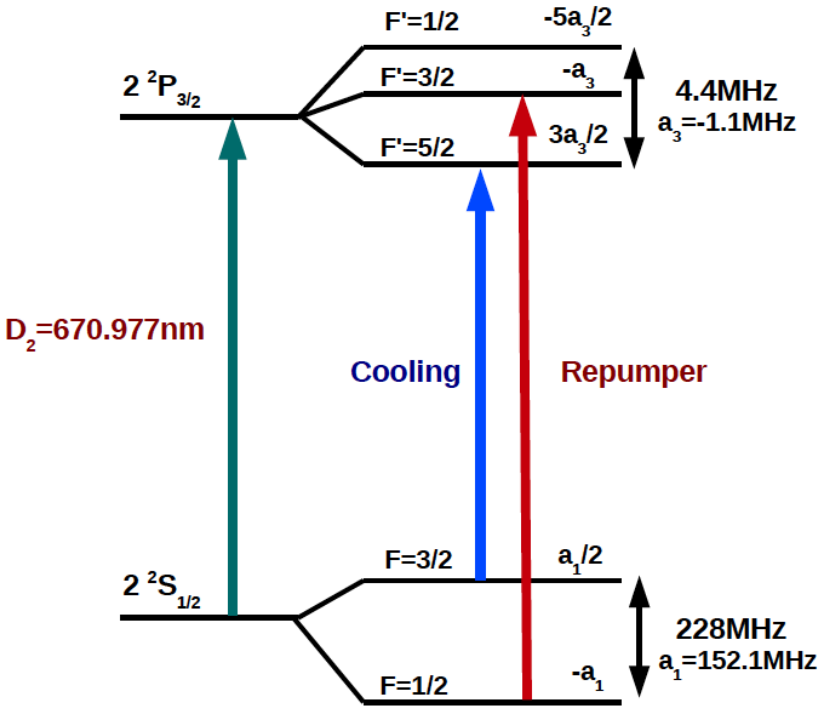

Figure 2.1: Optical transition used to cool the ^{6}Li atoms in the magneto-optical trap.

Lock-in scheme

The D_2 laser is frequency locked at the cooling transition $F = 3/2 \rightarrow F' = 5/2$ line through a +140MHz double passage AOM by saturated absorption spectroscopy with frequency modulation technique, using an Electro Optic Modulator at 12 MHz. The details of the lock-in scheme can be found in the Master Thesis [20].

2.1.1 Optical set-up to produce MOT and Zeeman slower lights

In figure 2.2 is shown a scheme of the frequency shifts: the D_2 light entering the MOT table is shifted of around -205 MHz from the resonance $F = 3/2 \rightarrow F' = 5/2$, which is given by the sum of the frequency shift achieved by the double passage AOM of the locking scheme and of another AOM at around +75 MHz placed in the TA-Pro's table, called the switch AOM (see "Experimental set-up and the characterization of ^{6}Li gray molasses" subsection). The D_2 laser light is then divided in two parts: the cooling and repumper light, that follow different optical path (fig. 2.3). The

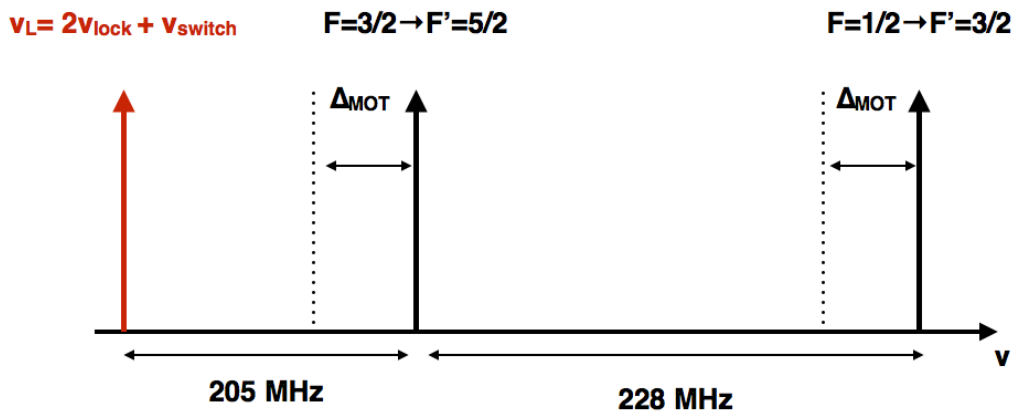

Figure 2.2: Frequency scheme of the experiment for the cooling and repumper light. The laser light entering the MOT table is frequency locked at -205 MHz from the resonance $F = 3/2 \rightarrow F' = 5/2$. MOT laser beams frequency can be further shifted from the resonance at a quantity Δ_{MOT} by just varying the frequency of the respective AOM.

cooling light passes twice through an AOM with center frequency at +90 MHz before injecting the corresponding tapered amplifier MOPA. The light power amplifiers (BoosTA, Toptica) give a maximum output power of about 400 mW for an input power of 28 mW. The repumper light instead passes twice an AOM with a center frequency of +200 MHz and then is sent to its MOPA. To obtain a frequency difference of 228 MHz at resonance ($\Delta_{MOT} = 0$) between the cooling and repumper light, the AOM frequencies are set at +91 MHz and +205 MHz respectively. Both the cooling and repumper light are overlapped to a non polarized 50:50 beam splitter NPBS, where two output beams are achieved: one for the Zeeman slower (part of the experimental apparatus, see section 3.4) and one for the MOT. The Zeeman slower light frequency is shifted with a double-pass AOM with a center frequency of -200 MHz and then is injected to another optical fiber to reach the experimental apparatus, i.e. both its repumping and cooling frequency are shifted -400 MHz with respect to the MOT lights $\nu_{slower} = \nu_{MOT} - 400$ MHz. We inject part of the light of the slower into an optical fiber and prepare the imaging light on another breadboard. In particular, to create the imaging light resonant with the $F = 3/2 \rightarrow F' = 5/2$ transition, we make use of an additional AOM to compensate the shift required for Zeeman slower. The MOT light instead is splitted in three different paths, one for each spatial direction with each of them sent to a polarization-maintaining optical fiber to reach the experimental apparatus. Independent shutters are used for MOT beams

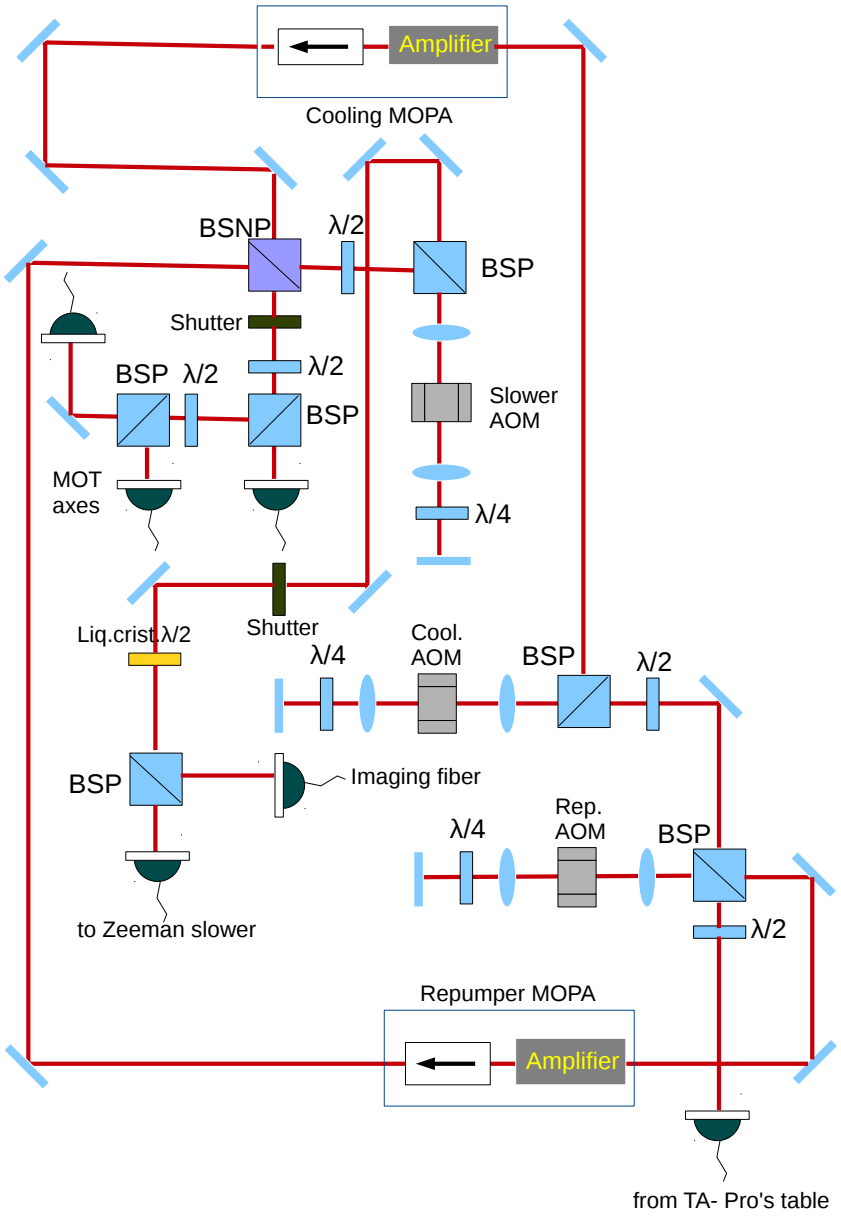

Figure 2.3: Optical scheme to produce the cooling and repumper light.

(Uniblitz), imaging (electromechanical shutter) and slower light (Uniblitz plus AOM deflection). All the fibers are stabilized in polarization by means of $\lambda/2$ positioned at their entrances. We can control the detuning of MOT's beams Δ_{MOT} by changing the AOM shifts before the MOPA amplifier.

2.2 Absorption imaging of cold atoms at low and high magnetic field

In our experiment, the number of atoms in each of the three lowest spin states, i.e. $|1\rangle$, $|2\rangle$ and $|3\rangle$ of ^{6}Li, as well as the sample temperature, are determined using absorption imaging. In this chapter, I will describe the actual experimental set-up for the preparation of imaging light at low and high magnetic field which corresponds to different interaction regimes.

2.2.1 Absorption imaging

The main tool that we use to investigate our sample is absorption imaging. A weak ($I << I_{sat}$) resonant laser beam is sent to the atoms which absorbs it creating a shadow cast on the imaging light recorded with a CCD camera. This image represents the projection of the atomic cloud in the plane orthogonal to the view axis. In our system, the imaging pictures are taken either in the vertical or horizontal direction by means of two independent optical set-up. Both the vertical and horizontal absorption beams can be quickly switched off and on by a AOM. Typically, a sequence of three pictures is recorded: the first one with the atomic sample, the second picture without the atoms (the reference picture), and the third one is a "background" picture, without the atoms and the imaging beam. The latter takes into account all the effects due to spurious light sources and is substracted from the other two. If, for example, the imaging axis is the z-axis, then the atomic density integrated along z is given by

$$\hat{n}(x,y) = \int n(x,y,z)dz = -\frac{1}{\sigma}\ln\left(\frac{I_t - I_{bg}}{I_0 - I_{bg}}\right) \tag{2.1}$$

where I_t and I_0 are the trasmitted and incident beam intensity respectively, I_{bg} is the intensity corresponding to the "background" imaging and σ is the resonant absorption cross-section. In our case, σ takes different values for the imaging in vertical and horizontal direction. The reason is that the vertical imaging light at high magnetic field is σ^--polarized along the quantization axis (the Feshbach field axis) while the horizontal imaging beam is lineary polarized, so the value of sigma for the horizontal imaging is reduced by a factor of 2 with respect to the vertical one given by:

$$\sigma_{vertical} = \frac{3\lambda^2}{2\pi} \tag{2.2}$$

In order to extrapolate the number of atoms corresponding to each CCD pixel (labeled with i,j), the equation 2.1 has to be corrected by the area A of

a single pixel and by the magnification M (set by the optical system):

$$\hat{n}_{i,j} = -\frac{A}{\sigma M^2} \ln\left(\frac{I_t - I_{bg}}{I_0 - I_{bg}}\right) \tag{2.3}$$

Summing $\hat{n}_{i,j}$ over all pixels, we get the total atom number. In the case of a thermal gas, the two-dimensional density is fitted with a Gaussian distribution while in the case of mBEC only the wings of the density distribution, which gives the non-condensed part (thermal) density, are fitted with the Gaussian one. Due to the absorption of photons from the imaging beam the atomic cloud heats up very quickly which destroys the ultracold sample and consequently we have to prepare a new ultracold atom cloud after each imaging cycle. The absorption imaging sequence starts in general when all MOT lights and magnetic fields are switched off. The cloud expands according to its momenta and the interaction energy is transformed into kinetic energy in the expansion. We calculate the temperature of the thermal cloud from the width of distribution after time of flight (t_{exp}) as:

$$\sigma = \sqrt{\sigma_0^2 + \frac{k_B T}{m} t_{exp}^2} \tag{2.4}$$

We take different images for different time of flight (indicated also with TOF) and, by fitting σ as a function of TOF with this function, we recover the cloud temperature. When instead the sample expands in a magnetic field after being trapped in the optical dipole trap, the temperature is not recover by the free ballistic expression as we take into account the effect of the magnetic field too [2].

2.2.2 Imaging light preparation

Thanks to the Feshbach resonances we are able to study different physics regime found for different values of magnetic field B, passing from zero to high B values. To image the cloud at this range of magnetic field we have to compensate for the corresponding Zeeman shifts. The main issue that we have to deal with is that, the fast switching off of high magnetic fields, is not straightforward for our apparatus, due to both inductance of our coils and the auto inductance of the chamber. Furthermore at high field we may use non-destructive phase contrast imaging, sensitive to the single spin state, to address the physics close to the Feshbach resonance [23]. The optical scheme we developed is reported in figure 2.4, whose disadvantageous is that it permits to produce imaging light for restricted values of magnetic field. So, during my thesis work I design and develope a versatile optical sheme

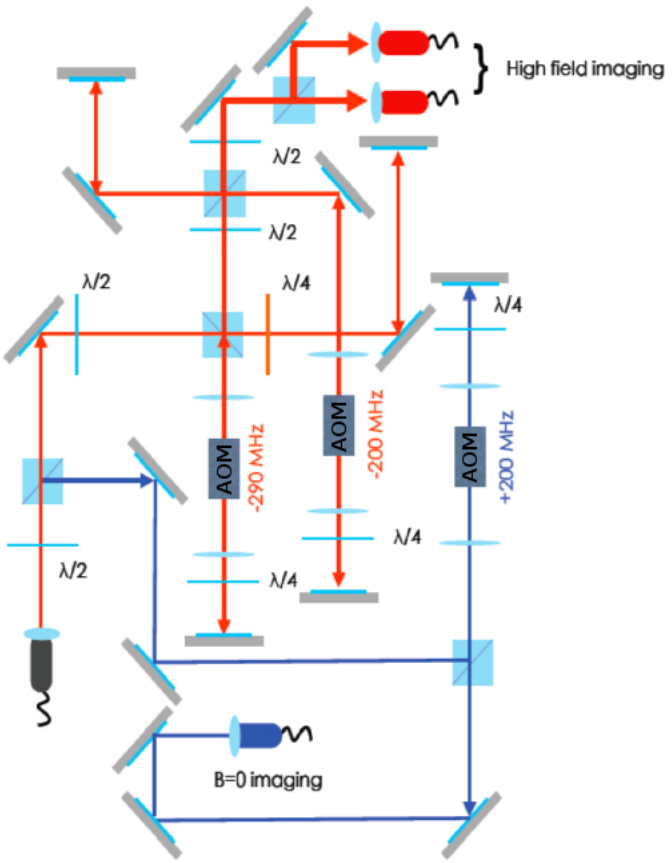

Figure 2.4: Optical setup for zero and high field imaging [21].

for imaging in a larger range of magnetic field values as I will show in the next chapter. To perform 0 field imaging, we need to compensate the shift of the slower light and the MOT detuning with respect to the D_2 transition, unresolved in its Zeeman substates. Instead for high values of the magnetic field, we image the closed atomic transition $|m_j = -1/2\rangle \rightarrow |m_{j'} = -3/2\rangle$. At a magnetic field value of 800 G, for instance, the Zeeman shift is -1100 MHz so the required frequency shift to be added to the slower's detuning is -700 MHz and this is achieved by a double-pass red-detuned AOM of -350 MHz frequency. The value of the AOM's shown in the figure 2.4 are for the imaging at 840 G and 690 G.

2.3 The oven and the science chamber

The heart of the experiment is an Ultra-High-Vacuum (UHV) system, to isolate cold atoms from hot thermal background atoms, which is composed of two principal parts: the oven assembly where the atomic vapor are produced and the science chamber where the atoms are trapped and cooled to the degenerate limit as shown in figure 2.5. These two regions are connected by a Zeeman slower tube long 56cm and by a differential pumping stage.

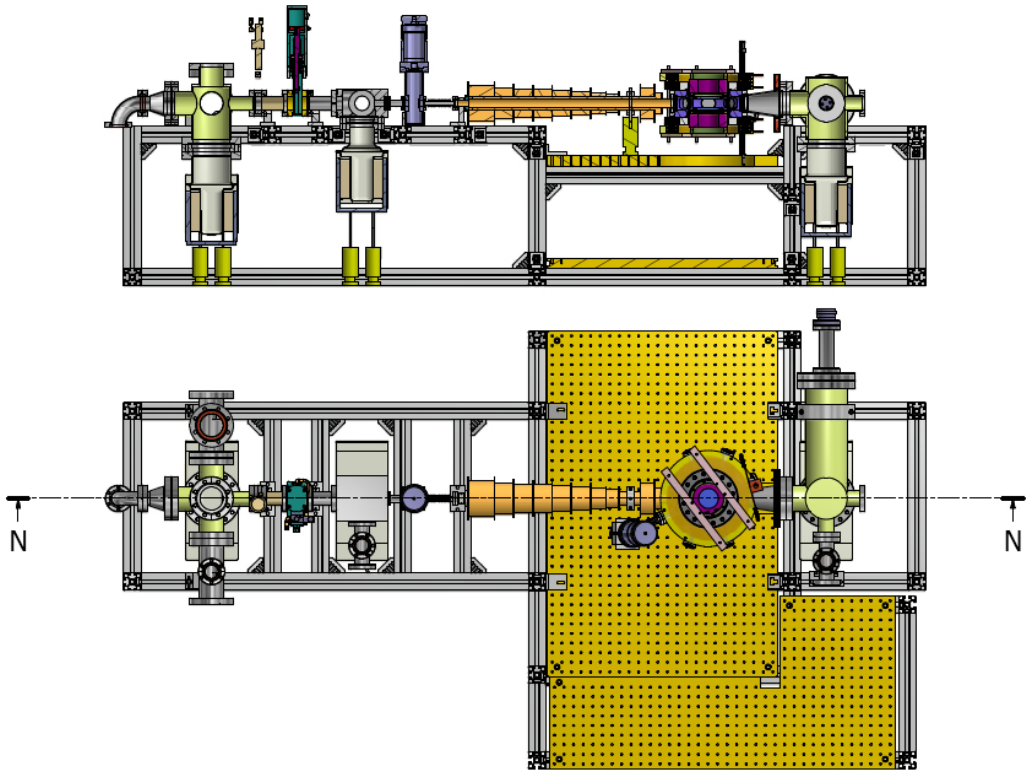

Figure 2.5: The vacuum system consisted on an oven and a science chamber connected by the Zeeman slower and a pumping section.

The oven

At room temperature, lithium is a solid so to achieve its atomic vapor we heat up in an oven to almost 400^0C a source of bulk composed of about 10g of ^{6}Li with purity of 99%. The atomic vapor coming out the oven and entering in the system is collimated by two apertures: the first one, called nozzle, is adjustable in its position permitting so to achieve a better alignment of the

atomic beam with the science chamber and is generally held at a temperature of 460^0C. After it a second regulable aperture, a copper plate called the cold plate, is kept cold using a Peltier cell[1]: hot atoms with misaligned direction with respect to the science chamber will strike and be stuck onto it and they will be stopped before entering the rest of the experiment. A pneumatic shutter is used to stop the atomic beam preventing it from entering the Zeeman slower and it is kept closed after loading the MOT. A differential pumping stage is also used to provide a pressure drop of about three order of magnitude from almost 10^{-8} mbar in the oven to almost 10^{-11} mbar in the science chamber.

Science chamber

The chamber 2.6 is a spherical octagon from Kimball Physics with a large optical access among different directions guaranteed by six CF40 (view diameter of 38 mm), ten CF16 viewports (view diameter 16 mm) and two rientrant CF100 viewports (view diameter of 90 mm). The pressure in the

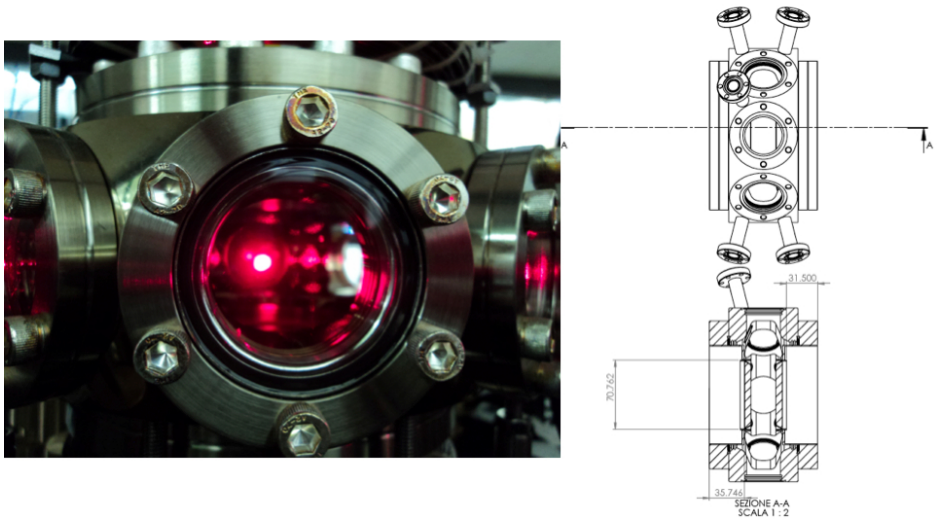

Figure 2.6: On the right: draw of the main vacuum chamber. On the left: fluorescence imaging of the atomic cloud in the MOT seen outside viewports.

UHV system is below of $P \leq 10^{-11} mbar$ and is reached and maintained by

[1]A Peltier cell is formed by two p and n doped semiconductor materials connected with each other by a thin copper plate. Based on Peltier effect, the cell is able to transfer heat from a junction to another when a current is fluxed in the copper circuit.

ionic pumps after the science cell and titanium sublimators. The system is descibed in more details in the [20].

2.4 Zeeman slower and magneto-optical trap

In figure 2.7 are shown the configuration of the MOT, gray molasses, the slower and the ODT laser beams across the science chamber. A flux of

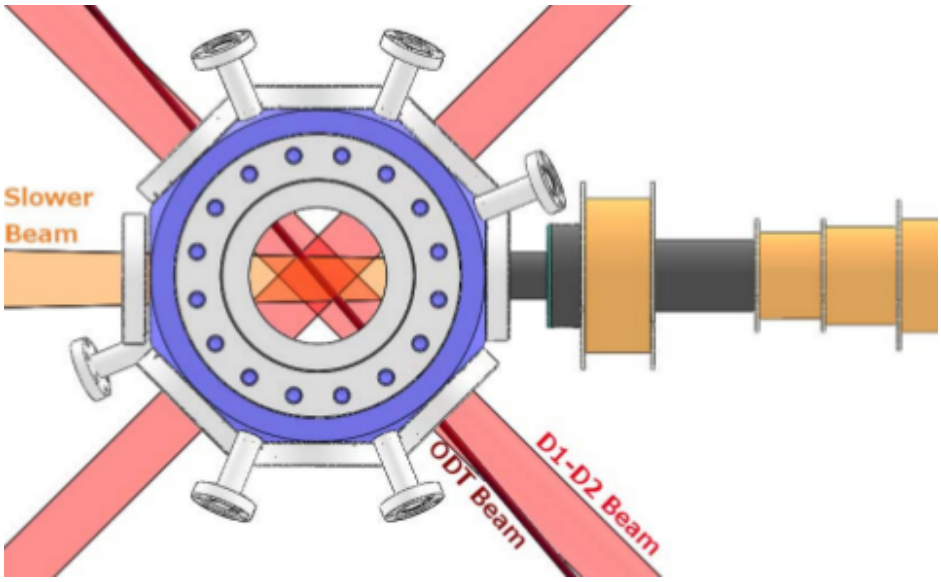

Figure 2.7: Top view of the science chamber showing the MOT/gray molasses beam (red), the slower beam(orange) and the ODT beam(brown)

atoms of about 10^{10} atoms/second entering the Zeeman slower have a mean velocity almost 800 m/s which is reduced to almost 30 m/s thanks to the combined effect of the slower magnetic field and a counter-propagating red-detuned laser beam. Such final velocity value is less than the MOT capture velocity of 60 m/s permitting to efficiently load the MOT. In 4 seconds we are able to load a MOT of 10^9 atoms and achieve temperatures on order of mK with a corresponding phase space density of 10^{-5}.

2.4.1 Zeeman slower

The ^{6}Li atoms leaving the oven follow a Maxwell-Boltzman velocity distribution with root mean square velocity for each direction around 800 m/s which is higher than the MOT capture velocity around 60 m/s. Consequently, we have to reduce it in order to efficiently load the atoms into the

MOT. We achieve lower velocity thanks to the radiative pressure of a counter-propagating red-detuned laser beam exerted on the atomic cloud. The atoms moving in the opposite direction of the incident light see a larger laser frequency, due to the Doppler effect, almost resonant with the atomic transition maximizing so the slowing force (chap.1). Once the atoms are slowed the Doppler effect is reduced and consequently the light pressure force becomes lower. To maintain the resonance condition, even when the atoms are slowed down, we apply an external magnetic field and this configuration is called the Zeeman slower. This magnetic field is designed such that the Zeeman energy shift of the cooling transition compensate the Doppler shift satisfing so the resonance condition $\delta = 0$ where

$$\delta = \omega - \omega_0 - \vec{k} \cdot \vec{v} + \frac{\Delta E_{zs}(B)}{\hbar} \tag{2.5}$$

with ω the laser frequency, ω_0 the atomic transition frequency on which the Zeeman slower is working, ΔE_{zs} the hyperfine splitting of the cooling transition depending on the magnetic field B and $\vec{k}\cdot\vec{v}$ the Doppler shift. Since ^{6}Li enters the strong field (Paschen-Back) regime at low magnetic field we can write $\Delta E_{zs} \simeq \mu_B B$. We designed the slower such that to get a constant deceleration along the direction of propagation of the atoms, which means that the atoms velocity varies as $v^2(x) = v_i^2 - 2ax$, i.e. being dependent on the atoms position along the Zeeman slower x-axis (fig.2.5). From the resonance condition we obtain that also the Zeeman slower magnetic field must be also position dependent satisfing

$$B = \frac{\hbar}{\mu_B}(\delta_0 + k\sqrt{v_i^2 - 2ax}) \tag{2.6}$$

where $\delta_0 = \omega - \omega_0$. In our experiment the Zeeman Slower is working on the transition $|^2S_{1/2}, m_j = 1/2\rangle \rightarrow |^2P_{3/2}, m_j = 3/2\rangle$ induced by a σ^+ polarized laser beam with direction of propagation parallel to the direction of the magnetic field inside the slower. The fast atoms are the first ones to be slowed due to their great Doppler effect, while the slower ones will be captured in the latest part of the tube. For our Zeeman slower the initial mean velocity is almost 800 m/s giving an initial Doppler shift at the first coil of almost 1.1x10^3 MHz, while the red-detuning of the Zeeman slower light is equal to -400 MHz. The frequency difference of about 700 MHz must be compensated by the Zeeman energy shifts, which requires a magnetic field of almost 500 G. The total magnetic field of the slower is produced by nine coils directly winded on the slower tube and do not need high electric power to be generated reducing so the heating of the apparatus. The cooling of coils is provided by an inner channel below the coils themselves, where water circulates after

being pumped from a chiller. In figure 2.8 are shown the simulated and measured magnetic fields for each coil. We note that the first three coils have value slightly different from the computed ones, so to compensate it we run these coils on independent suppliers and optimize the loading of the MOT. Its last coil has a sign inverted magnetic field in order to permit the

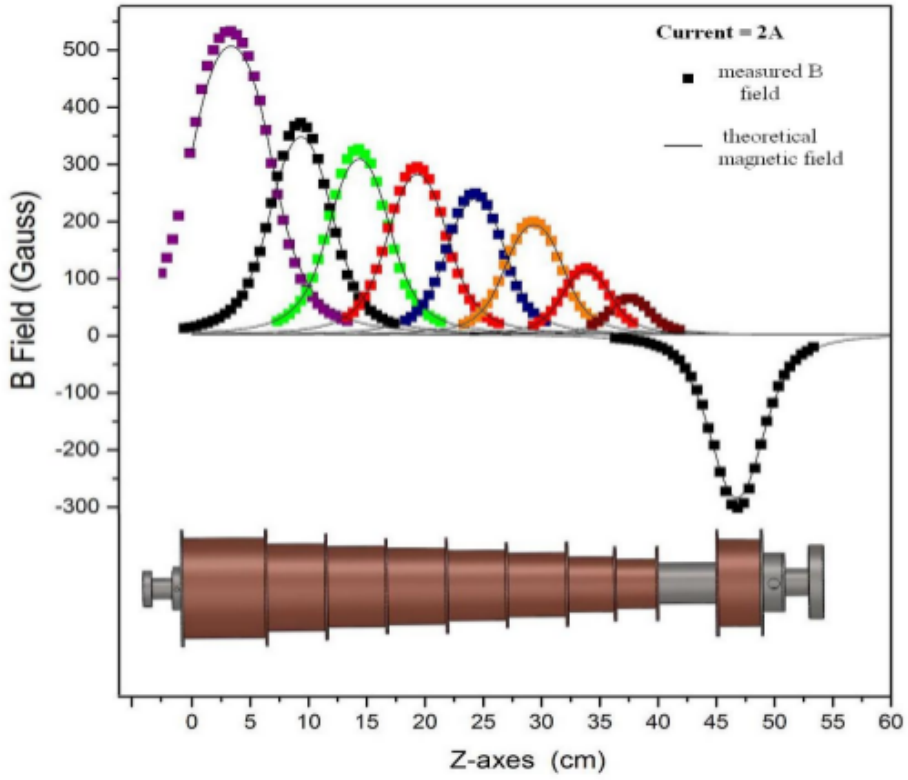

Figure 2.8: The slower simulated and measured magnetic fields plotted for each coil.

slowed atoms coming out of the Zeeman slower not to be anymore resonant with the counter propagating beam allowing so a better loading of the atoms in the MOT. The disadvantage of this configuration is that it produces a flip of the atoms spin where the magnetic field changes its sign as at this position m_j is no more a good quantum number and the slower transition is no longer closed. Atoms can escape the cooling cycle and fall in the state $|F = 1/2\rangle$ of the ground state. So, in addition to the cooling laser light we use repumper light which brings back the atoms into the cooling cycles In table 2.9 are shown the detuning and the power of the cooling and repumper laser beams of our Zeeman slower. The relative percentage of cooling and repumper light are due to the intrinsic design of the optical scheme: reducing

$\delta_{0,\ Cool.\&Rep}$	$P_{Cooling}$	$P_{Repumper}$	Final velocity
$-400\ MHz = -68\Gamma$	$50\ mW$	$50\ mW$	$\sim 30\ m/s$

Figure 2.9: Our Zeeman slower parameters, i.e. the counter-propagating light detuning, the cooling and repumper light intensity and the velocity obtained at the end of the Zeeman slower.

the repumper intensity on the Zeeman slower beam would reduce also the repumper intensity on the MOT as can be noted in figure 2.3. The final velocity obtained at the end of the Zeeman slower 30 m/s is less than the MOT capture velocity almost 60 m/s allowing so a good MOT loading.

2.4.2 Magneto-optical trap

MOT configuration

In our experiment, the MOT light configuration is composed of three mutually orthogonal retro-reflected laser beams with polarization σ^+/σ^- working on the D_2 transition. These laser beams have a $1/e^2$ beam radius of 1.5 cm and a maximum peak intensity of $7I_s$, with $I_s = 2.54mW/cm^2$ the saturation intensity of the D_2 transition. Each beam contains a cooling and a repumper light such that a closed cooling cycle is achieved. The magnetic field instead is a quadrupole one generated by a pair of coils in anti-Helmholtz configuration giving a magnetic field gradient of 20 G/cm at a current I = 20 A. They are mounted around the two reentrant CF100 viewports along z-axis and are shielded with a non magnetic plastic support, which allows water to circulate close to them and have sufficient cooling. Each coil has an inner diameter of 70 mm and has 6 and 8 horizontally and vertically windings respectively, realized with a copper wire with a rectangular section of 1 x 3 mm. .

MOT experimental results

In our case, the cooling beam is detuned -9Γ from the $|F = 3/2\rangle \rightarrow |F' = 5/2\rangle$ transition, while the repumper one is detuned -6Γ from the $|F = 1/2\rangle \rightarrow |F' = 3/2\rangle$ transition with $\Gamma = 2\pi \cdot 5.87$MHz and the ratio of the cooling to repumper light power is 3:2. The large detunings are choosen such that to maximize the number of the trapped atoms but these detunings values do not minimize the temperature. In fact, after typically 8 seconds of loading we have a large number of atoms of $2x10^9$ but at a temperature around 2.5 mK, which is larger than the minimum Doppler temperature equal to 137.6

μK for ^{6}Li. To reduce further the MOT temperature, the D_2 MOT is compressed by decreasing the detuning of both the cooling and repumper light to -3Γ. This leads to a larger photon scattering rate Γ_{scatt}, so simultaneously we reduce the intensity of both the cooling and repumper light to about 1% of the initial value at the same time. This compressed MOT (CMOT) procedure results in a temperature drops to about 500 μK and in a loading atomic number N_0=1.6x10^9.

2.5 Feshbach and curvature coils

In our experiment we use two-state mixture composed of $|1\rangle$ and $|2\rangle$ states. To tune the scattering length between them, we add two-coils, called Feshbach coils, in quasi-Helmholtz configuration to generate the desired offset magnetic fields. These coils together with some curvature coils, provide an axial confinement for the atoms in $|1\rangle$ and $|2\rangle$ state, which is useful where the atoms are trapped in the optical dipole trap as the corresponding axial confinement is much weaker than the radial one as I will describe in the next section.

2.5.1 Feshbach coils

To make use of the great possibility that the ^{6}Li Feshbach resonances offer to explore different physics regimes from BEC to BEC-BCS crossover, we add a pair of coils mounted around the flanges of the reentrant viewport to generate offset magnetic fields up to 1000 G. These Feshbach coils (fig. 2.10), placed in a quai-Helmholtz configuration, produce a magnetic field that has a maximum in the radial direction, while in the axial direction there is a field minimum at the center. As we use $|1\rangle$-$|2\rangle$ state mixture, that for $B > 30$ G minimize their energy at high magnetic field, the atoms feel a confining potential in the radial direction and an anticonfining potential in the axial direction. At 180 A corresponding to B around 840 G, they provide a radial magnetic curvature of about 3 G/cm^2, which gives a radial frequency for ^{6}Li atoms in the lowest hyperfine states $|1\rangle$ and $|2\rangle$ of 10 Hz. These coils are made of kapton insulated wire having a section of 4.6x4.6 mm and a hollow core for water circulation and cooling. Each coil has 8 vertical and 7 horizontal windings that are connected to a 200 A power supply [2]. The magnetic field of these Feshbach coils is stabilized in current by a PID controller whose input is connected to a current trasducer placed on one of the wire connecting the power supply to the coils. The digital feedback loop of

[2]Model SM 15-200 D, Delta Elektronika.

the PID controls the current circulating in the coils and correct its value if it is different from the value defined by calibrating the magnetic field. To calibrate the magnetic field we send a Radio-Frequency rectangular π-pulse to the atoms in the state $|1\rangle$, for instance, transfering them to the state $|2\rangle$; at a certain radio-frequency the atoms are almost all in the state $|2\rangle$ and from the Breit-Rabi formula we find to which magnetic field value corresponds this transition frequency. The magnetic field stability instead is determined by applying Radio-Frequency rectangular π-pulses of increasing duration on a polarized Fermi gas: when the width of the obtained spectrum is above the Fourier width $\delta\nu = 1/\Delta t$ set by our interrogation time Δt we deduce that the spectrum is dominated by noise and fluctuations of the field knowing the correspondence $\delta\nu = \delta B \Delta\mu/h$ where $\Delta\mu$ is the difference between the magnetic moments of the state $|1\rangle$ and $|2\rangle$ and δB the magnetic field inhomogeneity. The magnetic field stability is checked at different values of the magnetic field and is relatively high $\Delta B/B = 10^{-5}$. Since the Zeeman slower at the MOT position produces an axial magnetic field gradient, in order to compensate for it, we use compensation coils placed on the other side of the Zeeman slower. There are also other compensation coils, mounted around each axis, that eliminates any spurious magnetic field and both of them allow to adjust the spatial position of the quadrupole center.

2.5.2 Curvature coils

Thanks to a relay system, mounted in series to the lower coil of the MOT and in parallel to the upper one, we can switch the configuration of MOT coils from anti-Helmholtz to quasi-Helmholtz configuration, so that the magnetic curvature field is summed to the Feshbach magnetic field. For the $|1\rangle$ and $|2\rangle$ states the curvature coils provide a trapping along the horizontal axis with stimated trapping frequency of $\omega_{trap} = 2\pi \cdot 16$ Hz, while in the vertical direction (along the gravity) the atoms in this state feel an antitrapping potential corresponding to an imaginary frequency $\omega_{anti} = 2\pi i \cdot 16 \cdot \sqrt{2}$ Hz. The curvature coils we use are placed in the re-entrances of the vertical windows of our vacuum chamber.

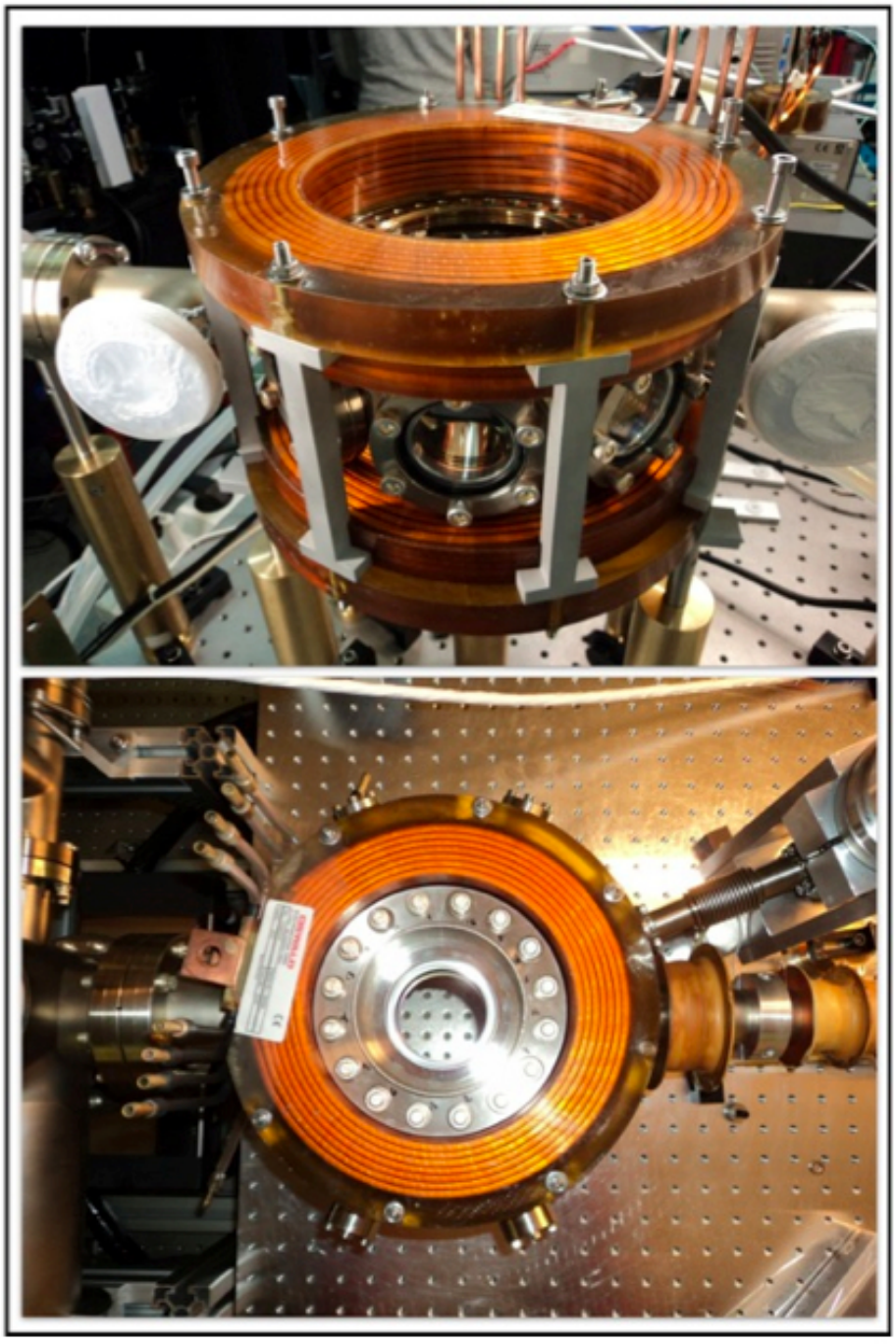

Figure 2.10: Pictures of the Feshbach coils.

2.6 Optical dipole trap

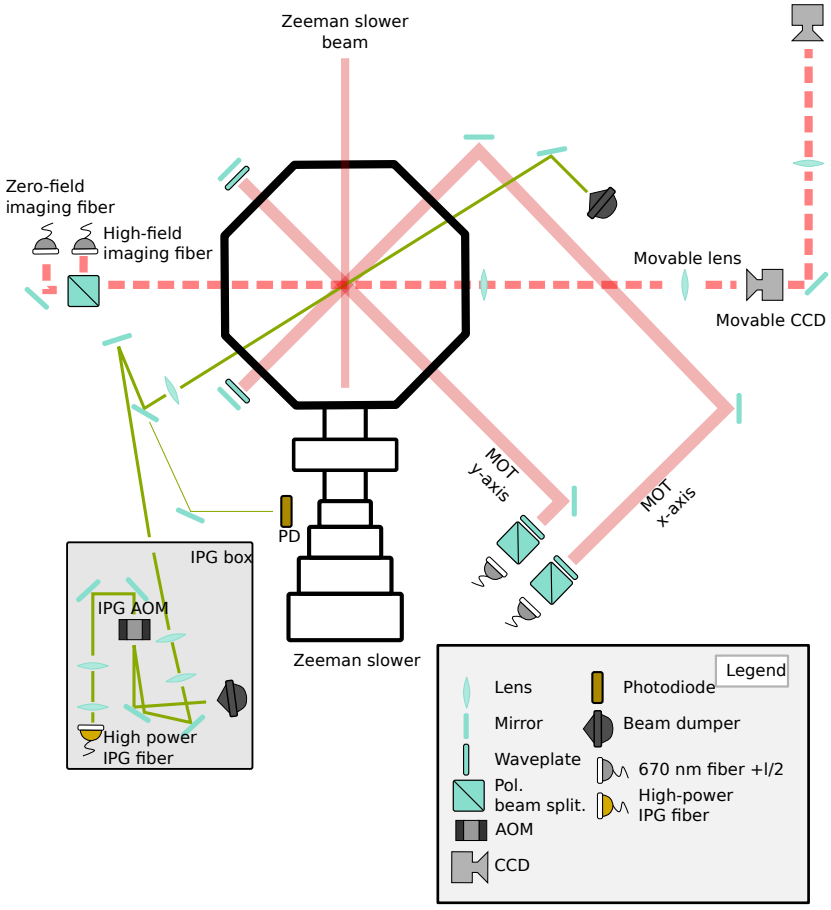

Figure 2.11: Sketch of the optical scheme around the science chamber. The two horizontal MOT beams are shown in faded red and the IPG's in green. The Zeeman slower beam is coming from above and is also shown in faded red, while the dotted lines are the imaging beams. The box where the IPG is brought towards the UHV apparatus is shown in the bottom left corner.

After cooling the atoms in the D_2 CMOT at 500 μK, we transfer them in an optical dipole trap, where we evaporate down to the degenerate limit with corresponding temperatures on order of hundreds of nK. I will describe here the main properties of our ODT while the experimental procedure applied to achieve degenerate temperature is explained in the next chapter. We use a single-beam red-detuned optical dipole trap generated by a 200W multi-mode ytterbium fiber laser (IPG laser) with a central wavelength of 1073 nm and with almost a 3 nm broadening, whose initial power is set at 120W.

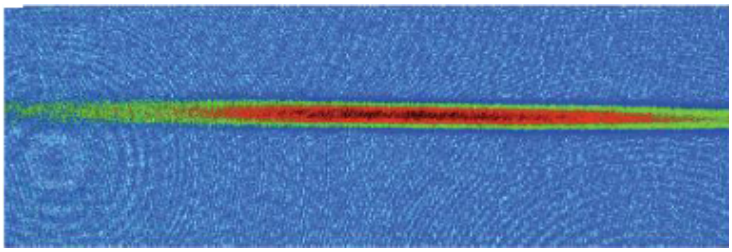

Figure 2.12: Imaging of atoms in the IPG trap.

To handle the IPG high power we use the optical scheme represented in figure 2.11. Because of high power, the beam is made pass through a single passage AOM without focusing and with a collimated waist around 1 mm. The major part of the optical path is held in a box under a continuous flux of air, to avoid deposition of dust on optical elements. The beam passes through an hole on one of the walls and then is brought to the science chamber and focused onto the atoms with a waist of 45 μm both in the x and y direction. The beam passes through the cell from one of the MOT windows, with an angle of 7° respect to the MOT beam. We need to stabilize the IPG power because laser intensity fluctuations may cause exponential heating of the trapped atoms due to parametric heating excitation [22]. This was achieved by using a photodiode, an AOM and a PID controller. At full power the ODT has a depth around 3 mK, sufficiently deep to trap atoms from the MOT. In figure 2.12 we show an example of the imaging of atoms trapped into the ODT. To optimize the transfer from the MOT into the ODT, we increase the trapping volume of the ODT by appling a fast sinusoidal modulation to both the central frequency and the amplitude of the IPG's AOM (fig. 2.11). The frequency modulation (FM) changes the frequency of oscillation of the AOM piezoelectric (pzt) trasducer. This results in a displacement of the position of the focused beam in the science chamber (after the lens). If the frequency of this modulation is above the trapping frequencies, atoms experience a time-averaged dipole potential with an effective waist larger than the one without modulation (fig. 2.13). Increasing the amplitude of the FM signal leads to a non-Gaussian trap profile. To correct this distortion we apply an amplitude modulation (AM) to the AOM's pzt with frequency twice the FM frequency of 600kHz and a relative phase of $\pi/2$. The AM restores the Gaussian profile with a width of 85 μm on the x-direction and thus the resulting ODT is an elliptic Gaussian-shaped beam with a waist along y-direction instead of 42 μm. The resulting trap depth is $U_0 = k_B$ x $1mK$ while the stimated frequencies, using equation 2.71, are: $\omega_z = 2\pi$ x 38.4 Hz, $\omega_y = 2\pi$ x 9.2 kHz

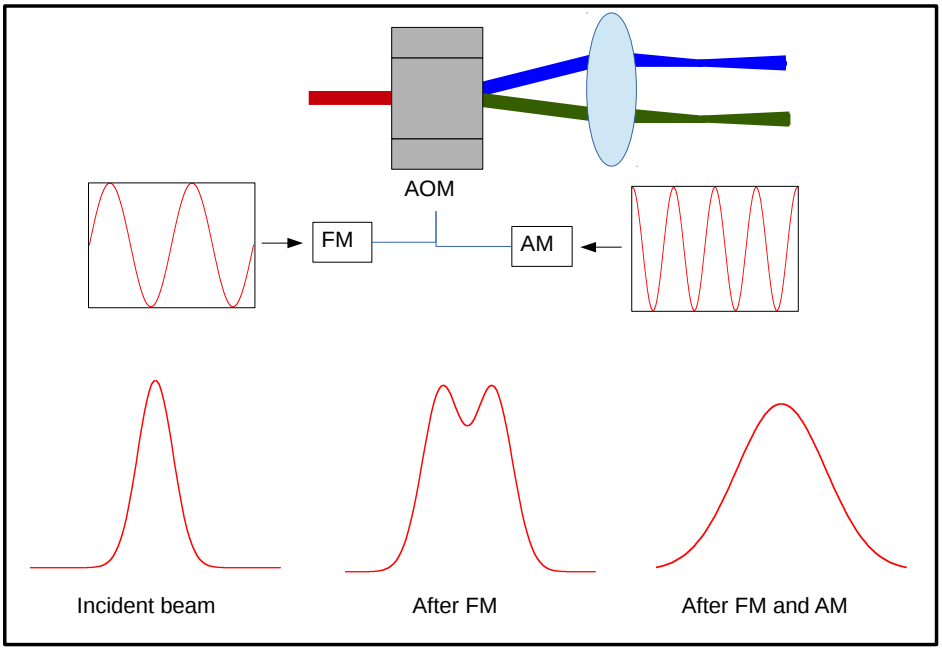

Figure 2.13: Representation of the Frequency Modulation (FM) and of the Amplitude Modulation (FM) signal sent to the IPG's AOM and their effect on the beam. The FM changes spatially the position of the IPG in the focus of the trap, (after the lens) but it distorts the Gaussian beam shape. The AM corrects for the FM's distortion and helps achieving the Gaussian profile but with an enlarged waist.

(the radial horizontal frequency) and $\omega_x = 2\pi$ x 4.5 kHz (the radial vertical frequency). We note that the ODT aspect ratio is $\omega_{radial}/\omega_x > 100$, i.e. much larger than one, which means that it strongly confine the atoms radially but not axially. The axial confinement is instead achieved by the Feshbach and curvature magnetic field as we mentioned above. In fact our Feshbach coils produce also a magnetic field curvature which gives raise to an axial magnetic confining potential along x-y for the high field seeker states, that at low value of the ODT intensity generates the necessary axial confinement. For example, at 834 G this confinement corresponds to a frequency $\omega_c = 2\pi \times 8$Hz. This residual curvature is due to the fact that the two Feshbach coils are opportunely placed at a distance smaller than the Helmoltz configuration providing so a trapping potential for the high-field seeker two-state mixture

$$U_c(x,y) = \frac{1}{2}m\omega_c^2(x-x_0)^2 + \frac{1}{2}m\omega_c^2(y-y_0)^2 \tag{2.7}$$

According to the Maxwell's equation, along the z-direction must be an anti-confining magnetic curvature (anticurvature) whose corresponding potential is

$$U_{ac}(z) = \frac{1}{2} m\omega_{ac}^2 (z - z_0)^2 \tag{2.8}$$

We note that while in the radial plane this curvature traps the atoms in the $m_F = \pm 1/2$ states, in the axial direction is antitrapping the atoms with a frequency $\sqrt{2}$ larger than the radial one. This must be kept in mind, since along this direction we have to consider also the effect of gravity:

$$U_{grav} = mgz \tag{2.9}$$

So, the resulting confining potential is given by the sum of all these contributions

$$U(x, y, z) = U_{opt}(x, y, z) - U_{grav}(z) - U_{ac}(z) + U_c(x, y) \tag{2.10}$$

Chapter 3

Efficient production of ^{6}Li quantum degenerate gases using D_1 gray molasses

In the previous chapter I have described the experimental set-up to trap and cool ^6Li gases obtaining a phase-space density ρ on order of 10^{-5} and a temperature of 500 μK. To increase the initial phase space density for evaporative cooling and to optimize the loading in the ODT, we have developed for the first time on ^6Li a new cooling scheme [24], [25], [26] based on a blue-detuned gray molasses respective to $F \rightarrow F' = F$ transition. This cooling technique permits to achieve temperature on order of 40 μK and a phase-space density 60 times larger than the one achieved in the MOT [27]. These represent ideal conditions to start evaporative cooling to achieve the quantum regime. In the following I will illustrate the main theoretical aspects of the blue-detuned gray molasses addressing how this novel cooling scheme allow to achieve quantum degeneracy of large samples in a very efficient way. In particular, with a total experimental cycle time of 12 s, we create either pure molecular Bose-Einstein condensates of up to 5x10^5 molecules or degenerate Fermi gases of about 8x10 ^{5} atoms at $T/T_F < 0.1$.

3.1 The working principle of gray molasses

This cooling mechanism is based on: the existence of dark and bright states when a blue-detuned light respectively to a $F \rightarrow F' = F$ (our case) or a $F \rightarrow F' = F-1$ transition is sent to atoms and on the coupling between these states which gives rise to Sisyphus cooling. The dark state is not coupled to the light field as we will see later, thus its energy does not change. The

energy of the bright state instead is positive for positive detuning and varies spatially depending on the light intensity variations and on the polarization gradient. When the atom is in a dark state, it can be excited to the bright state and this coupling is more likely to occur at the bottom of the bright state potential [24] (fig. 3.1). When the atom is in a bright state, it climbs up the hill of the optical potential before being pumped back to the dark state near the top of the hill. The kinetic energy of the atom is thus reduced by an amount of the order of the height of the optical potential barrier. Such cooling cycle is repeated, decreasing the temperature of the atomic ensemble to the sub-Doppler regime. Such mechanism is called Sysuphus cooling.

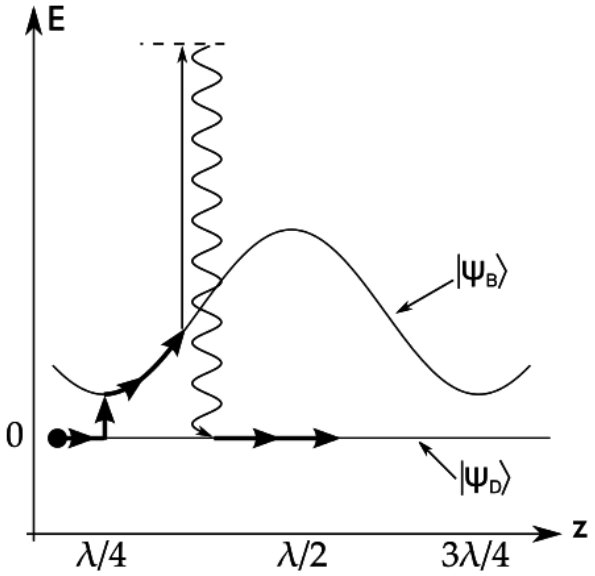

Figure 3.1: The energy of the bright state varying spatially like a sine because of polarization gradients, while that of the dark state remains constant. At the minima of the bright potential, atoms are transferred from the dark $|\psi_D\rangle$ to the bright $|\psi_B\rangle$ state and starts climbing its potential, while loosing kinetic energy. At the top of the bright potential, atoms are pumped back into the dark state, after a significant loss of kinetic energy [24].

3.1.1 Velocity coherent population trapping

To understand the gray molasses cooling mechanism, we consider an atomic system with three levels: two hyperfine ground states $|g_1\rangle$, $|g_2\rangle$ and an excited state $|e\rangle$ forming a Λ-configuration (fig. 3.2). The two transitions $|g_1\rangle \rightarrow |e\rangle$ and $|g_2\rangle \rightarrow |e\rangle$ are driven by two counterpropagating laser beams with

frequency ω_1, ω_2 and detuning δ_1, δ_2 with respect to the corresponding atomic transition. If an atom in the excited state has a momentum p, the ground substates must have a momentum $\vec{p}-\hbar\vec{k_1}$ and $\vec{p}-\hbar\vec{k_2}$ in order to be coupled to the excited state due to the momentum conservation law. For semplicity of notation, we will not specify the atomic kinetic state hereafter. In a

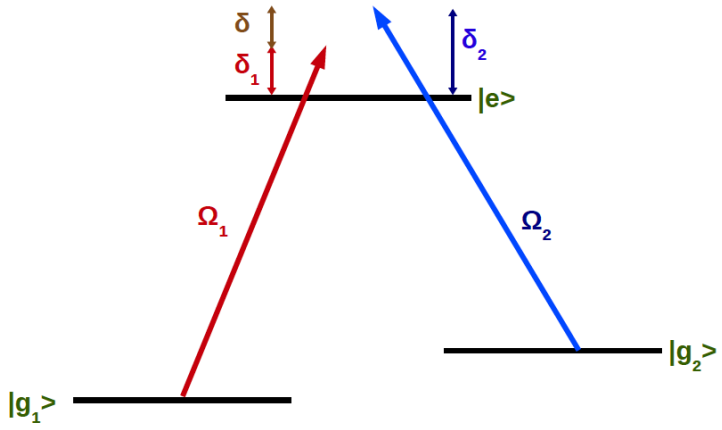

Figure 3.2: Three-level Λ-type system with $|g_1\rangle$ and $|g_2\rangle$ the ground state hyperfine sublevels and $|e\rangle$ the excited state.

semiclassical approach the corresponding hamiltonian H is the sum of the atomic one H_a, which includes the kinetic term $\vec{p}^2/2m$, with the interaction potential

$$\hat{V} = \hbar\Omega_1/2\,|e\rangle\langle g_1| + \hbar\Omega_2/2\,|e\rangle\langle g_2| \tag{3.1}$$

We can introduce a new basis for the ground state given by

$$\begin{aligned} |\psi_{dark}\rangle &= \tfrac{1}{\sqrt{\Omega_1^2+\Omega_2^2}}(\Omega_2\,|g_1\rangle - \Omega_1\,|g_2\rangle) \\ |\psi_{bright}\rangle &= \tfrac{1}{\sqrt{\Omega_1^2+\Omega_2^2}}(\Omega_2\,|g_1\rangle + \Omega_1\,|g_2\rangle) \end{aligned} \tag{3.2}$$

where the first one satisfies $\langle e|\,\hat{V}\,|\psi_D\rangle = 0$, which means that an atom in the $|\psi_{dark}\rangle$ state can not absorb the light and thus can not be excited to $|e\rangle$; for this reason it is called a dark state. The second one instead is coupled to the excited state $\langle e|\,\hat{V}\,|\psi_D\rangle = \hbar\Omega/2$ [28], with $\Omega = \sqrt{\Omega_1^2+\Omega_2^2}$, and for this reason it is called bright state. If an atom is initially prepared in the dark state $|\psi_{dark}\rangle$ and have $p = 0$, it remains there indefinitely if the Raman condition is fulfilled, given by

$$E_2 - E_1 = \hbar(\omega_1 - \omega_2) \tag{3.3}$$

where E_1 and E_2 are the unperturbed atomic hyperfine ground states (without including the light shifts). The Raman condition can be expressed also as having a total detuning $\delta = \delta_1 - \delta_2$ equal to zero. When the atom moves with a momentum different from zero, $|\psi_{dark}\rangle$ and $|\psi_{bright}\rangle$ are not stationary state of H and the kinetic term induces oscillations between these states. An atom can remain in the dark state for a time $\tau_D \propto 1/(vk)^2$ before being pumped to the bright state [28], more probably near the potential minima. Consequently, atoms with lower velocity will stay in the dark state for longer time than the ones having higher velocity which more probably are transferred to the bright state and from there to the excited state by V.
Thus the coherent population trapping in $\psi_{dark}(p = 0)$ becomes velocity selective (VSCPT process) and also the absorption rate of the laser beam, as shown in the figure 3.3. The atom that moves with velocity v climbs up the

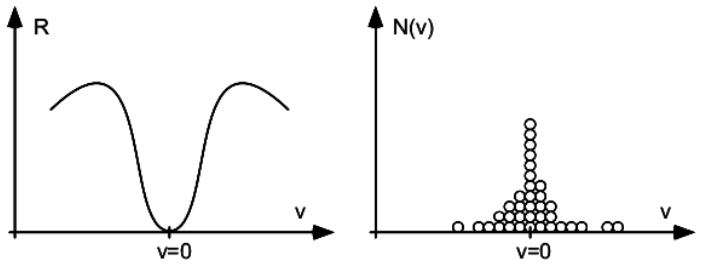

Figure 3.3: The velocity dependence of the absorption rate in the left and the atoms coherent population trapping at v=0 in the right [30].

bright state potential in a time $\tau \propto 1/kv$, reducing so its kinetic energy by an amount of the order of the height of the potential. The optical pumping from the bright to the dark state occurs at the top of the potential hill and is efficient if $\tau \geq \Gamma'^{-1}$, i.e. $kv < \Gamma'$, where Γ' is the optical pumping rate. This expression defines the capture velocity of the molasses $v_c = \Gamma'/k$. For a beam with detuning δ_2 with respect to the cooling transition, we have $\Gamma' \propto I/{\delta_2}^2$ and thus v_c increases with laser intensity. Such cooling cycle is repeated (Sisyphus cooling) decreasing the velocity of these atoms and consequently those with lower velocity are accumulate in the dark state with p in a narrow range around $p = 0$ with a width $\delta p = m\delta v$ (fig. 3.3) proportional to the inverse of the interrogation time.

3.2 The case of ^{6}Li

As the $2^2P_{3/2}$ hyperfine splitting is small compared to the natural width Γ, the gray molasses scheme is based on the D_1 transition of ^{6}Li, the transition from the ground state to the well-resolved $^2P_{1/2}$ manyfold (fig. 3.4). The

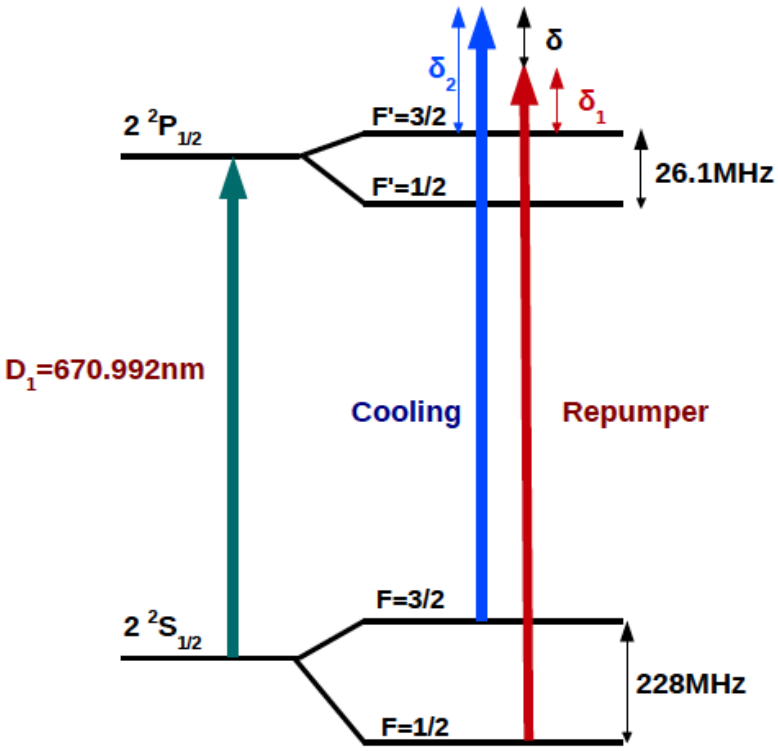

Figure 3.4: The D_1 cooling and repumper transition.

cooling light is blue detuned of δ_2 from $F = 3/2 \rightarrow F' = F = 3/2$ transition while the repumping light is blue-detuned δ_1 from $F = 1/2 \rightarrow F' = 3/2$ transition. The relative detuning is identified as δ. The repumper light not only repump the atoms into the cooling transition but also it can have a cooling effect of its own. In fact, one can see that if the cooling and repumper light fulfill the Raman condition $\delta = 0$ they form a Λ structure which was shown in figure 3.2.

3.2.1 Experimental set-up and the characterization of ^{6}Li gray molasses

Experimental set-up

The D_1 light at 670.992nm is produced by a Tapered Amplifier High Power Diode Laser produced by TOPTICA and it is placed on the same table of the D_2 TA-Pro. The D_1 laser is locked using conventional modulation transfer spectroscopy on the crossover of the transition $|2S_{1/2}, F = 3/2\rangle \rightarrow |2P_{1/2}\rangle$. The output of both laser is shifted in frequency by two AOMs and then coupled on the same optical fiber (fig. 3.5). These two AOMs are used as fast switches in order to turn on or off the D_2 and the D_1 laser lights selectively. This scheme has the advantage that we can use the same optical system for the MOT and the gray molasses without any further adjustment of the alignment [27].

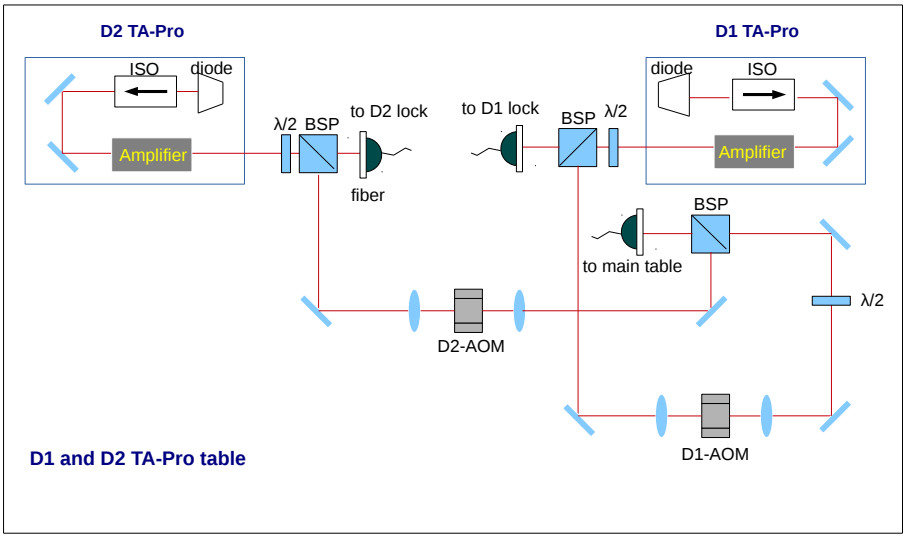

Figure 3.5: The D_1 and D_2 light preparation.

Characterization of ^{6}Li gray molasses

In a first experiment, we measured the cloud temperature after different time duration of the D_1 gray molasses (fig. 3.6). The temperature wass measured by TOF vertical absorption imaging and the error bars are found by repeating

five times the same measurement. The repumper and cooling light detuning were set on the Raman resonance $\delta = 0$, with each detuning $\delta_{cool/rep} = 5.4\Gamma$, while their intensity ratio was $I_{rep}/I_{cool} = 0.2$ with $I_{cool} = 2.7I_s$ and I_s the saturation intensity of the D_2 transition. We note that from 2 ms and

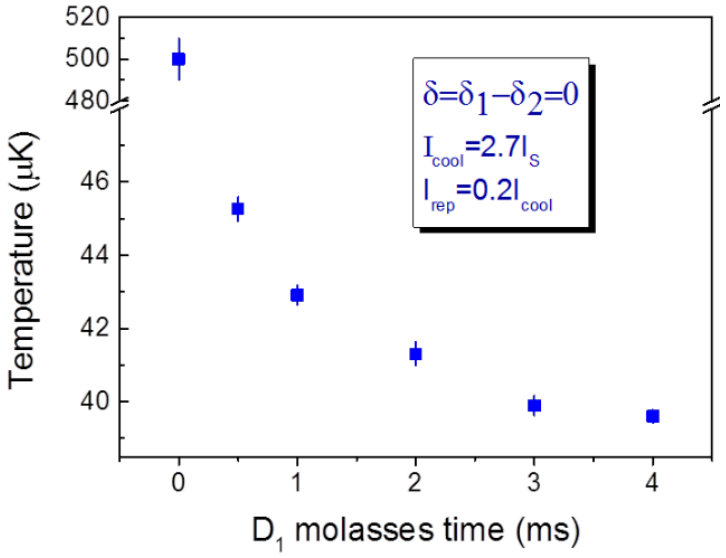

Figure 3.6: The temperature profile as a function of the time duration of the gray molasses. The temperature was measured by TOF absorption imaging and the error bars are found by repeating five times the same measurement, i.e. for the same time duration.

on the equilibrum situation is achieved, so we keep the time fixed at 2 ms in the following measurements. Also, the ratio of the repumper to cooling intensity is kept fixed at this value 0.2 in the following measurements, because was experimentally proved that it corresponds to the lowest temperature. By increasing the D_1 cooling light intensity, the number of captured atoms increases as is shown in figure 3.7, which is expected as the molasses capture velocity increases with the cooling intensity ($v_c \propto I$). The number of atoms was found by integrating the vertical absorption imaging density profile along the other two spatial-directions. In a second experiment, we investigated how the D_1 molasses efficiency depends on the repumper and cooling absolute detuning taken equal, i.e. on the Raman resonance. In figure 3.8 is shown the profile of the temperature and the cooled fraction, i.e. the ratio between the number of atoms captured by the molasses (N) to the one loaded in MOT (N_0), as a function of the absolute detuning expressed in units of

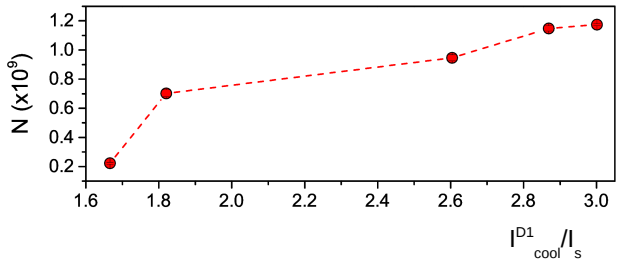

Figure 3.7: The number of the captured atoms in the gray molasses increases with the cooling laser intensity as the molasses capture velocity increases too.

Γ. We observe that for $4\Gamma < \delta_2 < 8\Gamma$ the temperature T and N/N_0 does not change, so we set $\delta_2 = 5.4\Gamma$ value hereafter. For $\delta_2 > 8\Gamma$ the cooled

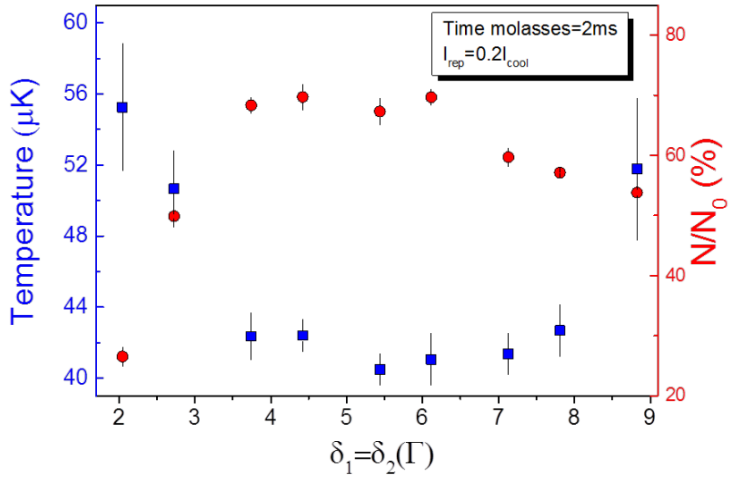

Figure 3.8: Temperature (blue) and the captured fraction $N/N_0 =$ (red) as a function of the absolute detuning δ_2 expressed in units of Γ.

fraction decreases due to the inverse dependence of the capture velocity with detuning ($v_c \propto 1/\delta^2$). By varying the relative detuning δ (keeping fixed the cooling detuning and changing the repumper one), we note that around the Raman resonance $\delta = 0$, the temperature dependence on δ shows the asymmetric Fano-profile with a small width (0.1Γ) (fig. 3.9). This is an evident signature of the emergence of a quantum interference effect. At the Raman resonance, the minimum temperature $T = 40.5(1.0)\ \mu K$ is achieved,

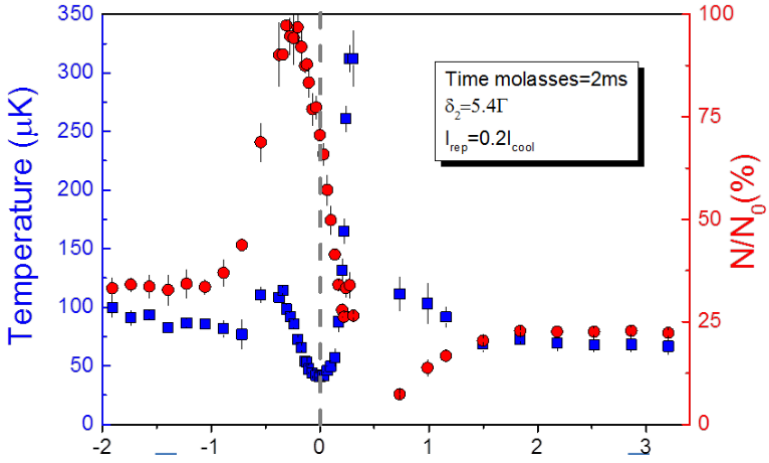

Figure 3.9: Captured atom fraction (red) and the temperature (blue) profile as a function of the relative detuning δ.

due to the Sisyphus effect on the blue-side of $F \rightarrow F' = F$ transition and the formation of the dark coherent state $|\psi_{dark}\rangle$ as I shown in the previous section. To this temperature corresponds a cooled fraction $N/N_0 = 75\%$ and its maximum value is achieved for an off-resonant detuning value $\delta = -0.2\Gamma$. For δ slightly positive instead we observe heating and atom losses. This can be explained by the fact that away from the resonance the atom number and the temperature assume stationary values determined by only the Sisyphus cooling mechanism [26]. Finally, we note that the $|F = 3/2\rangle$ and $|F = 1/2\rangle$ population ratio depends on the repumper to the cooling light intensity like

$$\left(\frac{\Omega_1}{\Omega_2}\right)^2 = \frac{I_{rep}^{D1}}{I_{cool}^{D1}} \tag{3.4}$$

Consequently, for $I_{rep}^{D1}/I_{cool}^{D1} \simeq 0.2$, we find at the end of the molasses phase almost 85% of the population transferred into the lower hyperfine level $F = 1/2$. In the end of the D_1 gray molasses scheme we measured a phase-space density of $2\text{x}10^{-5}$ at Raman resonance, about 60 times larger that the one obtained with the only D_2 cooling stages and this is a favorable starting condition to load efficiently the atoms into an optical dipole trap.

3.2.2 Interpretation of the experimental results

Lets suppose that the cooling light intensity is much larger than the repumper one and that their frequencies satisfy the Raman condition. In this limit, we can consider the scattering of a single photon ω_1 by an atom that interacts

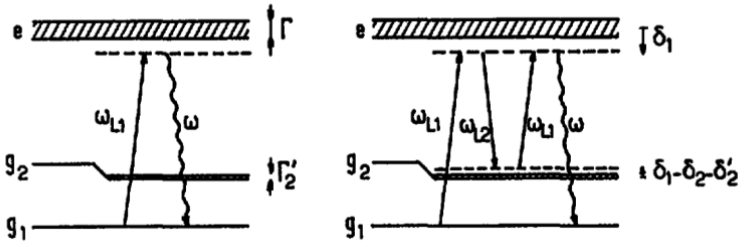

Figure 3.10: Representation of the scattering process in terms of bare states. In the left part (a): the Rayleigh scattering process from $|g_1\rangle$, the absorption of a ω_1 photon followed by the spontaneous emission of a ω photon. In the right part(b): the Stimulated Raman process $|g_1\rangle \rightarrow |g_2\rangle$ through the absorption of a ω_1 photon followed by stimulated emission of a ω_2 photon followed by the Spontaneous Raman process consisting in the absorption of an ω_2 photon bringing the atom in the state $|e\rangle$ and the fluorescence emission of ω photon bringing the atom in the $|g_1\rangle$ [29].

with several ω_2 photons [29]. The new system eigenstates, called dressed states, originating from the interaction of the atom in the state $|g_2\rangle$ with the cooling light are

$$\begin{aligned} |2'\rangle &\propto |g_2\rangle - i\frac{\Omega_2(z)}{\delta_2}|e\rangle \\ |3'\rangle &\propto -i\frac{\Omega_2(z)}{\delta_2}|g_2\rangle + |e\rangle \end{aligned} \tag{3.5}$$

If the radiative broadening of the state $|3'\rangle$ is larger than the one of the state $|2'\rangle$, it appears as a continuum with respect to the narrow $|2'\rangle$ and $|g_1\rangle$ states. The atom after absorbing the ω_1 can be transferred even in the state $|2'\rangle$ as it is contaminated by the excited state $|e\rangle$. Such contamination can be described in terms of virtual absorption and emission of ω_2 photon by the atom in state $|g_2\rangle$. So we expect in this basis of bare state two possible paths (fig. 3.10) for the atom to go from $|g_1\rangle$ to $|e\rangle$ states: the first one is by absorbing the photon ω_1 and going directly from $|g_1\rangle$ to $|e\rangle$ (Rayleigh scattering) and then returning to $|g_1\rangle$ by fluoresence emission of a photon ω. The second one intead is a three-photon process which consists on the absorption of a ω_1 photon followed by stimulated emission of a ω_2 photon which brings the atom in the $|g_2\rangle$ state (Stimulated Raman process) and in the end by the absorption of an ω_2 photon bringing the atom in the state $|e\rangle$ and the fluorescence emission of ω photon (Spontaneous Raman process). The interference of the second path which passes through a discrete state with the first one which is a direct path towards the continuum gives rise to

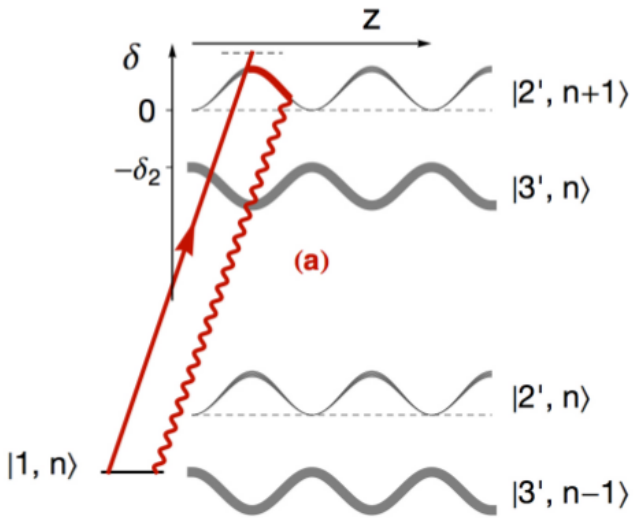

Figure 3.11: If the relative detuning is positive, atoms are pumped from $|1\rangle$ into $|2'\rangle$, more probably at the maxima of the state $|2'\rangle$ light shift. Then they exit this state near the light shift minima by spontaneously decaying into $|1\rangle$ and consequently we expect heating [26].

the Fano profile, characteristic of a resonance between a discrete and continuum state as was also the case of the Feshbach resonance. Let's consider now the dressed state picture [26]. In figure 3.11 is shown the cascade of the doublet dressed state corresponding to different number of ω_2 photons. If the frequency of the repumper light is slightly blue-detuned with respect to the doublet state energy, i.e. the relative detuning is positive (see fig. 3.11), atoms are pumped from $|1\rangle$ into $|2'\rangle$. The pumping process happens more probably at the maxima of the state $|2'\rangle$ light shift as there the detuning of this laser from $|1\rangle \rightarrow |2'\rangle$ transition is minimized. Then the ultracold atoms exit this state near the light shift minima by spontaneously decaying into $|1\rangle$ or into the cascade of dressed states and consequently we expect heating (fig. 3.11). In fact, our experimental results verify such expectation. If the repumper detuning is instead red detuned with respect to the state $|2'\rangle$ energy as shown in figure 3.12, i.e. $\delta < 0$, atoms are pumped at the states $|3'\rangle$ and then they spontaneously decay near the nodes of the state $|2'\rangle$. They climb the potential hill and due to the energy conservation law, reduce their kinetic energy undergoing so the Sisyphus cooling process. Therefore for such detuning we expect cooling and it was experimentally demostrated. At the Raman resonance, the scattering rate of photons is zero due to the coherent population trapping (VSCPT) on the dark state $|\psi_{dark}\rangle$. This implies

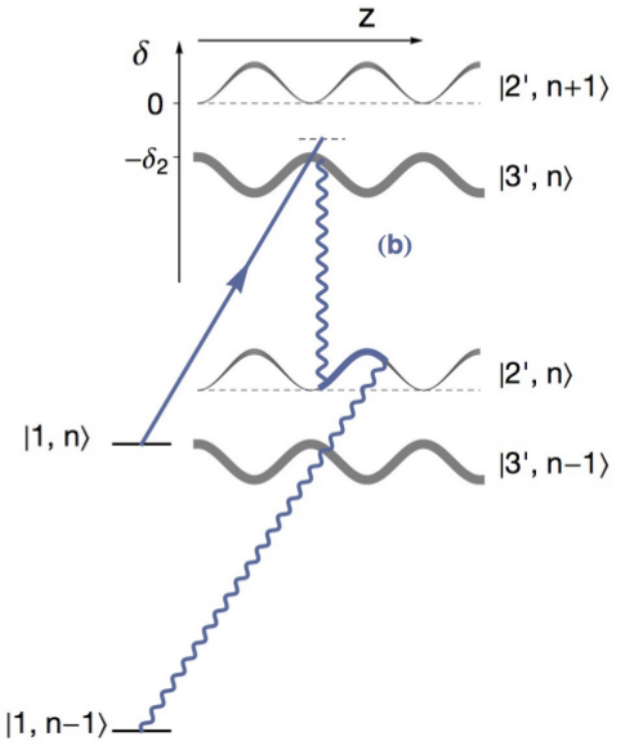

Figure 3.12: If $\delta < 0$, atoms are pumped at the states $|3'\rangle$ and then they spontaneously decay near the nodes of the state $|2'\rangle$. They climb the potential hill and then undergoes the Sisyphus cooling process. Therefore for such detuning we expect cooling [26].

that the Sisyphus cooling produces temperature enough low for the VSCPT mechanism to work. The atoms trapped in $|NC\rangle$ can still be coupling to the bright states giving rise to additional Sisyphus cooling (fig. 3.1).

3.2.3 D1-cooling phase for efficient optical trap loading

To test the feasibility of D_1 cooling in the presence of the strong light field of the optical potential, we first measure the light shifts of the D_1 transitions (cooling and repumper) as a function of the ODT power [27]. We obtain from a fit a slope of $+8.2(7)$ MHz/(MW/cm^2), corresponding to a shift of about 16 MHz ($\sim 3\Gamma$) for our initial trapping intensity. The uncertainty is mostly due to the systematic uncertainty (10%) in the estimation of the trap intensity. This measurement indicates that D_1 blue-detuned molasses can properly work in the ODT, provided that the absolute detuning accounts

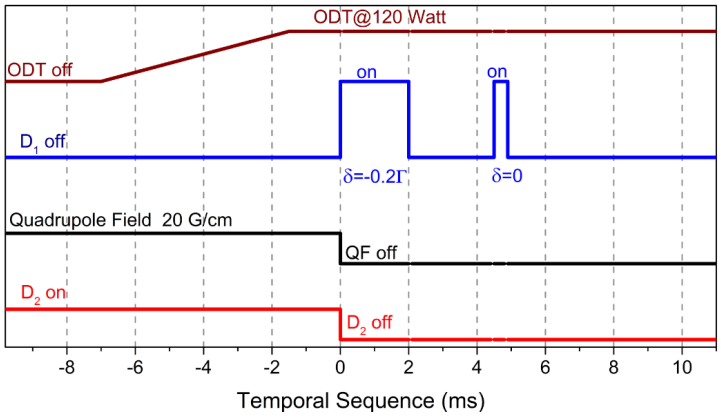

Figure 3.13: Experimental temporal sequence to load the atoms from the MOT to the ODT using D_1 molasses.

for these light shifts, remaining in the range from 4Γ to 8Γ. In order to load into the IPG dipole trap large atomic clouds, we apply a D_1 molasses phase, lasting 2 ms, with a relative detuning $\delta = -0.2\Gamma$ as it corresponds to the maximum captured atoms efficiency (fig. 3.9) even though not to the minimum possible temperature. We found convenient to turn off both the MOT coils and the compensation ones just 100 μs before applying this first D_1 stage. The MOT's beam power are significantly reduced along the direction of propagation of the IPG and allocated along the other axes, creating oblate clouds, in order to increase mode-matching between the MOT cloud and the ODT. The IPG power is instead increased till a value 120 W in 5 ms with a linear ramp, 2 ms before the D_1 phase. The experimental time sequence is shown in figure 3.13. After passing through the corresponding AOM, the IPG's waist along one direction is increased (see section "Time averaged ODT") and so the trapping volume. So, at the end of this D_1 phase, we have a loading atom number of $2\text{x}10^7$ and a temperature of T=135(5) μK. After this phase, we apply a second D1-cooling phase lasting 300 μs and we measure the temperature and the captured atom fraction (fig. 3.14), after 25 ms from the ODT loading, as a function of the relative detuning δ. We note that after the application of the second D_1 phase a temperature of T=80(5) μK is achieved on the Raman resonance $\delta = 0$, which shows that the D_1 cooling is also efficient even in the presence of the high intensity ODT. This minimum temperature is almost a factor of two higher than that measured without ODT and is accompanied by a broadening of the Fano profile around $\delta = 0$. This is due to large atom density inside the optical trap, on order of $10^{14}/\text{cm}^3$, which may limit the efficiency of D_1 cooling [31]. At the Raman

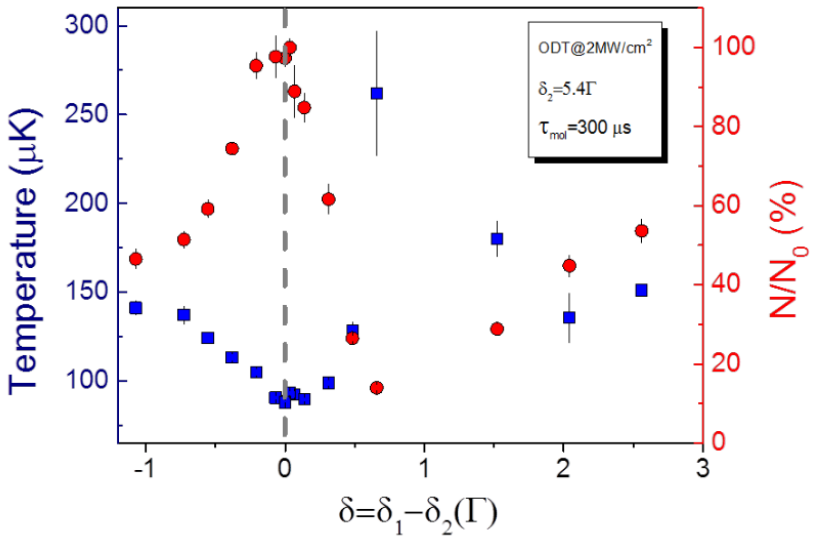

Figure 3.14: The red dots indicate the N/N_0 measured values while the blue squares indicate the T values. The error bars are the standard deviation of five independent measurements.

resonance a maximum captured atom efficiency (100%) is achieved too. This because the temperature of the atoms in the ODT before applying the second D_1 phase is about 135 μK, sufficiently low to allow an effective cooling of all the atoms. The second D1-cooling phase is followed by a hyperfine pumping to the $|F = 1/2\rangle$, lasting 25 μs, achieved by switching off the D1 repumper light before the cooling light. This hyperfine pumping stage also contributs in heating the atomic clouds as it increases the temperature by about 10%.

3.2.4 Production of a molecular BEC and of Fermi gases at BEC-BCS crossover

After loading the atoms into the IPG trap with the two stages D_1 cooling, we ramp up the Feshbach field till a value of 834 G, at the Feshbach resonance, in about 30 ms. The corresponding enhanced scattering length helped us during the evaporation cooling to faster thermalize the gas. We start evaporation by reducing the laser power from 120 W to 30 W with a linear ramp of 500 ms, i.e. from a trap depth of 1 mK to 200 μK. At the same time, we create an incoherent balanced mixture of the two lowest hyperfine states, $|1\rangle$ and $|2\rangle$ state, of ^{6}Li by continuously applying Radio-Frequency (RF) signals resonant with the transition among these two states. After this first evaporation ramp,

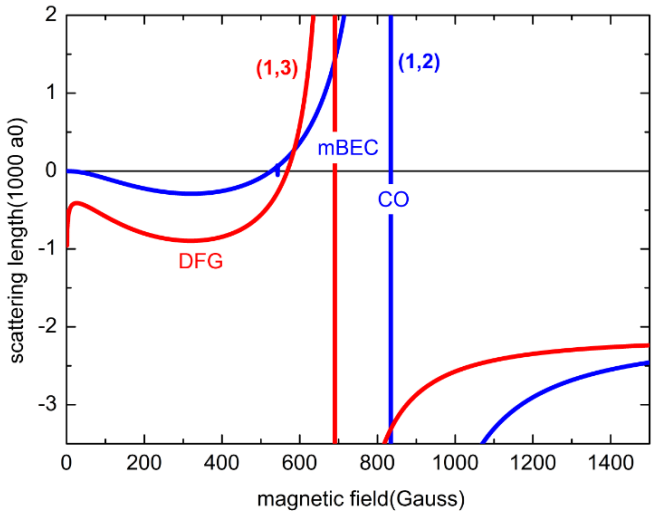

Figure 3.15: Feshbach resonances of ^6Li $|1\rangle - |2\rangle$ and $|1\rangle - |3\rangle$ substates.

we have 10^7 atoms per spin states at $T \simeq 30$ μK.

Molecular BEC

To produce a molecular BEC, we ramp the magnetic field at 780G which corresponds to the BEC-limit of the $|1\rangle$-$|2\rangle$ state Feshbach resonance (see figure 3.15) . Here the atoms are still strongly interacting with a s-wave scattering length $a_{12} = 7000\ a_0$, making so the cloud thermalize faster and thus a more efficient evaporation is achieved. The molecules are formed, by three-body recombination, when the temperature of the cloud becomes comparable with the molecular binding energy ($E_b = \hbar^2/ma^2$) of almost 750 nK at this magnetic field. As the polarizability of the molecules is twice that of the atoms, the trap depth is twice as deep for molecules. During evaporation, this effect suppresses the loss of molecules compared to the loss of atoms. After the first ramp of evaporation, we apply another one but this time to the IPG's AOM, lowering so further the laser power. Accordingly to the time duration of the ramp applied to the AOM, we have different final values of the ODT depth and thus different value of the cloud temperature. By TOF absorption imaging resonant with an atomic transtion, we recover the temperature and the atom number for each of time duration of the evaporative ramp and the results are shown in figure 3.16. We observe a decrease on the total atom number while increasing the ramp time duration, corresponding to lowering the trap depth, which is due to the molecular formation. In this

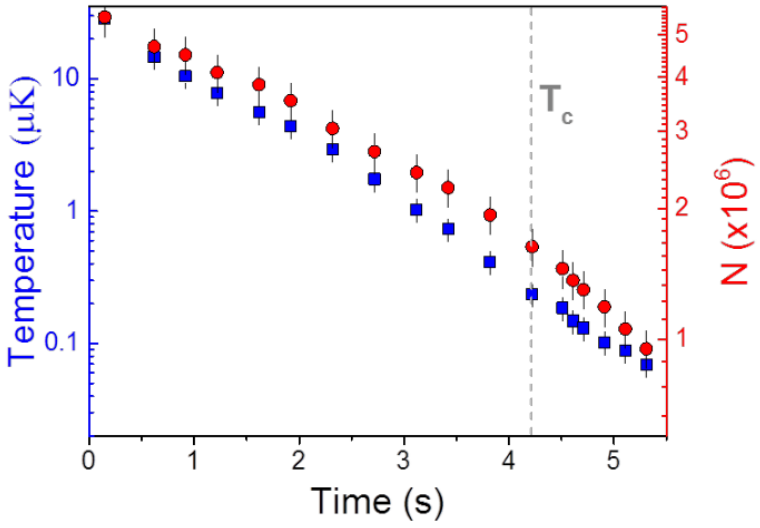

Figure 3.16: The measured temperature and total atom number for different value of the time duration of the evaporative ramp at 800G. The phase transition temperature T_c to the molecular BEC is indicated. The error bars account for both statistical (five independent measurements) and 10% systematic uncertainties.

figure is also indicated the evaporation time corresponding to the onset of the condensation at a critical temperature of T_c =210(20) nK for 10^6 molecules [27]. The error account for both statistical (five independent measurements) and 10% systematic uncertainties. At such magnetic field value, the size of the condensed part is not much smaller than the thermal size, due to the strongly interaction, so the condensate fraction is not well-resolved. For this reason, we reduce the interparticle interaction by adiabatically sweeping the magnetic field to 690 G, where $a_{12} = 1400\ a_0$. In the TOF imaging, the phase transition is observed by the emergence of a bimodal distribution in the two-dimensional density: the central part of the cloud corresponds to a condensed gas and its density is fitted by the integrated inverted parabola (as the Thomas Fermi approximation is valid at 690 G) while density distribution wings are fitted with a Gaussian density distribution. In fact, the fit function is $f(x, y) = y_0 + A \cdot f_{cond} + B \cdot f_{therm}$ where

$$
\begin{aligned}
f_{cond} &= \exp\left(-\frac{(x-x_c)^2}{2\sigma_{th_x}^2}\right)\exp\left(-\frac{(y-y_c)^2}{2\sigma_{th_y}^2}\right) \\
f_{ther} &= \left[\max\left(1-\frac{(x-x_c)^2}{2R_{TF_x}^2}-\frac{(y-y_c)^2}{2R_{TF_y}^2}\right),0\right]^{1.5}
\end{aligned}
\tag{3.6}
$$

with $R_{TF_i}=\sqrt{\frac{2\mu}{m\omega_i^2}}$ the Thomas-Fermi radius. In figure 3.17 is shown an example of a bimodal radial density distribution fitted by this function. From

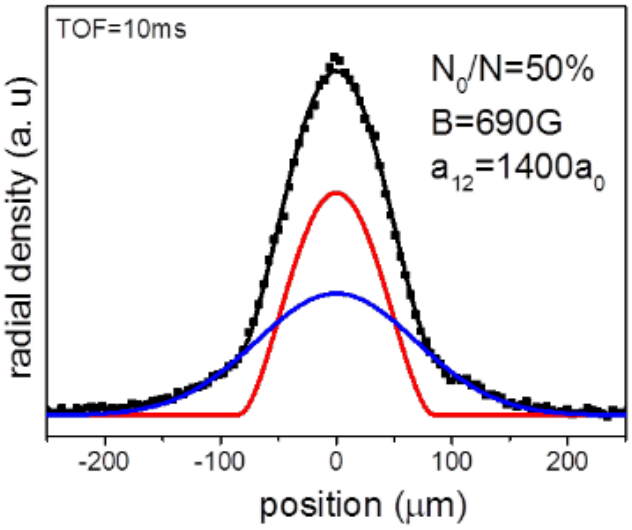

Figure 3.17: The black curve is the measured radial density, whose peak is fitted by a Thomas-Fermi density distribution (the red one), while the thermal wings are fitted by a Gaussian function (the blue curve).

the Gaussian fit of the thermal wings we recover the gas temperature at a TOF of 10 ms. By integrating further the two-dimensional density distribution in the vertical and horizontal radial directions, we found both the number of condensed and thermal molecules and thus the condensed fraction, resulting $N/N_0 = 0.5$ for this example. At the experimental stimated T_c, corresponding to a trap depth of 700 nK, we measure the trap frequencies resulting in $\omega_x = 2\pi \cdot 8.2(1)$Hz, $\omega_y = 2\pi \cdot 111(3)$Hz and $\omega_z = 2\pi \cdot 239(2)$Hz where the first one is given by the magnetic curvature of our Feshbach coils. With these trapping frequencies, we can also give an estimation of the critical temperature using equation 1.10 and we found $T_c = 240$ nK, in agreement with the value of 210 nK found experimentally. Actually, equation 1.10 is valid for a non-interacting Bose-gas but is a good approximation in the case

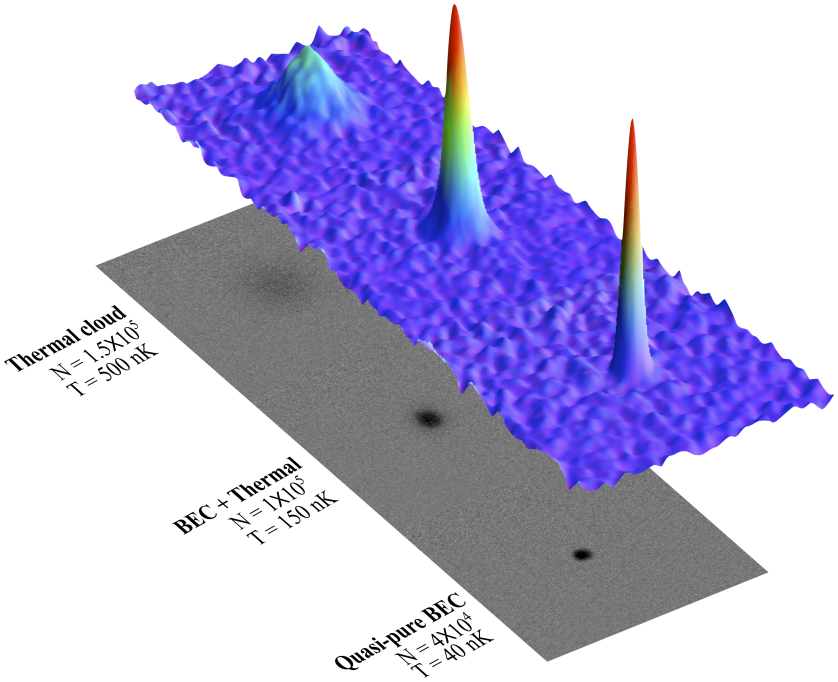

Figure 3.18: Transition from thermal to molecular BEC.

of weakly interacting Bose-gas for which $n_M^{1/3} a_M < 1$, which is verified at the magnetic field value of 690 G. The stimated chemical potential, using equation 1.39, is found to be $\mu = 2.87$ KHz and Thomas Fermi radius are $R_{TF_x} = 268$ μm, $R_{TF_y} = 19.8$ μm and $R_{TF_z} = 9.2$ μm. By reducing the trap depth further, we observe at the end of the evaporation the formation of a mBEC of 5x10^5 molecules without thermal component. Finally we note that when the cloud is released from the trap for a time of flight measurement, it expands as interaction energy is converted into kinetic energy. In anisotropic trap, expansion is fastest in the direction of strongest confinement. In a time of flight image, a cloud released from such a trap thus inverts its aspect ratio during expansion. In figure 3.18 is shown an experimental example of the transition from a thermal gas of molecules to Bose-Einstein condensate.

Production of a Fermi gas at Unitarity

To produce a Fermi gas at the BEC-BCS crossover, we keep on evaporating at a value of 834 G. We end evaporation with other cooling ramps in the ODT intensity, lasting an overall time around 5 s. At crossover we can not resolve the condensed fraction and so is difficult to estimate the critical temperature.

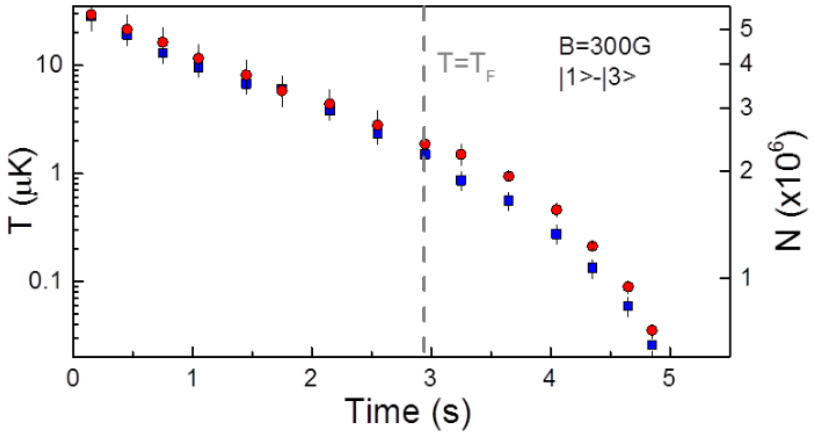

Figure 3.19: Total atom number N (blue) and temperature T (red) of the atoms during evaporation in the ODT at B=300G. The dotted line indicates the evaporation time for which $T/T_F = 1$.

So, we sweep the Feshbach magnetic field 834 G till 690 G, and look at the emergence of a bimodal distribution in TOF measurements. If each fermion pair is transferred into a tightly bound molecule, the momentum information of the original pair is preserved [2]. We observe ultracold clouds of about $2\text{x}10^6$ particles at a temperature corresponding to T_c, when sweeping to the molecular side of the resonance.

3.2.5 Production of degenerate Fermi gas

To efficiently produce weakly-interacting Fermi gases we evaporate the $|a\rangle$ to $|3\rangle$ spin mixture on their Feshbach resonances at 300 G (see figure 3.15, red curve). The first ramp of evaporation is the same as the one applied to produce mBEC. After it, we reduce the magnetic field firstly to the value of 580 G, where the scattering lengths between $|1\rangle - |2\rangle$ and the $|1\rangle - |3\rangle$ mixture are equal (see figure 3.15). This reduces collisional broadening [2] when performing RF-transition among the state $|2\rangle$ to $|3\rangle$. In particular, we trasfer all the atom of the state $|2\rangle$ into the state $|3\rangle$ with a RF π-pulse. Then the magnetic field is brought to a value of 300 G, where the $|1\rangle - |3\rangle$ scattering length has a minimum value of $-900\ a_0$, whose modulus is larger than the $|1\rangle - |2\rangle$ scattering length of $-300\ a_0$, making evaporation in $|1\rangle - |3\rangle$ mixture more efficient as the scattering rate depends on a^2 ($\Gamma_{scatt} \propto \sigma \propto a^2$). In this evaporation procedure, the magnetic field of 300 G is realized with both the Feshbach coils and the curvature one, in order to have a sufficient confinement

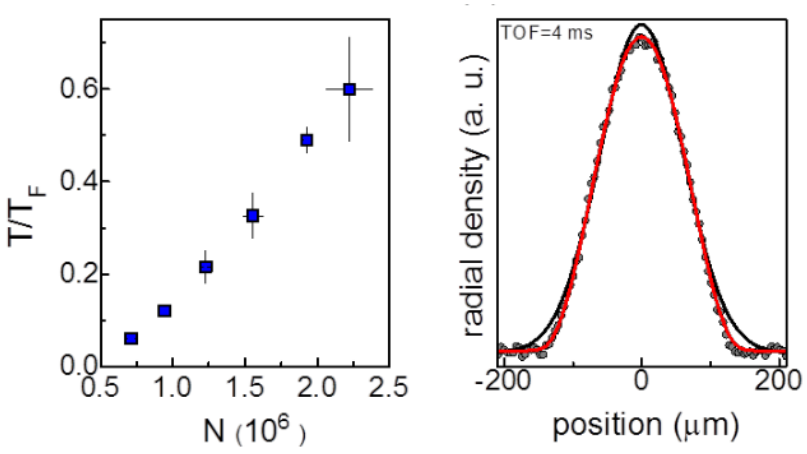

Figure 3.20: Left figure: T/T_F versus N, at the end of the evaporation ramp $T/T_F = 0.06(1)$. Right figure: Comparison between a Gaussian (black line) and the non zero temperature Fermi distribution fit (red line) for $T/T_F = 0.06(1)$. The error bars account for both statistical (five independent measurements) and 10% systematic uncertainties.

along the ODT's axial direction. We end evaporation with a different ramp from the one applied for the production of BEC. In figure 3.19 we show the measured temperature and total atom number as a function of the time duration of the evaporation. We note that the two trajectories are similar with the one for BEC, demonstrating the efficient thermalization between the $|1\rangle$- $|3\rangle$ states. In the degenerate regime ($T/T_F < 1$), we achieve the degenerate parameter T/T_F value by fitting the two-dimensional density with a polylogarithmic function [2]. At $T/T_F > 1$, the temperature is measured after expansion close to the zero-crossing $a_{13} = 0$. We note that after three seconds of forced evaporation, the system enter the degenerate regime ($T \simeq T_F$) with $N_{|1\rangle} = N_{|3\rangle} = 2\text{x}10^6$ atoms. After two other seconds later, we produce a highly degenerate Fermi gas of $N_{|1\rangle} = N_{|3\rangle} = 3.5\text{x}10^5$ atoms at $T/T_F \simeq 0.06(1)$. The corresponding measured trapping frequencies are $\omega_x = 2\pi \cdot 12.4(1)$ Hz, $\omega_y = 2\pi \cdot 111.5(2)$ Hz and $\omega_z = 2\pi \cdot 231(3)$ Hz and thus the T_F determined as:

$$T_F = (6N)^{1/3}\hbar\bar{\omega}/k_B \tag{3.7}$$

is of the order of 800 nK. In figure 3.20 is shown the T/T_F as a function of N and the comparison between a Gaussian distribution and the non zero temperature ($T/T_F = 0.06(1)$) polylogarithmic function, in the limit of weakly interacting fermion, which fit the degenerate Fermi gas density distribution [27].

Chapter 4

Development of a new optical set-up for ^{6}Li imaging

The atom number in the three lowest spin states and the cloud temperature are extracted from the absorption imaging pictures taken either along the horizontal or vertical direction (see section 2.2.1). In order to explore the different interaction regimes, accessible by tuning the Feshbach resonance, a versatile optical scheme is necessary to produce imaging beams whose frequencies correspond to relevant atomic transitions at high and low magnetic field values. In this chapter, I will describe a new optical set-up, which I have designed and partially implemented during my thesis work, for generating the required imaging beams. This scheme, differently from the one actually used in the experiment, is based on an independent laser system, which is frequency-stabilized by a tunable phase-lock loop [32] [33] [34] and allows to image the atoms in a larger magnetic field range.

4.1 Imaging laser system

For generating the imaging lights, I use a commercial external cavity-diode laser at 671 nm (Toptica D.L. Pro) which is amplified, conserving its narrow spectrum, by an home-made tapered amplifier (TA). The laser frequency ν_L is locked at a reference frequency ν_{ref} with an offset frequency ν_{offset}, using a phase lock loop. The reference frequency ν_{ref} is provided by a laser beam derived by the D_2 Toptica TA laser system, which is frequency stabilized using modulation transfer spectroscopy. This reference beam is shifted in frequency by -280 MHz from the cycling cooling transition: $|2S_{1/2}, F = 3/2\rangle \rightarrow |2P_{3/2}, F = 5/2\rangle$. If we indicate with ν_0 the atomic frequency then $\nu_{ref} = \nu_0 - 280$ MHz and $\nu_L = \nu_0 - 280$ MHz$+\nu_{offset}$. In

our system, the offset frequency can range from -150 MHz to -1 GHz. The principle of frequency offset locking [32] [33] [34] consists in overlapping two laser beams, one from a master laser and the other one from a slave laser on a photodiode and then using the resulting beat signal. As the imaging laser system, i.e. the D.L. Pro laser, is arranged on a separate optical table, the light from the master laser beam which is supplied by the D_2 Toptica TA laser, is here transported via a polarization-maintaining optical fiber. In the following subsections, we explain the working principle of the optical phase lock and the related experimental set-up.

4.1.1 Optical phase lock loop

Basic working principle

In figure 4.1, I show a sketch describing the principle of work of an optical phase-lock loop (O.P.L.L.), which consists in a diode laser (D.L. Pro), a phase detector and a low pass filter.

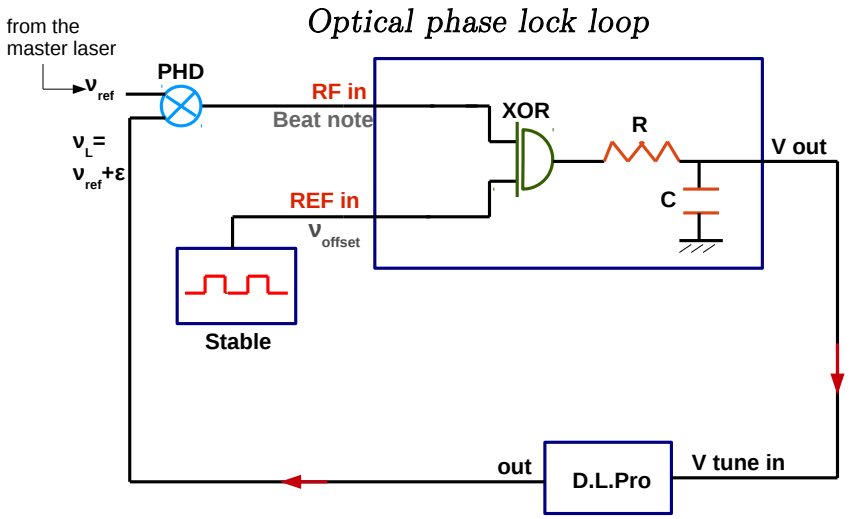

Figure 4.1: Sketch of an optical phase-lock loop.

Firstly, the beat note at the frequency difference between the master (the reference beam) and the slave (whose frequency has to be locked) laser is

XOR

in	out
00	0
01	1
10	1
11	0

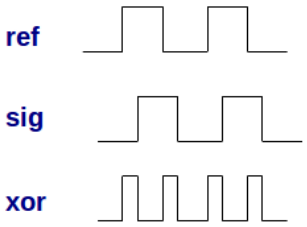

Figure 4.2: Left figure: truth table of XOR gate. Right figure: input and output digital signals at the XOR gate.

detected by a fast photodiode[1] (PHD) whose output drives one side of a two-input exlusive-OR (XOR) gate working as phase-detector (P.D.) [32] [33] [34]. The other side of the P.D. is driven by a programmable frequency generator whose frequency is set at the desidered offset value. By comparing the two inputs, the P.D. produces an output signal (error ϵ signal) proportional to their instantaneous phase difference ($\Delta\phi(t)$).If the two input signals are digital ones (or are converted in digital signals) the XOR output is high when one of the signal is high and is low when both of them are high or both of them are low (see figure 4.2). So, the P.D. produces an output signal whenever there is a phase misalignment between its inputs (indicated with a square wave in figure 4.2).

A time-averaged of this logic signal is performed thanks to the low-pass filter placed after the P.D. (fig. 4.1). During a period, when the XOR output signal is "on" (high), the capacitor is charged until the signal goes "off" where then it begins to discharge at a final value depending on the "off" time duration and on the filter time constant. Over different periods, the capacitor is charged and discharged less undergoing voltage ripples, which after some periods are strongly reduced and the signal is stabilized at its time-averaged value (V_{out}). For larger XOR output duty cycle (the time percentage of a period in which the signal is high), i.e. for larger $\Delta\phi$, V_{out} value is higher reaching its maximum value for $\Delta\phi = \pi$. When its duty cycle is instead 50%, i.e. the corresponding $\Delta\phi = \pi/2$, V_{out} value is half the maximum one. The phase-lock loop is closed by sending the time-averaged

[1]For our photodiode the rise and fall time are 10 ps.

signal to the unlocked D.L. Pro laser driver. The frequency of the D.L. Pro is proportional to V_{out} (traduced in a change in the laser current, which leads to a change in a laser frequency), which on the other hand is proportional to $\Delta\phi$ (with a proportional factor $K = 1.6$ V/rad).
So, if $\nu_{offset} > \nu_{beatnote}$, $\Delta\phi$ increases in time and so V_{out}, leading to an increase of ν_L. Thus in this way the difference between the beat note and the offset frequency is reduced (the opposite happens if $\nu_{offset} < \nu_{beatnote}$). Actually, by tuning the laser voltage input (fig. 4.1) the diode laser frequency is changed of 1 MHz for a 1 mV voltage correction. In our case, when the D.L. Pro laser is locked, $\Delta\phi = \pi/2$. The range of the input signal frequency over which the loop remains locked is limited by the P.D. and the diode laser tuning range. The lock is maintained by the P.D. in a range $0 < \Delta\phi < \pi$; outside this range the slope of V_{out} versus $\Delta\phi$ profile is reversed, so the frequency would change in the opposite direction to that required to maintain the locked condition.

The PHD is polarized by a Bias Tee[2] (see figure 4.3) which contains an inductance ($L \simeq 1$ μH) and a capacitance ($C \simeq 100$ pF) (LC circuit) and its bias is derived by a 9V battery. The alternate current produced by the

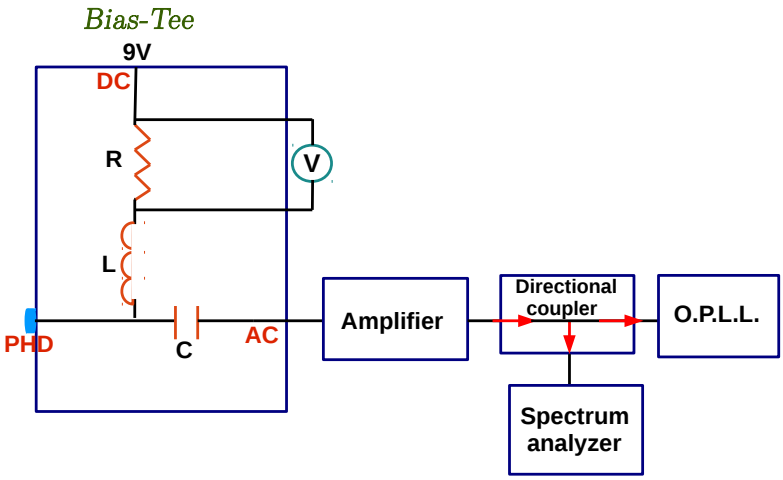

Figure 4.3: Scheme of the Bias-Tee and the signal processing.

PHD is transmitted to the amplifier through the capacitance, whose value at the PHD current frequency is small enough to not significatly reduce the

[2]BIAS-TEE mini-circuits ZX85-12G-S$^+$

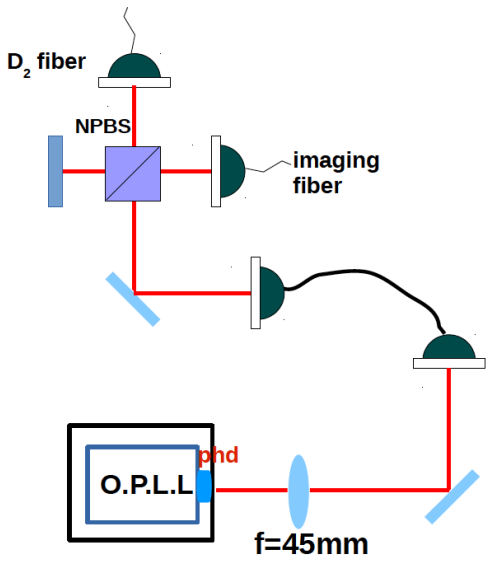

Figure 4.4: Optical scheme for phase locking.

signal. The inductance protects the battery from alternate currents and let the continuous one produced by the battery to polarize the PHD. As the PHD signal is too low for the P.D. to work, it is amplified from -40 dBm at the PHD output to 0 dBm at the P.D. input. After the amplifier, the signal is sent to a 10 dB directional coupler (figure 4.3), which splits the signal in two parts; 10% of the signal is sent to a spectrum analyzer, while the rest 90% is sent to a O.P.L.L. circuitry in order to close the loop.

Experimental set-up

As first, the two laser beams coming from the D.L. Pro laser, amplified by the TA, and from the D_2 Toptica TA are coupled into two optical fibers. The two fibers outputs, which have the same polarization, are overlapped using a non polarized beam splitter (NPBS) (see figure 4.4). The NPBS transmits the 50% of the incident intensity and reflects the rest 50%. Then, the overlapped beams are coupled to the same optical fiber, whose output is sent to the PHD [3]. The PHD signal maximum visibility is achieved when the slave and master laser intensity and polarization are the same. As the PHD photosensitive area (0.2 mm x 0.2 mm) is smaller than the fiber output beam (with waist of about 1 mm), a convergent lens, with focal length of 45 mm, is used to focus the beam on the photosensitive area of the PHD. The

[3]Hamamatsu G4176 series (GaAs)

O.P.L.L. system is mounted on a translation stage which is moved back and forth to align the PHD.Knowing the PHD radiant sensitivity (0.2 A/W) and measuring the beam power (0.3 mW), I stimate the flowing current through the resistor (R=500 Ω) (see figure 4.3) and consequently the voltage drop across it to be 30 mV. So, the goodness of the alignment can be estimated using a voltmeter.

Results

As first step, the laser frequency ν_L of the slave laser is adjusted by tuning both the laser current and the laser piezoelectric voltage control, which changes the length of the external cavity. The frequency is measured using a wavemeter and brought close to the ^{6}Li D_2 transition. After optimizing the PHD signal, the beat note between the locked master laser and the unlooked slave laser is monitored by means of a spectrum analyzer. At this point, we change further the laser current and piezoelectric voltage until the beat note is close to the desired offset frequency ν_{offset}, proved by the function generator. The phase-lock loop is then closed and the laser is locked. We observe that the laser remains locked to the offset frequency until its value is varied over a range of about 800 MHz. The laser output is analyzed using both the spectrum analyzer and a Fabry-Perot cavity with a Free Spectral Range (FSR) of 1.5 GHz. For this purpose, the part of the beam split by the NPBS, which is not used for the lock, passes through the Fabry-Perot interferometer and the laser transmission spectra are acquired by an oscilloscope. In figure 4.5 is shown the transmission spectra for two different values of ν_{offset}:-130 MHz (red line) and -680 MHz (black line). It is worth to note that each spectrum contains two frequencies: one from the master (lower peak) and the other one from the slave laser (higher peak) since the two beams are overlapped. The laser keeps the lock without mode-jumps as ν_{offset} is changed from -130 MHz to -680 MHz. In figure 4.6a and 4.6b we show the beat note, measured with the spectrum analyzer, at the offset frequency of -750 MHz and -1.25 GHz respectively.

The locked beat note signal has a full width half maximum (FWHM) of 611 kHz (fig. 4.7) measured as the distance between the points where the signal drops of 3 dB with respect to its maximum value (as it is normalized). This value depends on the bandwidth of the time-averaged filter used, but as the FWHM is much smaller than the state $|2^2P_{3/2}\rangle$ natural width (6 MHz), it is not necessary to further reduce the FWHM.

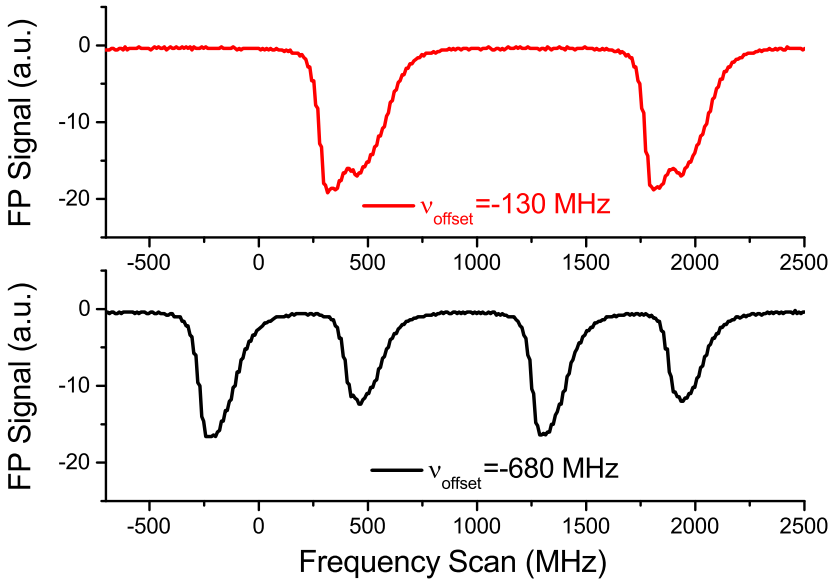

Figure 4.5: Fabry-Perot transmission signal as a function of the frequency for two different values of the offset frequency. The lower transmission peak corresponds to the master laser while the higher one to the slave laser.

4.1.2 Tapered amplifier

The imaging laser's maximum output is limited to 25 mW, however further gain in its power is possible using a tapered amplifier (TA) [35] [36] [37]. This semiconductor device is characterized by a trapezoidal geometry and it is pumped in current; however, contrary to a standard diode laser, the TA chip has an anti-reflection coating ($R_f \approx 1\%$) on both facets in order to prevent internal lasing. Therefore, the TA needs a seed beam, coupled into the front side, for lasing. As the seeding beam propagates through the TA medium is strongly amplified. Here, I describe and experimentally characterize a home-made TA system which uses a GaAs Semiconductor Laser Chip (manufactured by Eagleyard Photonics). This device has been developed and tested in our laboratory, during my thesis work, and it provides a cheap and effective solution to increase the available laser power.

Basic principle of the TA semiconductor chip

The TA chip amplifies the power of an input Gaussian laser beam maintaining its single spatial mode. This is realized by means of a straight index waveg-

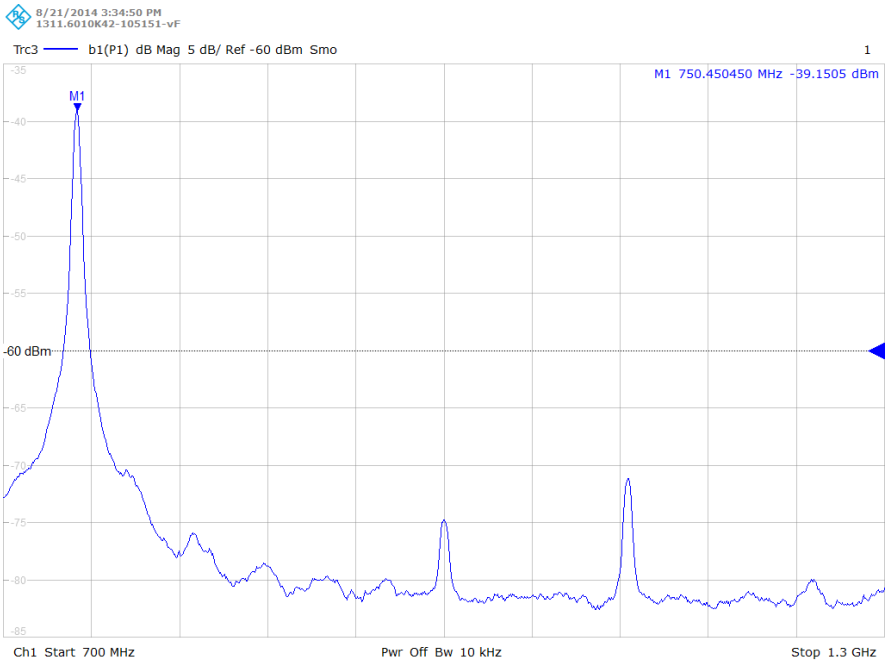

(a) Offset frequency at -750 MHz without mode-hoping.

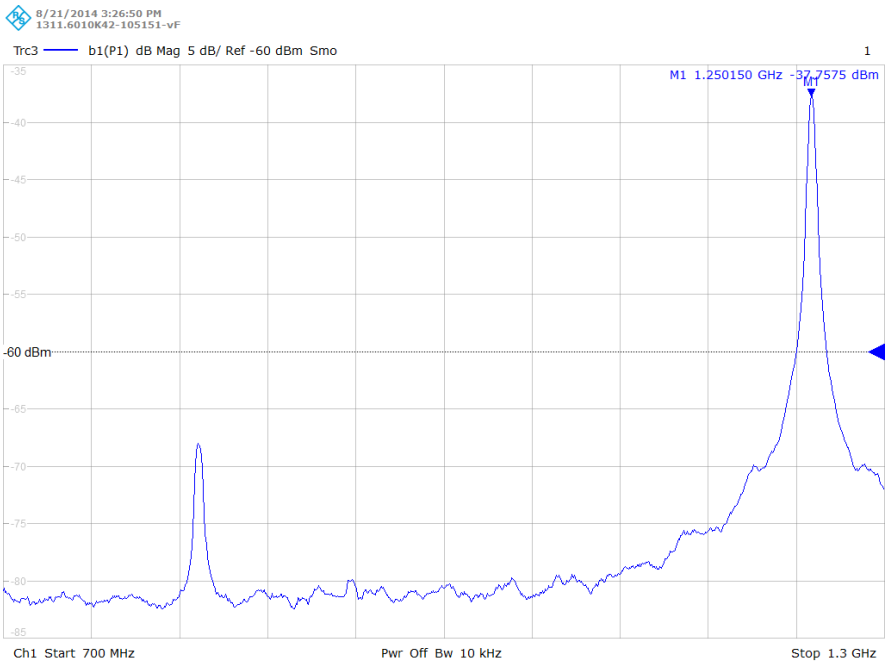

(b) Offset frequency at -1.25 GHz without mode-hoping.

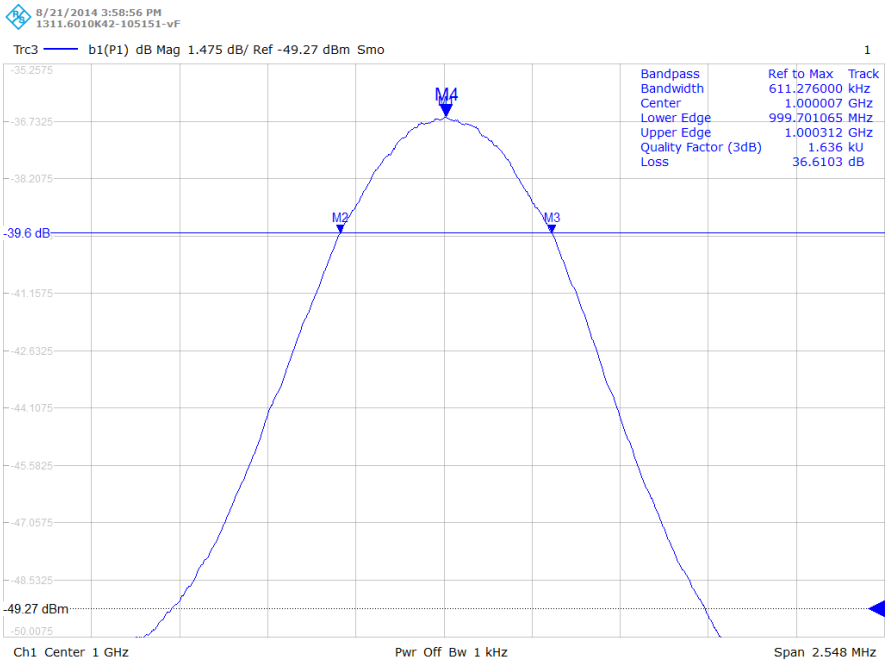

Figure 4.7: The beat note signal.

uide section (L_1=0.5mm) and a gain-guided tapered section (L_2=1.5mm) (see figure 4.8). The seed laser light is coupled, through a narrow aperture (w_1=1.2 μm), into a straight waveguide. The light propagates towards the tapered region where it is diffracted and fills all the gain medium. In a single pass, along the gain medium, the optical power is enhanced and the amplified output beam exits from the cavity through a wider output facet (w_2=205 μm). The small transverse dimensions of the waveguide only permits the fundamental transverse mode to propagate. This has the drawback to limit the output power for a certain energy density. This limit is overcome by the tapered gain region which matches the spatial diffraction of the seed laser light coming out from the straight waveguide (the diffraction angle is about 4^0 for our chip). The active medium is pumped by a spatially homogeneous current density, which gives rise to an uniform gain along the propagation axis, but not laterally as the gain is proportional to the inverse of the optical power density. Thus an incident Gaussian beam experiences a higher gain at its wings and a lower gain at its center; this results in an output beam profile with a "flat hat" distribution. As shown in figure 4.8, cavity-spoiling grooves are etched into the chip, out of the tapered region, to deflect oscillating modes which are not fundamental. Such laser mode wavefronts propagate parallel to the two facets and are known as Fabry-Perot cavity

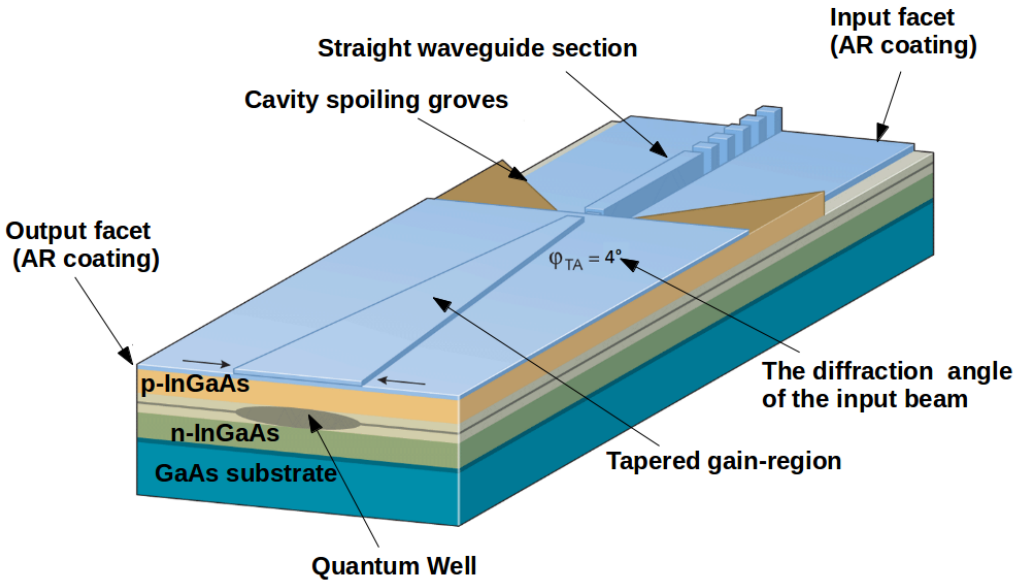

Figure 4.8: Principle drawing of a TA with a straight waveguide and a tapered section.

modes. If these modes are allowed to oscillate they would optically pump the regions of the chip that are not electrically pumped, thus heating up the chip. Due to the diffraction at the tapered angle, the amplitude and phase of the resulted beam will be uniform along the curved wavefronts expanding from the straight aperture. Consequently, the beam emitted from the wide output aperture seems to originate from a point that is approximately L/n_l behind the output facet, with L the length of the gain region and n_l the effective refractive index. Furthermore, according to the Snell's law and for small angles, the output beam horizontal (parallel to the wide side of the facet) diffraction angle is given by the TA chip angle times the lateral modal index. The vertical beam profile instead diffracts with an angle of 45^0 at the output facet.

TA components

A schematic drawing of the TA system is shown in figure 4.9. The chip mount (EYP-TPR-0670-00500-3006-CMT02-0LAB) is screwed to a copper block; we use a thin indium foil pressed between the chip and the copper surface in order to provide a good thermal contact. The copper block is fixed to a copper base plate with a groove wherein a temperature transducer (AD592) is accommodated (fig. 4.9). A ceramic thermoelectric cooler (TEC)

is attached at the bottom of the copper plate and fixed with four Teflon screws on the top of an aluminum heat sink.

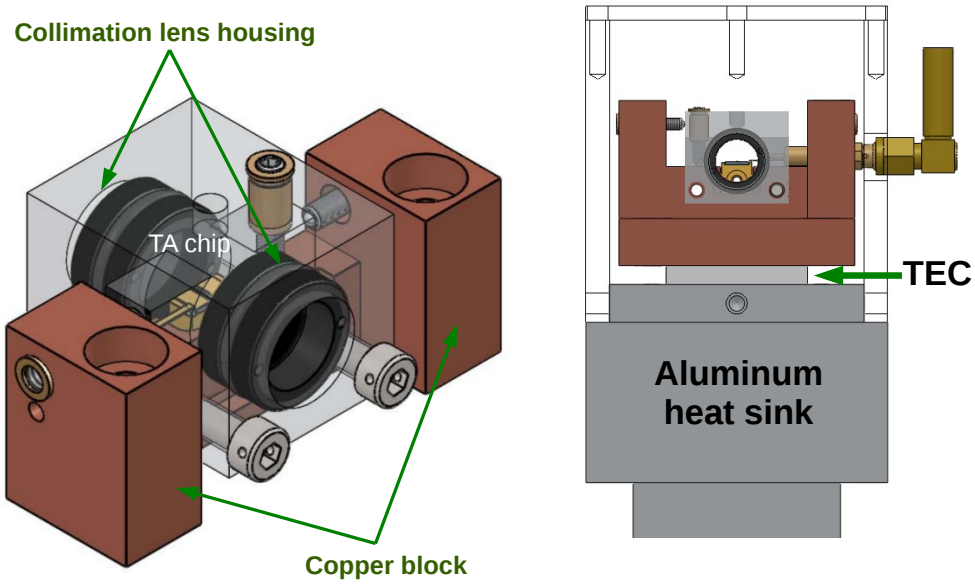

Figure 4.9: Tapered amplifier components.

Two aspherical lenses, with a focal length of 4.5 mm (Thorlabs C230TME-B), are placed in front of both chip facets: one to focus the seed beam, the other one, i.e. the fast-axis collimating lens, to collimate, along the vertical direction, the divergent output beam from the TA. Both lenses are housed inside two holders (Thorlabs S05TM09) which are, in turn, placed into an aluminum block with a fitting thread hole. The lens are aligned with respect to the chip axis by adjusting the position of the aluminum holder by means of three micrometric screws. After the alignment procedure, the aluminum holder is permanently fixed to the copper block with two screws. Holes are cut into the mechanical parts to allow for electrical wires to pass through, in order to supply current to the chip and for temperature regulation. The laser and TEC current are provided by a dual current/temperature controller (Thorlabs ITC4001).

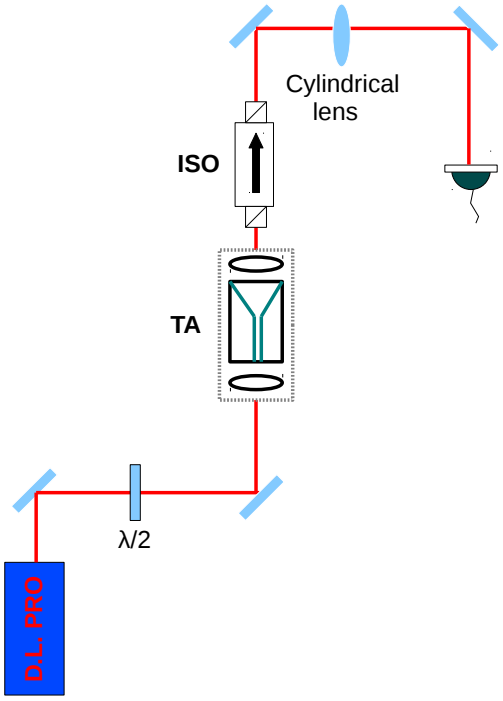

Figure 4.10: Optical set-up for the input and output side of the TA.

4.1.3 TA alignment and characterization

TA alignment

When the TA chip is unseeded, an amplified spontaneous emission (ASE) light is produced by its several quantum wells (see figure 4.8), both from the input and output facet. As a starting point, I set the TA current at 500 mA, not a large value, to avoid damage to the chip because most of the electrical power dissipates as heat when the TA is unseeded (ASE power is low). Then I collimate both sides of the unseeded TA by adjusting the position of the two aspherical lenses. I overlap the D.L. Pro outgoing beam with the TA light emitted from the input facet using a pair of mirrors (see figure 4.10). Once the seed beam is injected in the TA, I observe a suddenly increase of the TA output power, which is measured by means of a power meter. Also, using a spectrum analyzer, an intense peak in a background of ASE multi-mode is noted when the TA is seeded. Since the TA injection efficiency strongly depends on the position of the input collimation lens with respect to the input facet, I slightly re-adjust its position to improve the output power. Once that the alignment of the TA to the seeding beam has been optimized, the

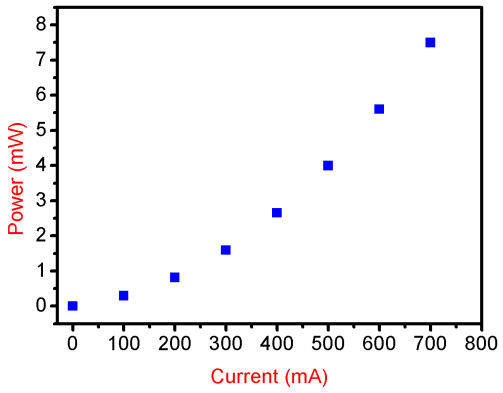

Figure 4.11: ASE power as a function of the TA current.

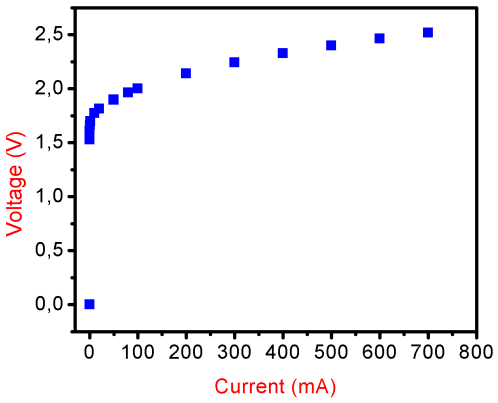

Figure 4.12: The diode voltage as a function of the TA current.

amplified output beam is collimated also in the horizontal direction using an anti-reflection coated cylindrical lens (slow-axis collimating lens) with focal length of 200 mm. In order to protect the chip from any back-reflections, we place an optical isolator (ISO), which provides up to 60 dB of isolation, between the TA output facet and the cylindrical lens.The ISO transmits 74% of the incident light power.

TA characterization

When the TA is unseeded, it simply produces the amplified spontaneous emission light. Since its output and input facets are slightly reflective ($R_f \approx 1\%$), the TA acts as a laser diode. By measuring the output power as a function of the injected current (fig. 4.11), I note a threshold followed by a linear increase of the power versus current, which is a characterizing feature of a laser diode. In figure 4.12 is shown instead the the voltage versus the injected current, which has the same profile as a diode laser. In figure 4.13, I show the spatial density profile of the unseeded TA output beam recorded by a CCD camera. The laser current is set at 200 mA. One can note the expected "flat hat" distribution profile of the light along the x-direction . As the seed beam from the D.L. Pro laser is properly injected into the TA, the laser operation is started and the output power increases. At this point, we characterize the dependence of the TA output power on the power of the seed laser (figure 4.14) and on its polarization (figure 4.15) which is changed using a $\lambda/2$ waveplate. In both cases the TA current is set at 200 mA. One observes that the TA output power linearly increases with the input power and saturates for injection powers up to 17 mW. So, in the following

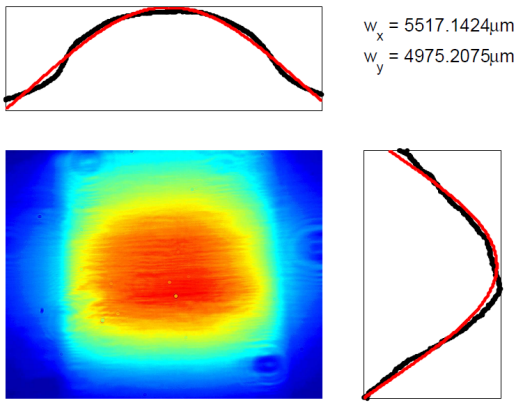

Figure 4.13: Amplified spontaneous emission light of the tapered amlifier at I=200mA. Note the "flat hat" distribution along the x-direction.

measurements the input power was set at a value almost 18 mW in order not to degrade the chip. The output power also depends on the polarization of the seed laser and gets its maximum value for an horizontally polarized seeding beam. I achieve an output power of about 300 mW for a TA current of 600 mA and a seed power of 18 mW. This corresponds to an amplification factor of more than 17. Then, the amplified TA output beam is coupled into an optical fiber and the coupling efficiency is optimized by slightly changing the position of the cylindrical lens. I note that the coupling into the fiber is also affected by the TA current, i.e. the TA mode profile; for a current of about 600 mA we achieve the maximum coupling efficiency which is of the order of 55%.

4.2 Imaging at low and high magnetic field

In order to image the atoms in the three lowest spin states at low and high magnetic field, the D.L. Pro laser frequency ($\nu_L = \nu_0 - 280$ MHz+ν_{offset}) must be resonant with an atomic transition in a large range of magnetic field values. So, ν_{offset} must take into account not only the shift of -280 MHz but also the Zeeman shifts of the ground and excited substates. Also, for the imaging of the $F = 1/2$ state manyfold, hyperfine splittings have to be considered too. In the following, I show the resulting frequency shifts to be compensated, by using also some AOMs, at the particular values of magnetic field of 0 G, 300 G and 850 G. The corresponding Zeeman shifts was calculated via Breit-Rabi formula using Mathematica.

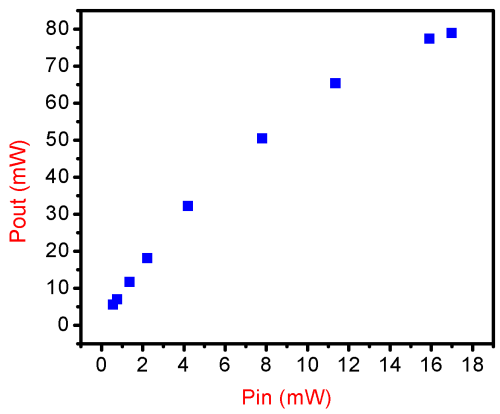

Figure 4.14: The TA output power beam as a function of the seeded laser power.

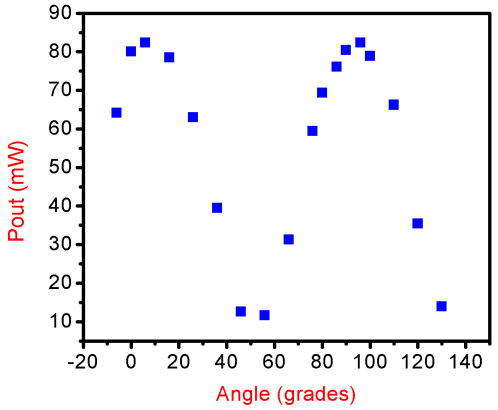

Figure 4.15: The TA output power beam as a function of the seeded polarization.

At zero magnetic field, the $|1\rangle$ and $|2\rangle$ state are degenerate so they can not be resolved; they are contained both at the ground state hyperfine level $|F = 1/2\rangle$. In order to image the atoms that are found in the $|F = 1/2\rangle$ manyfold, I have to compensate for the detuning of -280 MHz (from the $|2S_{1/2}, F = 3/2\rangle \rightarrow |2P_{3/2}, F' = 5/2\rangle$ transition) and for the ground state hyperfine splitting of 228 MHz (i.e. between $|F = 3/2\rangle$ and $|F = 1/2\rangle$ hyperfine substates). Actually, the imaging light, because of dipole selection rules, have to be resonant with $|F = 1/2\rangle \rightarrow |F' = 3/2\rangle$ so the splitting between $|F' = 3/2\rangle$ and $|F' = 5/2\rangle$ have to be considered but it is negligible (almost 2.5 MHz) with respect to the natural linewidth $\Gamma \simeq 6$ MHz. At low magnetic field, in particular at 300 G, the $|1\rangle$ and $|2\rangle$ state are no longer degenerate and it is possible to image the atom population in each spin state (see figure 4.16). For ^{6}Li, such magnetic field value corresponds to the regime where m_I and m_J are good quantum numbers. We choose as imaging light transition: $|m_J = -1/2\rangle \rightarrow |m'_J\rangle = -3/2$. The magnetic field value of 300 G corresponds to the value at which we achieve a weakly-interacting two-state Fermi mixture, composed of $|1\rangle$ and $|3\rangle$ states. To image the atoms in $|3\rangle$ state, I have to compensate only for the Zeeman shifts in addition to the shift of -280 MHz. Another important magnetic field value is 850 G, which is near the Feshbach resonance position between the state $|1\rangle$ and $|2\rangle$. In figure 4.17, I show the offset and AOMs frequencies chosen for imaging of the three lowest spin states at 0 G, 300 G and 850 G. The advantageous of this imaging scheme is that the offset frequency value can be changed in a large range, during which the D.L. Pro laser remains locked, from -100 MHz

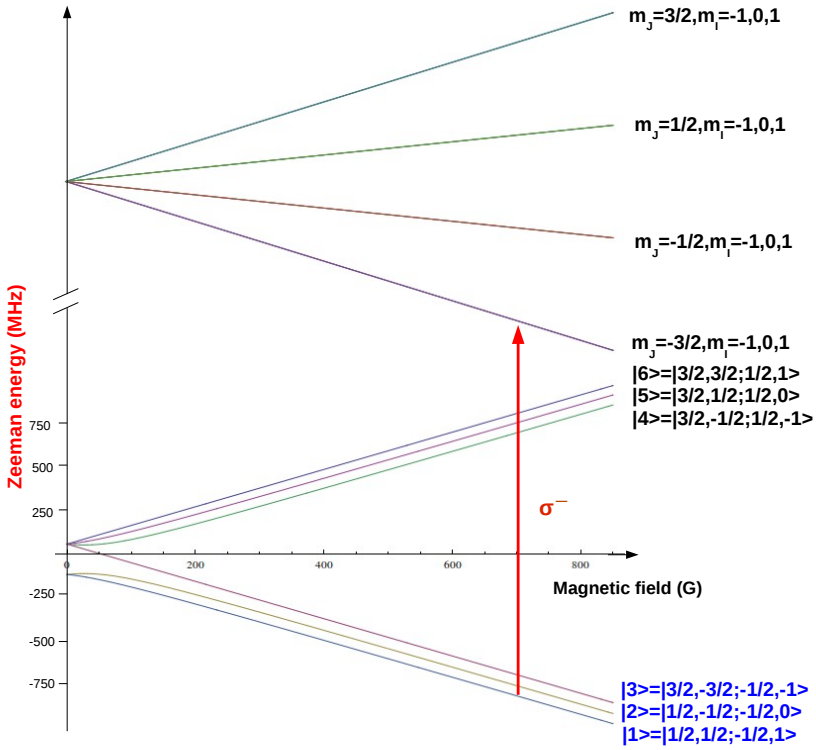

Figure 4.16: The Zeeman splitting of the excited state ($|2^2P_{3/2}\rangle$) and of the ground state ($|2^2S_{1/2}\rangle$) at a range of magnetic field from 0 to 850 G. Actually, the excited state is splitted in twelve Zeeman sublevels which can be resolved at a lower magnetic field range. Also the imaging light transition is indicated.

to more than -800 MHz, permitting so to image the atoms in these states even at intermediate value of magnetic fields.

B(G)	$\|1\rangle$		$\|2\rangle$		$\|3\rangle$	
	AOM (dp)	offset	AOM (dp)	offset	AOM (dp)	offset
0	350MHz	-200MHz				
300	200MHz	-376MHz	200MHz	-450MHz	200MHz	-541MHz
850	-200MHz	-350MHz	-200MHz	-430MHz	-200MHz	-512MHz

Figure 4.17: The offset and AOM frequencies chosen for the value of the magnetic field of 0 G, 300G and 850 G for imaging of each state $|1\rangle$ $|2\rangle$ and $|3\rangle$.

Experimental set-up

In figure 4.18 is shown an optical scheme of the experimental set-up that I mounted in order to prepare the imaging light. The D.L. Pro laser of

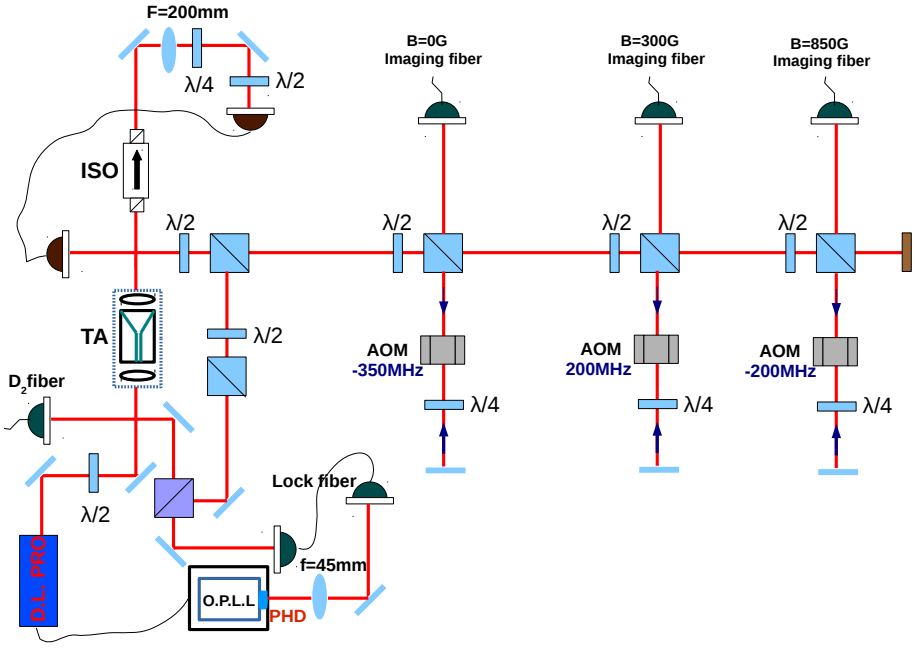

Figure 4.18: A sketch of the experimental set-up that I mounted to preparate the low and high magnetic field imaging light.

the right polarization and power of 19 mW injects the TA, whose output beam power is strongly enhanced. The operation current of TA is set at 600 mA, which corresponded to the maximum coupling efficiency with the polarization-maintaining optical fiber, and its temperature is set at $T = 18°C$. The TA output power at this current is 260 mW. An optical isolator is placed between the output facet and the cylindrical lens to protect the chip from retro-reflection, transmitting 74% of the incident power, i.e. almost 190 mW. After the cylindrical lens, the TA beam divergence is corrected both in the horizontal direction by the cylindrical lens and in the vertical one by the TA output collimation lens. Then the TA beam is coupled to the corresponding optical fiber (indicated with the brown color in figure 4.18), behind which a $\lambda/4$ and a $\lambda/2$ waveplates are placed in order to stabilize the polarization of the light entering the fiber. Its output is then splitted in two parts by a $\lambda/2$ waveplate and a polarizer beam splitter: the transmitted light goes versus the AOMs while the reflected one is overlapped with the D_2 laser, brought in this table by an optical fiber (indicated as "D_2" fiber in figure 4.18), with a NPBS. For practical reasons, the maximum output power of the D_2 fiber is 0.39 mW. After the NPBS, only its 50% is coupled with the "lock" fiber, with an efficency of 74%. In order to have the maximum visibility of the beat note at the PHD, I further reduced the D.L. Pro laser power, by placing a $\lambda/2$ waveplate and BSP along its path and before the NPBS, achieving so equal power of the master and slave laser. I also placed an $\lambda/2$ waveplate after the D_2 fiber in order to achieve the same polarization as the slave laser. The "lock" fiber output (of 0.3 mW) is focused into the PHD by the convergent lens ($f = 45$ mm).

The light that goes versus the AOMs is divided in three "branches" for imaging at 0 G, 300 G and 850 G. Each "branch" consists in a $\lambda/2$ waveplate, a PBS, a $\lambda/4$ waveplate, a mirror and an optical fiber. The part of the light that is reflected from the PBS passes firstly through an AOM. In figure 4.18 is indicated the value of the first order (positive or negative) of the AOM that I used in order to achieve the laser light frequency resonant with the atomic transition. After it, the light passes through a $\lambda/4$ waveplate, which produces a circularly polarized light for our linearly polarized D.L. Pro beam. It passes twice through this waveplate and also through the AOM, after being reflected by a mirror. The result is a laser beam having a polarization perpendicular to its initial one, so now it is transmitted by the corresponding PBS, going versus the "imaging" fiber which brings it to the experiment table.

Conclusions and future perspectives

My thesis work has been focused on the production and characterization of quantum gases composed of ^{6}Li atoms.

- The quantum degenerate regime has been achieved by implementing a new all-optical method based on the combination of D_1 gray molasses cooling (for the first time observed on ^{6}Li atoms), optical trapping and Feshbach resonances. I have experimentally tested that this molasses cooling is particularly effective, reaching temperatures as low as 40 μK for sample composed of almost 10^9 atoms in just few milliseconds. The large phase-space density obtained represents the optimum conditions to load the atoms in a pure optical potential where evaporative cooling to quantum regime has been performed. In the experiment, we have explored the different regimes across the Feshbach resonance of ^{6}Li centered at 832 G. In particular, on the positive side of the resonance we have produced an almost pure molecular BEC of 5×10^5 molecules, while working at the center of the resonance, in the strongly-correlated regime (the so-called BEC-BCS crossover) we have observed similar ultracold gases, eventually superfluid. We have also achieved Fermi degeneracy in the weakly-interacting regime (at 300 G) for about N=7×10^5 atoms at $T/T_F \simeq 0.06$.

- Beside my active participation to the main experimental work, I have also followed a more independent project, designing and setting up a new a and more versatile optical scheme to image the fermionic lithium in a large range of magnetic fields, i.e. of interactions. In fact, as discussed in this thesis, the main and peculiar properties of these ^{6}Li gases rely on the value of the inter-atomic scattering length that in practice we control via an external magnetic field B. This means that it is necessary to compensate the Zeeman shifts of the optical transition in a quite large range of frequency, indeed from 0 (corresponding to null

magnetic field) to almost 1 GHz (B=840 G).
This scheme involves the use of an independent commercial diode laser, of an home-made tapered amplifier and of a electronic offset-lock phase loop (up to 1 GHz) to stabilize this laser to a master, which is referenced to an absolute atomic spectroscopic line. The main advantage of this set-up is the possibility of tuning the value of the frequency with much more freedom, covering the full requested range of values. Furthermore the presence of a tapered amplifier assures the necessary intensity to produce the resonant light to image the atoms in all the three spatial directions.

In the future we want to study the effects of tailored optical potentials imprinted on our ^{6}Li quantum gases. In particular, we are now aiming at investigating the dynamics of lithium superfluids (both in the molecular BEC side and at the crossover of the resonance) through a thin barrier (with a size of about 2 μm) that we are currently implementing on the experiment. The work done in this thesis is the fundamental to proceed in this direction.

Bibliography

[1] S.Giorgini, L.P.Pitaevski, S.Stringari, Rev.Mod.Phys.80.1215 (2008)

[2] W.Ketterle and M.Zwierlein, arXiv:0801.2500v1 (2008), Varenna school.

[3] L.Pricoupenko, Y.Castin, Phys.Rev.A69, 051601(R)(2004)

[4] Ch.Chin et al, Rev.Mod.Phys.82, 1225-1286 (2010)

[5] S.Stringari, Lev Pitaevskii, "Bose-Einstein Condensation", Clarendon Press, Oxford, 2003.

[6] C.J. Pethick and H.Smith, "Bose-Einsten Condensation in Dilute Gases" 2002.

[7] Leggett A.J. "Quantum Liquids: Bose Condensation and Cooper Pairing in Condensed-Matter Systems", Oxford Graduate Texts (2006).

[8] Qijin Chen Jelena Stajic Shina Tan and K. Levin. "BCS-BEC crossover: From high temperature superconductors to ultracold superfluids", Physics Reports, 412(1):1-88 (2005).

[9] Karson Huang, "Statistical mechanics"-Wiley (1987)

[10] E.M.Lifsits, L.D.Landau, "Quantum Mechanics: Non-Relativistic Theory", Butterworth Heinemann, 1977.

[11] M.Inguscio, E.Arimondo and P.Violino, "Experimental determinations of the hyperfine structure in the alkali atoms", Rev. Mod. Phys., 49(1):31 (1977)

[12] J.Clarke, B.Lu J.Walls, R.Ashby and W. Wijngaarden, "Measurement of isotope shifts, fine and hyperfine structure splittings of the lithium lines" (2002).

[13] C.A. Sackett, E.R.I. Abraham, W.I. McAlexander and R.G. Hulet, "Spectroscopic determination of the s-wave scattering length of lithium", Phy.Rev. Lett., 74,(8) (1995).

[14] J.M. Gerton, E.R.I. Abraham, W.I. McAlexander and R.G. Hulet, "Triplet s-wave resonance in ^{6}Li collisions and scattering lengths of ^{6}Li and ^{7}Li, Phy.Rev. A, 55(5) (1997).

[15] G.Zurn, T.Lompe, A.N.Wenz, S.Jochim, P.S.Julienne J.M.Hutson, "Precise characterization of ^{6}Li feshbach resonances using trap-sideband-resolved rf spectroscopy of weakly bound molecules", Phys. Rev. Lett., 110(135301), 2013.

[16] C.C.Tannoudji, D.G. Odelin, "Advances in Atomic Physics: An Overview"

[17] M.Inguscio and L.Fallani, "Atomic Physics: Precise Measurements and Ultracold Matter, Oxford University Press (2013).

[18] H. J. Metcalf and P. van der Straten, "Laser Cooling and Trapping", Springer, (1999).

[19] T.Muller, Phd thesis: "Microscopic Probing and Manipulation of Ultracold Fermions"(2011)

[20] G.Valtolina: "Development of an experimental apparatus for the production and study of ultracold atomic gases of fermionic lithium". Master's thesis, Università degli Studi di Milano, 2012

[21] A.Morales: "High resolution imaging and production of thin barriers for ultracold ^{6}Li Fermi gases". Master's thesis, Università degli studi di Roma, 2013.

[22] M. E. Gehm et al.: "Dynamics of noise-induced heating in atom traps", Phys. Rev.A, volume 58, number 5, 1998

[23] D.M. Stamper-Kurn, W.Ketterle, D.S. Durfee: "Making, probing and understanding bose-einstein condensate. In Bose-Einstein Condensation in Atomic Gases: Proceedings of the International School of Physics (Enrico Fermi), Varenna, 1999.

[24] D. Rio Fernandes et al: "Sub-Doppler laser cooling of fermionic ^{40}K atoms in three-dimensional gray optical molasses", EPL, 100 63001, 2012

[25] G. Salomon et al: "Gray-molasses cooling of ^{39}K to a high phase-space density", EPL, 104 63002, 2013

[26] Andrew T. Grier et al: "Λ-enhanced Sub-Doppler Cooling of Lithium Atoms in D_1 Gray Molasses", Phys. RevA.87.063411, 2013

[27] A. Burchianti et al.: "Efficient all-optical production of large ^{6}Li quantum gases using D_1 gray-molasses cooling", Phys. RevA.90.043408, 2014

[28] A.Aspect et al.: "Laser cooling below the one-photon recoil energy by velocity-selective coherent population trapping: theoritical analysis", Optical Society of America, 1989

[29] B. Lounis and C. Cohen-Tannoudji: "Coherent population trapping and Fano profiles", J. Phys. II France 2 579-592, 1992

[30] A. Aspect, E. Arimondo, R. Kaiser, N. Vansteenkiste, and C. Cohen-Tannoudji, Phys. Rev. Lett. 61, 826, 1988.

[31] D.Boiron et al: "Cold and dense cesium clouds in far-detuned dipole traps", Phys.Rev.A, volume 57, number 6, 1998.

[32] U. Schunemann et al.: "Simple scheme for tunable frequency offset locking of two lasers", Review of Scientific Instruments 70.1 (1999), 242-243

[33] M. Prevedelli et al.:"Phase locking of grating-tuned diode lasers", Appl. Phys.B 60, S241-S248, 1995.

[34] Paul Horowitz, Winfield Hill: "The art of electronics", Cambridge University Press, 1980.

[35] Jayampathi Kangara :"Design and construction of tapered amplifier systems for laser cooling and atom trapping experiments", Master's thesis, Faculty of Miami University.

[36] Jayampathi Kangara et al.:"Design and construction of cost-effective tapered amplifier systems for laser cooling and atom trapping experiments", Am.J.Phys.82, 805, 2014.

[37] Matthias Fuchs :"Development of a high power stabilized diode laser system", Master's thesis, University of Oregon.

[38] E.C. Stoner, Phil. Mag. 15, 1018 (1933).

[39] D Belitz and T. R. Kirkpatrick, arXiv:1204.0873, 2012.

[40] Toshitaka Tatsumi, Physics Letters B, 489(34), 280, 2000.

[41] D. S. Petrov. Phys. Rev. A, 67:010703, Jan 2003.

[42] G.B.Jo, et al., Science, 325,1521, (2009).

[43] A. Barone and G. Paterno, Physics and applications of the Josephson effect, (Wiley) (1982).